

INFORMATION TO USERS

This manuscript has been reproduced from the microfilm master. UMI films the text directly from the original or copy submitted. Thus, some thesis and dissertation copies are in typewriter face, while others may be from any type of computer printer.

The quality of this reproduction is dependent upon the quality of the copy submitted. Broken or indistinct print, colored or poor quality illustrations and photographs, print bleedthrough, substandard margins, and improper alignment can adversely affect reproduction.

In the unlikely event that the author did not send UMI a complete manuscript and there are missing pages, these will be noted. Also, if unauthorized copyright material had to be removed, a note will indicate the deletion.

Oversize materials (e.g., maps, drawings, charts) are reproduced by sectioning the original, beginning at the upper left-hand corner and continuing from left to right in equal sections with small overlaps. Each original is also photographed in one exposure and is included in reduced form at the back of the book.

Photographs included in the original manuscript have been reproduced xerographically in this copy. Higher quality 6" x 9" black and white photographic prints are available for any photographs or illustrations appearing in this copy for an additional charge. Contact UMI directly to order.

U·M·I

University Microfilms International
A Bell & Howell Information Company
300 North Zeeb Road, Ann Arbor, MI 48106-1346 USA
313/761-4700 800/521-0600

Order Number 9128950

Atomic structure and sintering behavior of ultrafine ceramic particles

Bonevich, John Edward, Ph.D.

Northwestern University, 1991

U·M·I
300 N. Zeeb Rd.
Ann Arbor, MI 48106

NORTHWESTERN UNIVERSITY

**Atomic Structure and Sintering Behavior
of Ultrafine Ceramic Particles**

A DISSERTATION

**SUBMITTED TO THE GRADUATE SCHOOL
IN PARTIAL FULFILLMENT OF THE REQUIREMENTS**

for the degree

DOCTOR OF PHILOSOPHY

Field of Materials Science and Engineering

By

John Edward Bonevich

EVANSTON, ILLINOIS

June 1991

ABSTRACT

Atomic Structure and Sintering Behavior of Ultrafine Ceramic Particles

John E. Bonevich

The atomic structure and sintering behavior of ultrafine particles (UFPs) of aluminum oxide were investigated by means of high resolution electron microscopy (HREM) under ultra-high vacuum (UHV) conditions. The UFPs were created by an arc discharge apparatus in an Ar-O₂ atmosphere. They were carried by the flowing Ar-O₂ gas into a custom-built UHV furnace system where they sintered at elevated temperatures and were collected onto a microscope specimen cartridge which was then transferred to the microscope under UHV conditions.

The UFPs were variants of the spinel structure. A 'new' form of the orthorhombic δ -phase was observed to have lattice parameters of $a_{\delta}=1.58$ nm, $b_{\delta}=1.17$ nm, $c_{\delta}=0.79$ nm (space group P2₁2₁2). The monoclinic θ -phase was also possibly observed with the cell parameters of $a_{\theta}=1.09$ nm, $b_{\theta}=0.56$ nm, $c_{\theta}=0.27$ nm, $\beta=103.3^{\circ}$ (space group B2/m). The UFPs exhibited highly faceted surfaces corresponding to the low energy planes of the crystal structure.

The sintering behavior of these UFPs demonstrates three major issues; the surface faceting due to the Wulff construction plays a major role in determining the final sintering geometry with sintering occurring predominantly on the closed-packed {111} facets. Surface diffusion is the predominant mechanism for sintering, as evidenced by the fact that many sintered particles have their initial adhesion structure 'locked-in' during sintering with no reorientation occurring. Furthermore, the necks formed during sintering have well-defined, atomically-sharp contact angles which suggests that the neck growth process is

controlled by the faceted structures and may be modeled by a mechanism similar to crystal growth due to ledges, grain boundaries, and twins. The driving force for sintering can be considered as a chemical potential difference between facet surfaces and the neck region.

Phase transformations may also occur during sintering with the consequence of grain boundary migration and epitaxial crystal growth. Transformations to the δ -phase were observed with both grain boundary migration and grain coalescence competing with the sintering process. No transformations to α -alumina were observed when sintering occurred under 'vacuum' conditions.

Professor Laurence D. Marks (Thesis advisor)

Department of Materials Science and Engineering

Robert R. McCormick School of Engineering and Applied Science

Northwestern University, Evanston, IL 60208

DEDICATION

This work is dedicated to my parents Don and Ann and my brothers Jim and Jeff. The support of family is always the most important.

ACKNOWLEDGEMENTS

I would like to thank my thesis advisor, Dr. Laurence D. Marks, for making this dissertation possible. His continual support and encouragement throughout the course of my doctoral research at Northwestern University is greatly appreciated.

Thanks go to Dr. D. Lynn Johnson who, as the Co-Principal Investigator and my joint thesis advisor, also made this research possible. I would also like to thank the other members of my thesis committee, Drs. Peter C. Stair and Peter W. Voorhees, for their time and considerations.

Special thanks to Mao-Hua Teng who has been my colleague on this project. He contributed both the particle production techniques and constructed the furnace tube for this sintering study. His ceaseless efforts have greatly contributed to the success of this research. I also appreciated his views both of the project and the world at large.

I also appreciate Mr. M. Kubozoe of the Scientific Instruments Division of Hitachi who donated to Dr. Marks the rotary/linear magnetically coupled feedthrough with cerium magnets. This feedthrough was essential to the UHV specimen transfer system.

The members of my laboratory also deserve many thanks. I have always enjoyed both their company and their assistance to me during my stay at Northwestern University. Special accolades to Dr. Jinping Zhang with whom I had many useful discussions on aspects of crystallography and microscopy techniques.

I also greatly appreciate the Department of Energy (Grant #DE-FG02-87ER45309) for their financial support.

TABLE OF CONTENTS

	Page
ABSTRACT	ii
ACKNOWLEDGEMENTS	v
TABLE OF CONTENTS	vi
LIST OF TABLES	ix
LIST OF FIGURES	x
CHAPTER 1 INTRODUCTION	
1.1 Introduction	1
1.2 Macroscopic Sintering	2
1.2.1 Two Sphere Model	4
1.2.2 Analysis of Assumptions	5
1.2.3 Rotating Spheres-on-Plates	8
1.3 Ultrafine Particle Sintering	9
1.4 Role of Contamination	10
CHAPTER 2 IMAGING THEORY AND TECHNIQUES	
2.1 Elemental Electron Microscopes	12
2.2 Electron Optics	16
2.3 Contrast Transfer Theory	20
2.3.1 Conventional Non-linear Theory	23
2.3.2 Improved Non-linear Theory	24
2.3.3 The $\alpha\Delta$ Cross-terms	26
2.4 Multislice Method	29
2.5 Microscopy Techniques	32
2.5.1 High Resolution Imaging	32
2.5.2 Bright-field / Dark-field Imaging	34
2.5.3 Nano-diffraction	35
2.5.4 Energy Spectroscopies	36
2.5.4.1 Energy Loss Spectroscopy	37
2.5.4.2 Auger Spectroscopy	39

CHAPTER 3 EXPERIMENTAL METHODS AND APPARATUS		
3.1	The Arc Discharge Method	41
3.2	Experimental Equipment	44
3.2.1	The UHV Furnace System	44
3.2.2	UHV Furnace Conductance Analysis	54
3.2.3	The Furnace Vacuum System	57
3.2.4	Particle Production Procedure	58
3.3	UHV-HREM	59
3.3.1	The History of UHV Microscopy	59
3.3.2	The UHV-H9000 HREM	64
3.3.2.1	The HREM Vacuum System	65
3.3.2.2	Surface Science Instrumentation	67
3.4	UHV Specimen Exchange	72
CHAPTER 4 EXPERIMENTAL RESULTS		
4.1	Initial (unsintered) Particles	73
4.1.1	Structure	73
4.1.1.1	Delta Alumina	75
4.1.1.2	Theta Alumina	77
4.1.2	Present Results	78
4.1.2.1	Delta Alumina	82
4.1.2.2	Nano-diffraction Results	84
4.1.3	Surface Faceting	86
4.2	Sintered Ultrafine Particles	92
4.2.1	Structure	92
4.2.2	Sintering Process	98
4.2.2.1	Sintering at Low Temperatures	98
4.2.2.2	Sintering at High Temperatures	103
4.2.2.3	Bright-field / Dark-field Analysis	103
4.2.2.4	Phase Transformations	107
4.2.3	Role of Faceting	110
4.2.4	Electron Spectroscopies	111
4.3	Discussion of Results	115

CHAPTER 5	CONCLUSIONS	
5.1	Research Summary	121
5.2	Future Directions	122
REFERENCES		124
APPENDIX 1	Electron Beam - Solid Interactions	134
APPENDIX 2	Fiddelly Bits (Work on the UHV-HREM)	149
APPENDIX 3	What Not To Do (Murphy Was Right)	151
APPENDIX 4	Contrast Transfer Source Code	153
APPENDIX 5	UHV Microscope and Furnace Designs	164
APPENDIX 6	UHV Design Philosophy	172
VITA		175

List of Tables

	Page	
1.1	Mass transport mechanisms during initial-stage sintering.	3
3.1	Arc discharge characteristics showing the relationship of pressure with the mean particle size.	42
3.2	Compilation of the various UHV electron microscopes with related user groups and the surface preparation facilities.	61
4.1	Reported δ-alumina phases from X-ray and TEM data.	76
4.2	Reported θ-alumina phases from X-ray and TEM data.	77
4.3	Optical diffractograms analysis of ultrafine particles.	93
4.4	Ultrafine particles sintering by faceting structure.	111

List of Figures

1.1	Mass transport mechanisms during sintering and the model of Johnson for competing mechanisms during initial stage sintering.	4
1.2	The sintering of two faceted ultrafine particles along {111} surfaces.	4
2.1	The effect of spherical aberration on the Gaussian image.	14
2.2	The effect of chromatic aberration.	16
2.3	Production of the 'out-of-focus' image.	18
2.4	Contrast transfer function for linear imaging (a) and (b) and non-linear imaging with g_{100} (0.25 \AA^{-1}) in (c) and (d).	27
2.5	The orientation of the specimen for high resolution imaging.	33
2.6	Electron-loss near-edge structure of Si, Al, and Mg atoms in different local crystallographic environments.	38
3.1	Schematic representation of the arcing process.	43
3.2	The particle size distribution as a function of arcing pressure.	43
3.3	Schematic of the entire UHV furnace system. The large furnace tube vacuum chamber supports the whole structure and rests upon an angle iron frame (not shown).	45
3.4	The UHV furnace system showing the transfer rod and collection chambers (a) specimen transfer chamber with the cartridge exposed (b).	46
3.4	The UHV furnace tube and vacuum chamber (c).	47
3.5	The measured temperature profile of the furnace tube (courtesy MHT).	49
3.6	The extender tube transports the ultrafine particles through the bellows to the specimen cartridge.	49
3.7	The arcing apparatus is designed to occupy only one 8 inch flange.	53
3.8	Perspective view of the UHV furnace system.	55
3.9	Schematic representation of the UHV-H9000 HREM showing the specimen transfer chamber and the computer-controlled digital acquisition system.	62
3.9	UHV-H9000 HREM in actual use (b). Here, the microscope is seen as a functioning system with the STC attached.	63

3.10	The side view (a) of the specimen transfer chamber showing, among others, the ion milling, controlled atmosphere, and specimen exchange facilities.	69
3.10	The top view (b) of the specimen transfer chamber showing the multiport flange, the LEED/Auger optics, the specimen exchange port, and the recessed viewport.	70
3.11	The STC instrumentation with line-of-sight at the specimen.	71
4.1	γ -alumina spinel particle aligned near to the [011] zone with ODM.	79
4.2	Calculated images of the alumina spinel. Thickness of 10 nm as a function of lens defocus; starting at -20 nm in steps of -5 nm. (a) no tilt and (b) 2 mrad of tilt..	79
4.3	Schematic representation of the spinel structure viewed down [011].	81
4.4	γ -alumina spinel particle oriented along $[\bar{1}12]$ zone with ODM.	81
4.5	Schematic representation of the diffraction pattern from δ -alumina particle of the [011] zone. The actual zero order Laue zone is shown at the left.	83
4.6	Large particle of δ -alumina oriented along the [012] zone. The DP in (b) has obviously been montaged to bring out all intensities in the pattern.	83
4.7	Typical diffraction patterns from the HF2000 showing in (a) the $[111]_{\gamma}$, in (b) the $[100]_{\gamma}$, in (c) the $[112]_{\gamma}$, and (d) a particle with 5 minutes beam damage.	85
4.8	Wulff construction of the [011] zone. Each facet's perpendicular bisector intersects with the Wulff center of the particle. The {220} facets are treated as locally flat.	88
4.9	Plot of the total facet length scaled by particle diameter vs. diameter. As the size decreases, the {111} facets grow at the expense of the {200} and {220}.	88
4.10	Schematic representation of a twinned particle showing the mathematical cut along the twin boundary. Values of r_i are measured from each particles' respective Wulff centers, i.e. $r_1 \neq r_3$.	90
4.11	A particle of δ -alumina along [120] is sintered to another particle on a irregular facet surface which corresponds to the reentrant surface of a twin, see §4.2.2.	94

4.12	A sintered particle which is analyzed by the ODM method to be $[123]_{\gamma}$ orientation. The dark-line facets are identified as $\{111\}$ surfaces.	94
4.13	A particle of γ -alumina along $[136]$ according to the ODM analysis. The particle can also be identified as $[010]$ of the θ -phase which is monoclinic.	95
4.14	The focal series simulation of the $[010]_{\theta}$ zone. The thickness correspond to 4 nm (a) and 10 nm (b) with lens defocus starting at -10 nm in steps of -10 nm.	95
4.15	Particle which can be identified as either the $[123]_{\gamma}$ or $[361]_{\gamma}$ zones from the ODM analysis. However, there was no image match suggesting instead another phase.	96
4.16	Schematic representation of an ordering process leading to a change in symmetry and lattice parameters, but not a macroscopic shape change. In (a) the initial γ -phase transforms to δ -alumina (b). The triangles are typical tetrahedral sites, $[100]$ zone.	97
4.17	Two 'spherical' particles have sintered with a small neck, no densification.	97
4.18	Chains of sintered particles. Here the particles have adhered with no apparent reorientation as arrowed in (a). In (b) note the distorted Wulff shape, arrowed.	99
4.19	Two particles which have sintered with a 5° misorientation of their $\{311\}$ planes. These spherical particles were able to 'roll around' to achieve this orientation.	101
4.20	Many particle system where all particles have sintered on their $\{111\}$ facets.	101
4.21	Two particles which have sintered to a third particle. The grain boundary region is distinct from the two particles.	102
4.22	Many particles which have sintered and are constrained from densifying.	102
4.23	Many particle system where all particles have sintered at 1200°C . The arrowed particle has experienced particle/grain growth and has a quite distinct grain boundary region. A scanned representation of the particles is shown in (b).	104
4.24	Bright field/dark field montage of sintered particles. The particles show a high degree of internal faulting and twinning as a result of particle adhesion.	105

4.25	Bright field/dark field montage of sintered particles. Again the particles have internally faulted in response to the adhesion stress. The arrowed particles also show indications of inhomogeneous strains as a consequence of sintering together.	106
4.26	Two sintered particles that have undergone a transformation to the δ -phase. The smaller particle has grown epitaxially with the larger particle, oriented along $[102]_{\delta}$. The grain boundary is now inside the smaller particle.	108
4.27	Two particles which have no grain boundary between them, resulting in a single crystal in the shape of the original two. The particles are coherent along the $\{400\}$.	108
4.28	Two sintered particles of the γ -phase. The neck is sharply faceted and has a discrete contact angle. The particles seem to have phase transformed into one particle, however closer examination reveals that the $\{311\}$ planes in the right particle do not cross the grain boundary which also appears distinctly. Note the neck surface has reconstructed.	109
4.29	PEELS of alumina of the oxygen K-edge from the UHV (a) and HF2000 (b) microscopes. Their respective first derivative spectra are shown in (c) and (d).	112
4.30	Alumina PEELS from the UHV microscope. The zero loss and plasmon peaks (a), the Al L _{2,3} stripped edge [from EELS Atlas 1983] (b), the Al L _{2,3} (c) and its first derivative in (d).	113
4.31	Two faceted ultrafine particles which have sintered on common $\{111\}$ facets but with mixed edge character. In this case densification, as defined by center-to-center approach, is constrained by the Wulff construction.	118
A1.1	Time sequence of the damage process of α -alumina $[11\bar{2}0]$ zone. The initial surface in (a), after 30 minutes of low flux (10 A/cm^2) damage. After 2 hours of damage (c) the faceting has become more extensive and the surface phase resembles $[112]_{\gamma}$ zone.	139
A1.2	The unit cell crystal structure from a multislice calculation for the $[2\bar{2}01]$ zone of α -alumina (a). The dark-line facets occur along planes in the crystal which are either all aluminum or all oxygen (vertical). The horizontal planes have a mixed character and no faceting is observed there. In (b) the unit cell is viewed along the 'x-axis' and is, in fact, the $[11\bar{2}0]$ zone where faceting occurs along the (0006) planes which have been rotated to the vertical orientation.	141

A1.3	The faceting occurs on almost all crystal orientations in α -alumina. Here the $[2\bar{2}01]$ zone also exhibits facets on planes which are layers of oxygen or aluminum.	142
A1.4	The damage process accelerates at 100 keV in the CTEM. Here, the $[11\bar{2}0]$ zone damages after 90 minutes of medium flux (20 A/cm^2) irradiation.	142
A1.5	The damage process under UHV conditions results in the formation of small crystallites of aluminum. Here, the initial surface of the $[2\bar{2}01]$ zone and after 1 hour of moderate flux (20 A/cm^2) irradiation.	143
A1.6	PEEL spectra of the UFPs in the HF2000. In (a) the spectra of Al L _{2,3} The near-edge structure of the L _{2,3} in (b) and the first derivative of (a) in (c). The stripped edge of aluminum metal (d) from the EELS Atlas (1983).	146
A5.1	The 3 mm cartridge design.	165
A5.2	The sliding O-ring seal design for the collection chamber.	166
A5.3	The specimen collection chamber.	168
A5.4	The electrode chamber.	169
A5.5	The specimen cartridge 'grabber' jaws.	170

Chapter One. Introduction

Ceramics are materials of extreme technological importance, prized for their chemical resistivity, hardness and wear resistance, high melting temperature, and low densities. And yet, the widespread application of these materials has been impeded by their sensitivity to mechanical and thermal shocks as a result of their brittle nature. The relatively poor mechanical properties are usually considered to be the consequence of flaws within the materials which lead to catastrophic failure. Whereas metals may plastically deform, either by the motion of lattice dislocations (Weertmans 1969) or diffusional creep (Herring 1950), to alleviate an applied stress, materials with immobile lattice dislocations are brittle at temperatures where diffusional creep is inoperative (low temperatures).

In recent developments (Karch et al. 1987), ceramic materials have been tailored to accommodate diffusional creep at low temperatures. This is achieved by making the grain size of the polycrystalline ceramic on the order of a few nanometers (nm), hence the name nanocrystalline materials. Nanocrystalline materials deform plastically under an applied stress due to the ease with which the small grains slide past each other.

Another way to view the behavior of nanocrystalline materials is through an analogy to the Hall-Petch (Hall 1951; Petch 1953) relationship in metals which states that the yield stress is related to the grain size as;

$$\sigma = \sigma_0 + f d^{-1/2} \quad (1.1)$$

where σ is the yield stress, σ_0 the lattice friction stress required to move individual dislocations, f a constant, and d the spatial grain size. According to this relationship, a grain size of a few nms should possess improved mechanical properties over a bulk material with grain sizes of several microns.

In the structural regime between bulk ceramic materials and the novel

nanocrystalline properties are the ultrafine-grained materials, i.e. grain sizes about 20-50 nm. Thus, it is conceivable that these ultrafine-grained materials could represent a sort of amalgam, possessing both the advantageous properties of conventional bulk ceramics and the unique and desirable qualities of the nanocrystalline materials. Given that ultrafine-grained ceramic powders can be easily produced, the central questions one has to address are: what is the behavior of these particles as they sinter at elevated temperatures and can this sintering process be understood on an atomic level. In this thesis the process of sintering in ultrafine ceramic particles will be investigated in terms of both the atomic structure and the particle shape considerations. To place this research in its proper context, it is appropriate to discuss the framework of sintering theory in the macroscopic sense and also to review some of the previous sintering developments with ultrafine ceramic particles.

§1.2 Macroscopic Sintering

Sintering is defined (Hausner 1979) as “the process of reducing the interior and exterior surface of a body or of bodies of particles in contact by reinforcement of contact bridges and the reduction of the void volume.” The seminal work on the sintering of materials is that of Kuczynski (1949a,b) who placed spheres of different materials on flat substrates and annealed them at elevated temperatures. Kuczynski then measured the necks that formed between the spheres and plates as functions of both time and temperature. Kuczynski noted that a power law with respect to time was obeyed during sintering. That is, a plot of the logarithm of the neck radius, scaled by the sphere radius, versus the logarithm of the time period yielded a straight line. The slope of this line (the exponent of the time period) was then related to a specific mass transport mechanism responsible for neck growth. Knowledge of the sintering mechanism allows one to then calculate the diffusion coefficients and activation barriers for that particular mechanism.

There are six generally recognized mechanisms of mass transport leading to neck

growth during the solid-state sintering process as shown in Table 1.1.

Table 1.1: Mass transport mechanisms during initial stage sintering.

<u>Mechanism #</u>	<u>Transport Path</u>	<u>Source</u>	<u>Sink</u>
1	Surface Diffusion	Surface	Neck
2	Lattice Diffusion	Surface	Neck
3	Vapor Transport	Surface	Neck
4	Boundary Diffusion	Grain Boundary	Neck
5	Lattice Diffusion	Grain Boundary	Neck
6	Lattice Diffusion	Dislocations	Neck

[from Kingery et al. (1976) where the mechanism number corresponds to Figure 1.1(a)]

Mechanisms 1-3 lead to neck growth during sintering, however, they do not also promote densification as do mechanisms 4-6. Following the pioneering work of Kuczynski, later investigations of sintering behavior used the same method, with improvements in the theoretical treatments, of measuring the neck growth rate as functions of time and temperature and attributing the behavior to a single mechanism indicated by the time exponent. Kingery and Berg (1955) studied the initial stages of sintering for different materials and confirmed that glass spheres sintered by means of a viscous flow mass transport mechanism, NaCl spheres by an evaporation-condensation scheme, and Cu spheres by volume transport. Herring (1950) recognized that the effect of a change of scale with respect to the particle size on the rate of neck growth was dependent upon the mass transport mechanism. Scaling laws were developed which removed the uncertainties in the sintering geometry as assumed by Kuczynski. Coble (1958) sintered alumina and hematite and determined that volume diffusion was the dominant transport mechanism. Coble (1961) later determined that in alumina the sintering was controlled by the bulk diffusion of aluminum cations whereas the oxygen transport occurs along the grain boundaries. Johnson and Cutler (1963a,b) refined the geometrical relations of sintering

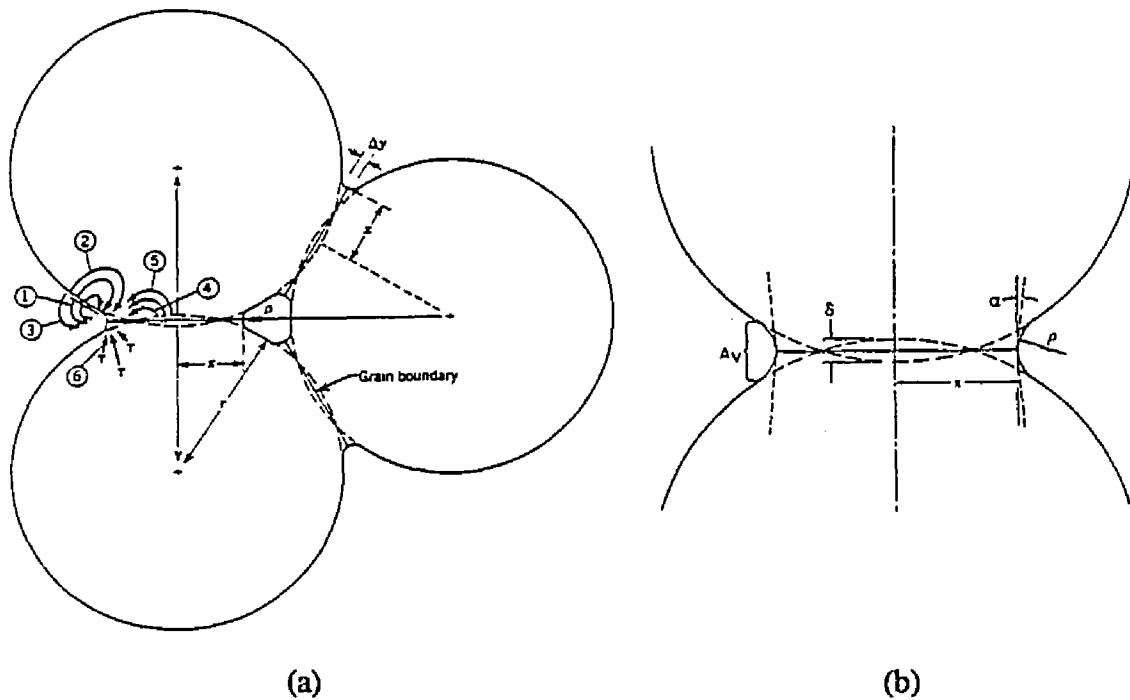


Figure 1.1. (a) Mass transport mechanisms during sintering (from Ashby 1974). (b) The model of Johnson (1969) for competing mechanisms during initial stage sintering.

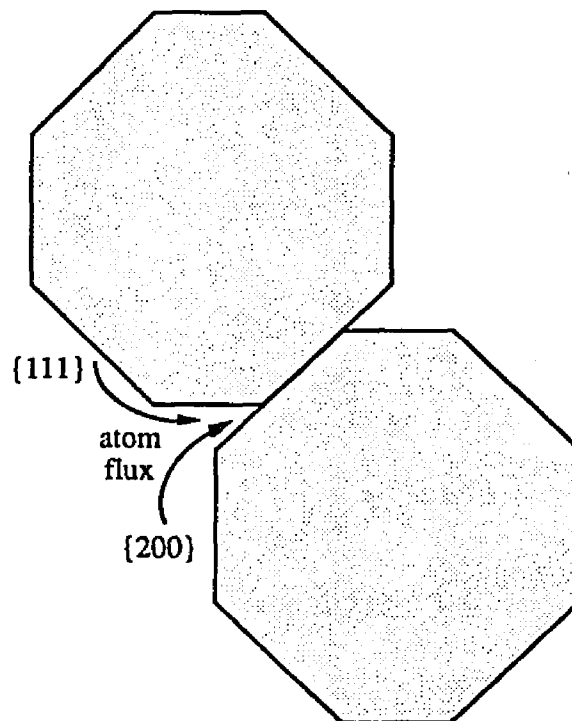


Figure 1.2. Two faceted ultrafine particles that have sintered together along common {111} surfaces. The discrete contact angle of the grain boundary/neck region is evident.

and found that the shrinkage rates measured in powder compacts could be correlated with two-sphere models and that the alumina compacts sintered with grain boundary diffusion as the rate-controlling mechanism. Nichols and Mullins (1965) and Nichols (1966) investigated the role of surface diffusion during sintering and developed a numerical method of predicting the rate of neck growth.

§1.2.1 Two Sphere Model

In a substantial improvement over previous approaches, Johnson (1969) proposed a method by which all the diffusion coefficients (volume, grain boundary, and surface) could be determined from the same neck growth / shrinkage measurements. It has been recognized that during sintering more than one mechanism could contribute to neck growth. Johnson pointed out, more importantly, that these combined mechanisms could result in shrinkage measurements (on a log-log plot) which resembled an entirely different mechanism. The sintering model proposed by Johnson, schematically represented in Figure 1.1(b), handled competing mechanisms by making the following assumptions;

- 1• The sintering bodies have an axis of revolution which is normal to the grain boundary between the particles, i.e the neck has a circular cross-section.
- 2• The surface tension, γ , and grain boundary tensions are isotropic.
- 3• The stress immediately beneath the neck surface near the grain boundary is described by the Gibbs-Thomson equation:

$$\sigma = \gamma[(\cos\alpha/x) - (1/\rho)] \quad (1.2)$$

where σ =stress and $\alpha=(\pi-\beta)/2$.

- 4• Material transport by dislocations is negligible.
- 5• The vacancies are at equilibrium everywhere.
- 6• A quasisteady-state exists, implying that the vacancy migration rate is large

in comparison to the rate of change in geometry.

- 7• The chemical potential gradients for grain-boundary diffusion and volume diffusion to the grain boundary are identical.
- 8• The grain boundary and volume mobilities are independent of radial position in the neck and are isotropic.

These assumptions allowed to Johnson to derive the shrinkage rate in a compact as;

$$\frac{X^3 R}{X + R \cos \alpha} \dot{y} = \frac{2\gamma \Omega D_v}{\pi k T a^3} \frac{A_v}{X} + \frac{4\gamma \Omega b D_b}{k T a^4} \quad (1.3)$$

where $X = x/a =$ radius of neck/radius of sphere

$R = r/a =$ minimum radius of curvature of neck/radius of sphere

$\Omega =$ atomic volume for diffusion

$\dot{y} =$ shrinkage rate

$A_v =$ neck surface area/square of sphere radius

$\gamma =$ surface tension

$b =$ width of the region of enhanced diffusion at the grain boundary

$D_v =$ volume diffusion coefficient

$D_b =$ grain boundary diffusion coefficient

A plot of $[X^3 R / (X + R \cos \alpha)] \dot{y}$ versus (A_v / X) has a slope containing the volume diffusion term and the intercept contains the boundary diffusion term, $b D_b$. Once these terms were known, the surface diffusion coefficient could be determined.

§1.2.2 Analysis of Assumptions

While Johnson's model describes the sintering of two large spheres, when it is extended to ultrafine particles (UFPs) a number of the assumptions can no longer be considered valid. For example, ultrafine particles have surface facets which depend upon

the crystal structure and orientation. This result is not surprising given the fact that such faceting has been reported (Herring 1953) in sintering of wires to flat plates. In this case, there was some concern as to whether the macroscopic facets actually represented unstepped surfaces, their absence precluding a mechanism for step growth.

Surface faceting means that we can not assume that the surface tension is isotropic. Indeed, the surface faceting in UFPs is decidedly anisotropic. Furthermore, the use of the term 'surface tension' as applies to a solid is really a misnomer. The implied usage in eqn. 1.2 is the *reversible work* to create new surface by stretching (i.e. surface stress), which must be distinguished from the surface energy (Linford 1973). Surface energy, or more specifically the excess surface free energy, will control the shape of the UFPs due to the Wulff construction (§4.1.3) and will also be highly anisotropic.

The distinction between surface stress and surface energy is a rather important point. If we define the surface stress, g , in terms of purely elastic strains, ϵ , as (Howie and Marks 1984);

$$g_{ij} = - \frac{\partial E}{\partial \epsilon_{ij}} \quad (1.4)$$

where E is the free energy of the system, then it can be shown that the value of g_{ij} depends upon the potential used. For example, if a Lennard-Jones potential is assumed (which is good for the noble gases) g_{ij} is negative meaning the surface will expand (tensile stress). For the case of metals, g_{ij} is positive meaning the surface wants to contract (compressive stress). However, in either situation the surface energy, γ_{ij} , is *always* a positive quantity.

The existence of faceted surfaces affects the assumptions about isotropic diffusion coefficients and mobilities, they will also be highly anisotropic in nature. An important point to note is that with UFPs, the surface to volume ratio is large. Consequently, the sintering behavior will be dominated by their surfaces. That is, the surfaces will act as the 'short-circuit' diffusion path and one would expect surface diffusion to contribute more to

sintering than volume diffusion. Furthermore, the neck region between the particles (where two surface facets come together) will not have a radius of curvature, see Figure 1.2. Thus the Gibbs-Thomson equation is not valid for the case of UFPs.

Additional considerations are of an experimental nature. For example, in sintered compacts the neck is measured as it grows from a 'point' contact to larger and larger toroidal surfaces. However, in the case of ultrafine particles with faceted surfaces, the initial 'neck' region will begin with a large interfacial area which may also have a specific crystalline orientation. This means that the neck growth rate will be difficult to quantify in an exact manner. Furthermore, both elastic and plastic deformations due to contact stress in ultrafine particles, as is the case with metals (Tholen 1979), could give an initial neck which is not the consequence of the sintering process.

§1.2.3 Rotating Spheres-on-Plates

The matter of particle rearrangement during sintering to low energy configurations can be addressed by considering the rotating sphere-on-a-plate experiments of Gleiter and company (e.g. Herrmann et al. 1979). In these experiments, small single crystal spheres of a material, usually a metal, are randomly distributed about the surface of a flat single crystal substrate and are sintered at elevated temperatures for long periods of time. The neck that develops between each sphere and the substrate contains a grain boundary. If the degree of misorientation between the sphere and substrate is large, the grain boundary exerts a sizable torque on the sphere causing it to rotate to a local energy cusp, or minimum.

Erb and Gleiter (1979) sintered spheres of Cu to a [110] oriented Cu substrate and varied the sintering temperature. At 750°C it was determined that many local minima existed indicating that only small rotations were necessary to achieve a stable configuration. However upon heating to 1050°C, the number of stable energy cusps was dramatically

reduced leading to only a few specific sphere rotations. Mykura (1979) also investigated this behavior for small Cu spheres and determined that a rolling translation was indeed significant and was ascribed to grain boundary sliding during sintering. Kuhn et al. (1979) experimentally determined the energy-misorientation relationship for Cu and found that no localized dislocation model could describe the structure of the grain boundary. A question that remained from these experiments was whether the grain boundary could be characterized as crystalline or 'melted' as the means to allow for sphere rotation. However, Balluffi and Maurer (1988) investigated the behavior of high-angle grain boundaries and determined that even with high misorientations, the grain boundaries were crystalline. That is, no melting occurs until T_m is reached and the grain boundary sliding mechanism is the correct interpretation.

§1.3 Ultrafine Particle Sintering

In the regime of ultrafine particles of alumina, much work has been done. Vergon et al. (1970) studied the initial sintering in UFPs of δ -alumina. They made the powders of various particle sizes into greenform compacts, sintered them over the temperature range 1050°C to 1400°C for short periods of time and measured bulk shrinkage rates. Such experiments resulted in a linear variation of the shrinkage rate with time and was associated with a mechanism of diffusional creep of Nabarro and Herring. However, since phase transitions (i.e. from δ to α) are expected in this temperature regime, and this was not included in their analysis, the result of linear time dependence of shrinkage may be inaccurate.

Raman et al. (1984) characterized the initial sintering in γ and α -aluminas of a few tens of nms in diameter. In α - Al_2O_3 , they attributed the sintering behavior to Coble creep and grain boundary diffusion of oxygen. In the case of γ - Al_2O_3 , the mechanism was aided by the transformation of γ to α involving dislocation climb causing the γ to densify

more than α at 1800°C. Subsequent investigations by Raman et al. (1986) by means of transmission electron microscopy and selected area diffraction resulted in evidence for plastic deformation assisted sintering behavior.

Lis and Pampuch (1986) investigated the role of surface diffusion in the sintering of micropowders and concluded that conventional two-body models were insufficient to explain the experimental data. Their approach was that the shrinkage rate was increased when the pores in a powder compact had a lower coordination number and that since surface diffusion usually results in coalescence, the small particles will help the sintering process. This approach dovetails neatly with the idea of Lange (1984) that the sinterability of a powder depends upon the pore coordination number and that only those pores with coordination less than a critical number will shrink, kinetics permitting. Lange (1986) later provided thermodynamic arguments for the shrinkage of pore space in powder compacts by considering the arrangement of random arrays of polyhedra. Optimum sinterability was determined to occur for particle arrangements that are periodic in nature.

Previous microscopy studies of the sintering behavior were conducted by Iijima (1984, 1985) and Warble (1985). These researchers independently produced UFPs of aluminum oxide by arc discharge methods for sintering experiments. Iijima noticed the formation of new alumina phases (see Chapter Four, Tables 4.1 and 4.2) and sintered the UFPs under vacuum at 1350°C for 2 hours. However, only a few examples of sintering were shown and the resulting interfaces (grain boundaries) between particles was considered to be atomically irregular. Warble sintered UFPs of alumina at atmosphere at 1150°C for 48 hours and noted that the γ -phase particles had transformed to the α -phase in a "plate and block" arrangement.

§1.4 Role of Contamination

In all of the preceding discussion, no mention was made concerning the role of

impurities on the properties of these materials. However, the large surface to volume ratios found in the UFPs and the fact that many properties are surface-controlled mandates that the extrinsic effects of impurities be carefully scrutinized. For instance, there is considerable debate over whether the Hall-Petch relation can be extended down to grain sizes typically found in UFPs and nanocrystalline materials. Neiman et al. (1989a,b) have reported that nanocrystalline Cu and Pd samples do exhibit Hall-Petch behavior and that no appreciable grain boundary diffusional creep was observed. However, Chokshi et al. (1989) have contradictory evidence in nanocrystalline Cu and Pd reporting a *negative* Hall-Petch relationship and substantial diffusional creep resulting in grain boundary sliding.

Clearly contamination is the defining factor in the discrepancy between these results as the materials systems are the same, and the samples are presumably prepared and tested in a similar manner. The impurities in these systems may act to either 'embrittle' or 'lubricate' the grain boundaries in these nanocrystalline materials; i.e. the behavior is controlled by extrinsic properties. The existence of impurities can also have a dramatic effect on the thermodynamics of surfaces and the rates of surface diffusion (Somorjai 1972). For example, adsorption on surfaces can result in a negative surface stress (Howie and Marks 1984).

In no previous study of UFP sintering behavior have the issues presented by contamination been adequately handled. Iijima (1985) did mention that the vacuum level present during observation of the UFPs was about 10^{-6} Pa. However, the important factor is not the overall vacuum level, but the *cleanliness* of the entire system; this will control the observed behavior. From the onset of this study, a determined effort was made to insure the cleanliness of the entire UHV system, which includes a furnace, a transfer system and a UHV-HREM. The goal here was to at least minimize, if not completely eliminate, any contaminating species during the particle formation and sintering processes.

Chapter Two. Imaging Theory and Techniques

§2.1 Elemental Electron Microscopes

Electron microscopy has been for years the technique of choice to investigate the structural properties of materials providing a wealth of information on a very localized scale. This section will give a brief explanation of the operations of the microscope and its various function modes, following the introduction of Hirsch et al. (1977).

The basic electron microscope elements consist of an electron gun, a series of apertures and electromagnetic lenses, and an imaging system. In older microscopes, the electron gun has a tungsten filament, however in newer microscopes LaB₆ crystals, which have higher intensity and longer life, are routinely employed. The thermionically emitted electrons are then accelerated to the desired potential where they enter the condenser (or illumination) lens system. The H9000 series has three condenser lenses: the first lens, C1, controls the beam spot size and is associated with the fixed condenser aperture. Using larger spot sizes gives higher brightness (intensity) illumination, but at the expense of resolution. The C2 lens is the brightness control and is used to either focus or spread out the illumination. This lens is associated with an adjustable aperture (CA) that controls the degree of beam convergence. Larger apertures increase both the beam convergence and intensity and, ultimately, decrease the resolution. The third condenser lens, CAUX, situated between C1 and C2 is a probe forming lens whose excitation, in conjunction with C1, forms a smaller beam size and is useful in microdiffraction studies.

Once the illuminating beam is formed, the electrons enter the all-important objective lens. This lens is the most highly excited and thus strongly focuses the electrons which pass through and are diffracted by the specimen. The objective lens is also associated with an aperture (OA) whose adjustable size allows the user to operate the microscope in

several imaging modes to be described in more detail in later sections. Ideally, the objective lens is designed such that the specimen, sitting midway between the pole pieces, is also at the optimum position to achieve the highest resolution. That is, the ultimate resolution is altered if the specimen does not lie at the optimum height in the lens. When tilting a specimen for proper crystal orientation the height is changed and, in the extreme case, the ultimate resolution is reduced. There are several means to correct changing specimen height. An eucentric stage can be used where the tilt occurs about a fixed axis. A Z-adjust stage, whereby the specimen height is changed to bring the image into focus, allows the specimen to be imaged at constant, and optimum, objective lens excitation.

The selected area aperture (SAA) follows the objective lens. In selected area (SA) mode, the image is focused such that the aperture lies in the back-focal plane (BFP) of the objective lens. This allows the user to obtain diffraction patterns (DP) from the specimen area contained within the aperture. It is essential that the SAA and the BFP coincide to ensure that only those beams diffracted by the desired specimen region are obtained in the DP. Following the OL and SAA are the intermediate and projector lens systems (PL). These lenses are mainly used during high resolution work to change the magnification of the image. Typically, these lenses are designed such that as the magnification changes, there is no image rotation.

Finally, the electrons from the specimen come to the imaging system consisting of a phosphor viewing screen beneath which lie photographic film plates for image recording and perhaps a TV camera. The photographic film typically used is a fine-grained, high sensitivity film with exposure times for high resolution work of 4-6 seconds. A relatively recent advance in microscope technology has been the development of TV cameras that have sufficient response and signal-to-noise for use in high resolution imaging. The current method combines the TV camera (running at 30 frames/sec) with a computer

controlled frame buffer to digitally acquire images which may then be numerically 'massaged' with commercially available image processing routines. Typical TV cameras employ YAG scintillators fiber optically-coupled with an image intensifier, though recently the use of charged coupled device (CCD) cameras have gained widespread acceptance. In fact, developers of CCD technology (Gatan Inc., and others) foresee a future where images are digitally recorded avoiding the necessity of using photographic film and the chemical darkroom.

Lens Aberrations

Since the electron source and electromagnetic lenses are not perfect, certain errors are introduced which are passed along with the electrons to the final image, i.e. spherical and chromatic aberrations. Fortunately, they can be accounted for as follows. Spherical aberration arises when electrons travelling through the outer periphery of the lens are more strongly focused than those which pass through the center of the lens. The effect is shown schematically in Figure 2.1.

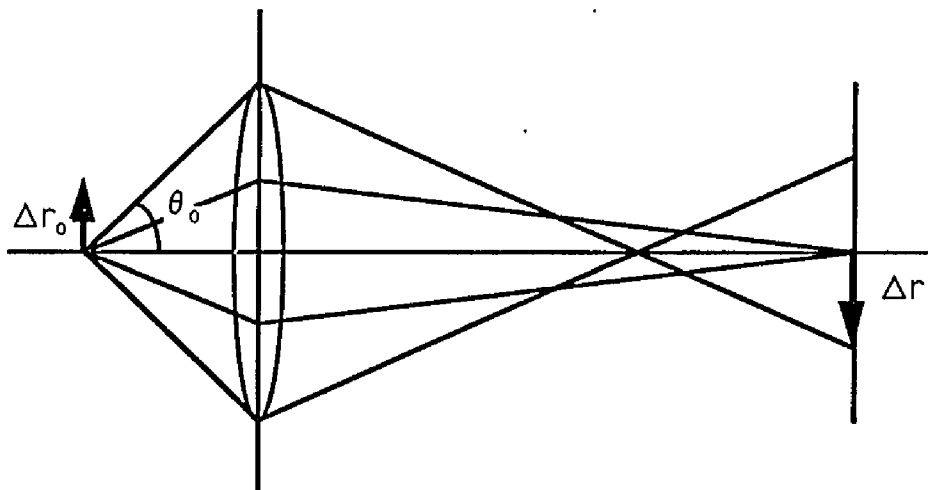


Figure 2.1. The effect of spherical aberration on the Gaussian image. The electrons passing through the outer zone of the lens are more strongly focused.

The radius of 'least confusion' is expressed as;

$$\Delta r_o = \frac{1}{4} C_s \theta_o^3 \quad (2.1)$$

where the lens object scatters the aberrated electrons by an angle θ_o and C_s is the spherical aberration coefficient of the lens. Since the objective lens is the most strongly excited, and C_s is a function of the excitation, the C_s of the OL sets the limit on the 'interpretable' resolving power of the microscope.

Chromatic aberration arises from the fact that the focal length of the electromagnetic lens is a function not only of lens excitation (i.e. current) but the wavelength of the electrons being focused. Thus, the following instabilities in the microscope system cause chromatic aberration: the energy distribution of electrons leaving the filament and changes in the electron energy (wavelength) due to high voltage instabilities, and instabilities in the objective lens excitation. It is convenient to group the voltage and lens instabilities together such that the change in the focal length, f , is;

$$\frac{\Delta f}{f} = \frac{\Delta V_o}{V_o} - \frac{2\Delta I}{I} \quad (2.2)$$

where the chromatic aberration, C_c , is defined as $C_c = Kf$. Then we can further define a radius of 'least confusion' as;

$$\Delta r_o = \theta_o C_c \left(\frac{\Delta V_o}{V_o} - \frac{2\Delta I}{I} \right) \quad (2.3)$$

as represented schematically in Figure 2.2. The effect of these aberrations on the final microscope image is developed in the section on the transmission cross-coefficient used in contrast transfer theory.

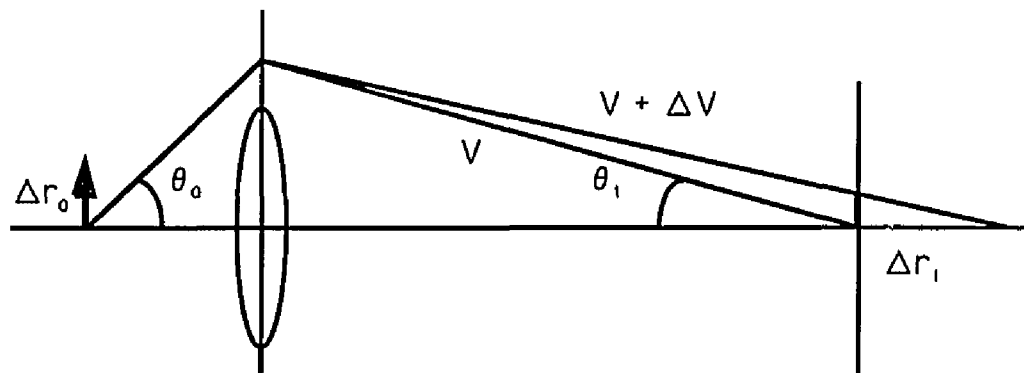


Figure 2.2. The effect of chromatic aberration where electrons of higher energy are not as strongly focused given a constant lens excitation.

§2.2 Electron Optics

As mentioned above, the electron microscope is a system of electromagnetic lens which focus and image the electrons diffracted by the specimen. And given that electrons behave as waves as well as particles, it is appropriate to understand elemental electron optics as applied to microscopes. This section is by no means a full quantum mechanical treatment of electron-optical theory, i.e. Hall (1966), nor is it intended to be. However it is useful to develop some of the relations particularly as they become important in understanding how the electrons are transferred to the high resolution image. In fact, in this respect it is approximately correct to treat the electrons by classical wave optics whereby the electromagnetic lenses are considered as ideally thin.

The electrons which produce the final image can be treated in three different stages. First the electrons leave the gun, a point source, and are focused by the illumination system (C1, C2, CA, etc.) into the incident wavefunction (a plane wave). The wavefunction then reaches the specimen where it is transformed by the complex interaction of the electrons with the crystal potential. The exit surface wavefunction from the specimen thus contains all of the structural information through which the electrons have traversed. Finally, the exit wavefunction is further transformed by the imaging system (OL and PL) into the final

image viewed on the screen. We will be most concerned with the last process where the electrons are transferred to the final image. The complex interaction of the electrons and the specimen can be understood by a matrix formulation the n-beam dynamical scattering process and will be described in a later section on multislice image calculation.

In the typical treatment of electron optics, following the method of Spence (1988) the concepts of entrance and exit pupils are introduced to represent the diffraction limit of the microscope. In this way, the lens aberrations can be considered as phase shifts across the exit pupil on the converging spherical wavefront (incident electrons). For the OL, the OA acts as the exit pupil with the intensities of the electron diffraction pattern being the intensities across the objective BFP. Most important is the relationship between the wavefunction at the BFP and the complex exit-face wavefunction, and the relation between the image wave function and the BFP wavefunction. This is done using the Fourier optics approach based on the Abbe theory whereby the image is comprised from the Fourier summation of all the diffracted beams contained within the OA. The image is formed by taking the Fourier transform of the exit wavefunction to get the BFP wavefunction and then once again to obtain the image wavefunction, which includes the appropriate microscope aberrations.

The Gaussian focus condition is the OL excitation that focuses the lens on the exit face of the specimen where the various waves produced by scattering in the specimen have emerged. In a kinematical treatment these waves have not yet interacted, and so if the OL is focused at this point, no interference pattern will be observed. Of course, in a real material there will be dynamical interactions resulting in interference between scattered waves. In this case, there exists an interference pattern at Gaussian focus but, fortunately, the resulting contrast is small. In order to image the interference pattern of the exit wavefunction, the OL must be defocused by a certain amount and the coherent interference

pattern is imaged from the 'out-of-focus' plane located at a distance Δz from the exit surface of the specimen, e.g. Figure 2.3.

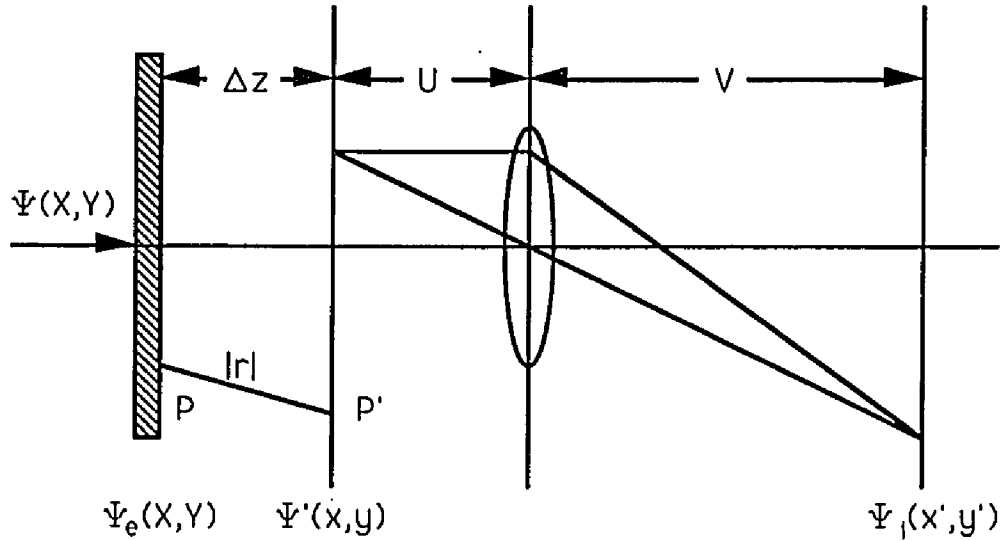


Figure 2.3. Production of the 'out-of-focus' image of a specimen by defocusing the objective lens. The image wave amplitude $\Psi_i(x', y')$ is formed by a convolution of the wave amplitude at the 'out-of-focus' plane through the imaging system of the microscope.

From Huygen's principle the wave amplitude at a point P' is

$$\begin{aligned}
 \Psi(x, y) &= \frac{i}{\lambda \Delta z} \iint \Psi_e(X, Y) \exp\left(-\frac{2\pi i |r|}{\lambda}\right) dXdY \\
 &\approx \frac{i \exp\{-2\pi i \Delta z / \lambda\}}{\lambda \Delta z} \\
 &\times \iint \Psi_e(X, Y) \exp\left(-\frac{i\pi}{\lambda \Delta z} \{(x-X)^2 + (y-Y)^2\}\right) dXdY
 \end{aligned} \tag{2.5}$$

where Δz is the OL defocus, λ the relativistic electron wavelength (0.01968 Å for 300 keV), X and Y the components in the 2D plane perpendicular to the optic axis, and the integrals are over all space. By neglecting all aberrations, eqn. 2.5 can be used to calculate the 'out-of-focus' image provided that Ψ_e is known. Written as a convolution

$$\begin{aligned}\Psi(x,y) &= A \Psi_e(x,y) * P_z(x,y) \\ &= A \iint \Psi_e(X,Y) P_z(x-X, y-Y) dXdY\end{aligned}\quad (2.6)$$

where A is a complex constant and

$$P_z(x,y) = \exp\left(-\frac{i\pi(x^2 + y^2)}{\lambda\Delta z}\right)\quad (2.7)$$

is the Fresnel propagator. This term is simply the phase shift that occurs in the exit face wavefunction as it propagates across a defocus distance Δz .

Now that the Fresnel propagator is introduced, we can trace the progress of the wavefunction through the lens system. Assuming a unit amplitude, coherent illumination on an object with transmission function $T(x,y)$, the wavefunction incident on the lens is

$$\Psi_1(x_1,y_1) = \frac{i}{\lambda U} T(x,y) * P_u(x,y)\quad (2.8)$$

with the wave immediately behind the lens equal to

$$\Psi_2(x_2,y_2) = \Psi_1(x_2,y_2) \exp\left(\frac{i\pi[x_2^2 + y_2^2]}{\lambda z}\right)\quad (2.9)$$

leading to a complex amplitude in the BFP given by

$$\Psi_d(u,v) = \frac{i}{\lambda z} \Psi_2(x_2,y_2) * P_z(x_2,y_2)\quad (2.10)$$

Evaluating these integrals and using eqn. 2.7 gives

$$\Psi_d(u,v) = \frac{i}{\lambda z} \exp\left(-\frac{i\pi(u^2 + v^2)}{\lambda z}\right) \left(\frac{1}{z} - \frac{U}{z^2}\right) \times \iint \Psi_0(x,y) \exp\left(2\pi i \left(\frac{u}{\lambda z} x + \frac{v}{\lambda z} y\right)\right) dx dy \quad (2.11)$$

Since Δz is small, U will be approximately equal to z and thus the quadratic phase factor will disappear. Thus we see that a function proportional to the Fourier transform of Ψ_e results in the BFP of the lens. This result agrees with the Abbe interpretation of coherent imaging. Parallel rays leaving the specimen at an angle θ will be focused at a point a distance X from the optic axis where $X=z\theta$; the Fourier transform (FT) of a plane wave (or set of lattice planes) is a delta function (spot). Therefore, the diffraction pattern consists of a set of point amplitudes if the illumination is coherent. These points can be considered as secondary sources that will produce fringes (the Fourier synthesis of all fringes is the image). Eqn. 2.11 can be rewritten as

$$\Psi_d(u,v) = \frac{Ai}{\lambda z} F(u,v) \quad (2.12)$$

which is the BFP wavefunction and

$$F(u,v) = \iint \Psi_0(x,y) \exp\{2\pi i(ux + vy)\} dx dy = FT\{\Psi_0(x,y)\} \quad (2.13)$$

where $u = X/\lambda z = \theta/\lambda$ and $v = Y/\lambda z = \gamma/\lambda$ with θ and γ being angles with the optic axis.

§2.3 Contrast Transfer Theory

Now that the BFP wavefunction has been derived, the conventional approach is to introduce a phase shift that operates on the BFP wavefunction. This phase shift, $\chi(u)$, contains the effects of the lens defocus and spherical aberration. The form of $\chi(u)$ is the

essence of contrast transfer theory. In this respect, the electron microscope is treated as a finely tunable filter of spatial frequencies, \mathbf{u} , the information from the specimen transmitted to the high resolution image being a function of the attenuation of this filter. The nature of the transmission of the exit-surface wavefunction to the image has been exhaustively studied by many authors with various approximations. Given here is a brief summary of concepts and terminology used in imaging theory. In linear theory, the specimen weakly scatters the electrons thus forming the image by interference of diffracted beams with the transmitted beam. The diffracted beams are considered to be of weak intensity. Consequently, the exit wave is expressed as;

$$\Psi(\mathbf{u}) = 1 - s(\mathbf{u}) + i \phi(\mathbf{u}) , \quad (2.14)$$

where $s(\mathbf{u})$ is the amplitude scattering of spatial frequency \mathbf{u} , $\phi(\mathbf{u})$ the phase scattering and $s, \phi \ll 1$. In this case we can define a contrast transfer function linking the Fourier transform of the final intensity to the Fourier transform of the wave leaving the specimen. Non-linear theory refers to the situation where the specimen strongly scatters the electrons. In this case the diffracted beams have sufficient intensity that in addition to interfering with the transmitted beam, they can interfere with each other.

As presented by Frank (1973) and Wade and Frank (1977), the linear contrast transfer theory can be written in terms of the product of the unmodified transmission cross-coefficient function and two envelope functions due to spatial and temporal coherence. Subsequent investigations by Jenkins and Wade (1977) and Wade and Jenkins (1978) developed the contrast transfer theory considering conical and tilted bright-field illumination. A closed-form representation of both amplitude and phase transmission was presented by Hawkes (1980), however only the zeros of the transmission functions were investigated and the envelope terms were not developed.

While linear contrast transfer theory is adequate for the kinematical diffraction of electrons (a thin amorphous film), extension to strongly scattering objects (a crystalline specimen) can lead to erroneous results. The more accurate non-linear imaging was investigated by Anstis and O'Keefe (1977), Ishizuka (1980) and Pulvermacher (1981) using a first-order Taylor series approximation of the beam convergence (tilt). These authors demonstrated that, with the improved analysis, some periodicities in the image arise from diffracted beam interference rather than from structural periodicities. In principle, this approach can be extended to considering different beams through the crystal, for instance the multislice approach of Coene et al. (1986), implicit in many standard programs.

Non-linear imaging theory can be extended to higher order terms of the beam convergence to develop a more accurate contrast transfer function than the conventional non-linear theory. That is, the work done on linear imaging by Frank (1973) and Wade and Jenkins (1978) can be extended to strongly diffracting crystals (i.e. real materials), instead of being neglected as by Anstis and O'Keefe (1977), Ishizuka (1980) and Pulvermacher (1981). This approach was taken by Bonevich and Marks (1988, 1990a) by considering the full expansion of the transmission cross-coefficient rather than expanding the Taylor series approximations.

If we consider the plane wave leaving the exit surface of the specimen $\Psi(\mathbf{r})$ in real space as having a Fourier transform $\Psi(\mathbf{u})$ in reciprocal space, the image intensity can be represented in real space as;

$$I(\mathbf{r}) = \text{FT}^{-1} \iint \Psi(\mathbf{u}) \Psi^*(\mathbf{u} - \mathbf{v}) \times \text{TCC}(\mathbf{u}, \mathbf{u} - \mathbf{v}, \Delta z) d^2\mathbf{u} , \quad (2.15)$$

where FT^{-1} is the inverse Fourier transform over \mathbf{u} , \mathbf{u} and \mathbf{v} the spatial frequency vectors with moduli u and v and are defined in the 2D planes perpendicular to the optic axis, $\Psi^*(\mathbf{u})$

the complex conjugate of $\Psi(\mathbf{u})$, and $\text{TCC}(\mathbf{u}, \mathbf{u} - \mathbf{v}, \Delta z)$ the transmission cross-coefficient (Frank 1973) due to the phase shift of spatial frequencies and the lens defocus. The transmission cross-coefficient can be expressed as;

$$\begin{aligned} \text{TCC}(\mathbf{u}, \mathbf{u} - \mathbf{v}, \Delta z) &= \iint a(\mathbf{u}, \mathbf{q}) \exp[-i \chi(\mathbf{u}) + i \chi(\mathbf{q})] \\ &\quad \times F(\mathbf{f}) S(\mathbf{w}) d\mathbf{f} d\mathbf{w} \end{aligned} \quad (2.16)$$

where $\mathbf{q}=\mathbf{u}-\mathbf{v}$, $a(\mathbf{u}, \mathbf{q})$ is the objective aperture pupil function, $\chi(\mathbf{u})$ and $\chi(\mathbf{q})$ the phase shifts in reduced units, and $F(\mathbf{f})$ and $S(\mathbf{w})$ the one- and two-dimensional distributions of the focal spread and convergence, respectively. This assumes implicitly that variations in the diffraction condition with changes in beam angle are negligible. Hereafter, the aperture function is assumed to be unity and the astigmatism fully corrected. Note: in reduced units, $\Delta z=(C_s\lambda)^{-1/2}\Delta z^*$ and $\mathbf{q}=(C_s/\lambda)^{1/4}\mathbf{q}^*$ where the asterisk denotes the actual unit.

§2.3.1 Conventional Non-linear Theory

In conventional non-linear theory, given by Spence (1988) and Reimer (1984), the phase shift of individual spatial frequencies is approximated by a Taylor series expansion;

$$\chi(\mathbf{u}, \mathbf{f}, \mathbf{w}) = (\pi/2)[2(\Delta z + f)|\mathbf{u} - \mathbf{w}|^2 + |\mathbf{u} - \mathbf{w}|^4] \quad (2.17)$$

$$= \chi(\mathbf{u}, 0, 0) + \mathbf{w} \cdot \nabla \chi(\mathbf{u}, 0, 0) + \pi f u^2, \quad (2.18)$$

where Δz is the lens defocus, f the focal spread, \mathbf{w} the beam tilt or convergence, and $\nabla \chi$ the gradient of χ . While eqn. (2.17) is exact, eqn. (2.18) relies on two assumptions: the amount of convergence is so small that only the first-order Taylor series term need be considered, and the cross-terms between the focal spread, f , and the convergence, \mathbf{w} , can be neglected (Wade and Frank 1977).

Assuming that the focal spread and convergence have Gaussian distributions the transmission cross-coefficient becomes;

$$\begin{aligned} \text{TCC}(\mathbf{u}, \mathbf{q}, \Delta z) = & \iint \exp\{i [\chi(\mathbf{q}) - \chi(\mathbf{u}) + \mathbf{w} \cdot (\nabla\chi(\mathbf{u}) - \nabla\chi(\mathbf{q})) \\ & + \pi f(u^2 - q^2)]\} F(f) S(\mathbf{w}) df d\mathbf{w} , \end{aligned} \quad (2.19)$$

with

$$F(f) = \sqrt{\beta/\pi} \exp(-\beta f^2) \quad (2.20)$$

$$S(\mathbf{w}) = (\alpha/\pi) \exp(-\alpha w^2) , \quad (2.21)$$

where β and α are related to the rms widths of the focal spread and convergence, respectively. Integrating eqn. (2.19) results in;

$$\begin{aligned} \text{TCC}(\mathbf{u}, \mathbf{q}, \Delta z) = & \exp\{i [\chi(\mathbf{q}) - \chi(\mathbf{u})]\} \\ & \times \exp(-|\nabla\chi(\mathbf{u}) - \nabla\chi(\mathbf{q})|^2/4\alpha) \\ & \times \exp[-\pi^2(u^2 - q^2)^2/4\beta] , \end{aligned} \quad (2.22)$$

the conventional non-linear transmission cross-coefficient. The first term is simply the phase shift of spatial frequencies due to the OL, it is an oscillatory function with the real component being the amplitude transfer and the imaginary component the phase transfer. The second and third terms represent the envelope functions due to spatial and temporal coherence, respectively. These envelope terms act to damp the transfer of high spatial frequencies and impose an ultimate resolution for given microscope parameters. For example, the convergence damping term may be reduced by using smaller condensor apertures (small α) while the focal spread may be reduced by means of LaB₆ filaments (rms of 80 Å) as opposed to tungsten (120 Å).

§2.3.2 Improved Non-linear Theory

If one uses the full expansion of $\chi(\mathbf{u}, f, \mathbf{w})$ instead of the Taylor series, then eqn. (2.17) becomes;

$$\begin{aligned} \chi(\mathbf{u}, \mathbf{f}, \mathbf{w}) = & (\pi/2)\{2(\Delta z + f)[u^2 - 2\mathbf{u} \cdot \mathbf{w} + w^2] \\ & + [u^4 + 2u^2w^2 + w^4 - 4\mathbf{u} \cdot \mathbf{w}(u^2 + w^2) + 4|\mathbf{u} \cdot \mathbf{w}|^2]\}, \end{aligned} \quad (2.23)$$

where a similar expression can be used for $\chi(\mathbf{q}, \mathbf{f}, \mathbf{w})$. Eqn. (2.19) now becomes;

$$\begin{aligned} \text{TCC}(\mathbf{u}, \mathbf{q}, \Delta z) = & \iint \exp\{(i \pi/2)\{2(\Delta z + f) \\ & \times [q^2 + 2\mathbf{w} \cdot (\mathbf{u} - \mathbf{q}) - u^2] + [q^4 - 2w^2(u^2 - q^2) - u^4 \\ & + 4\mathbf{w} \cdot (u^2\mathbf{u} - q^2\mathbf{q}) - 4(|\mathbf{u} \cdot \mathbf{w}|^2 - |\mathbf{q} \cdot \mathbf{w}|^2) \\ & + 4w^2\mathbf{w} \cdot (\mathbf{u} - \mathbf{q})]\}\} \times \sqrt{\beta/\pi} \exp(-\beta f^2) df \\ & \times (\alpha/\pi) \exp(-\alpha w^2) dw. \end{aligned} \quad (2.24)$$

If we first integrate over f the focal spread envelope term becomes;

$$\exp\{-(\pi^2/4\beta)[q^4 - 2u^2q^2 + u^4 - 4\mathbf{w} \cdot (\mathbf{u} - \mathbf{q})(u^2 - q^2) + 4|\mathbf{w} \cdot (\mathbf{u} - \mathbf{q})|^2]\} \quad (2.25)$$

As in conventional non-linear theory, the cross-terms between the focal spread and the beam convergence can be neglected (Wade and Frank 1977) giving;

$$\exp\{-[\pi^2(q^2 - u^2)^2/4\beta]\}. \quad (2.26)$$

The remaining terms in eqn. (2.24) can be integrated by means of a convolution of two perpendicular integrals based on the vector $\mathbf{v} = \mathbf{u} - \mathbf{q}$. This results in an analytical solution (Bonevich and Marks 1988) for $\text{TCC}(\mathbf{u}, \mathbf{q}, \Delta z)$;

$$\begin{aligned} \text{TCC}(\mathbf{u}, \mathbf{q}, \Delta z) = & \exp[-i \chi(\mathbf{u}) + i \chi(\mathbf{q})] \times \exp\{-[\pi^2(q^2 - u^2)^2/4\beta]\} \\ & \times \exp\{-[\nabla \chi(\mathbf{u})\cos\theta_2 - \nabla \chi(\mathbf{q})\cos\theta_3]^2 \\ & / 4[\alpha + i \pi(u^2(1 + 2\cos^2\theta_2) - q^2(1 + 2\cos^2\theta_3))]\} \\ & \times \exp\{-[\nabla \chi(\mathbf{u})\sin\theta_2 + \nabla \chi(\mathbf{q})\sin\theta_3]^2 \\ & / 4[\alpha + i \pi(u^2(1 + 2\sin^2\theta_2) - q^2(1 + 2\sin^2\theta_3))]\} \end{aligned}$$

$$\begin{aligned}
& \times \alpha / ([\alpha + i \pi(u^2(1 + 2\cos^2\theta_2) - q^2(1 + 2\cos^2\theta_3))] \\
& \times [\alpha + i \pi(u^2(1 + 2\sin^2\theta_2) - q^2(1 + 2\sin^2\theta_3))])^{1/2} \quad (2.27)
\end{aligned}$$

While the envelope term for the focal spread is the same as the conventional theory, the convergence envelope term is quite different. For instance, the envelope is now complex and this makes the envelope less effective in damping higher spatial frequencies. Consequently, higher values of the beam convergence do not have the deleterious effect on resolution expected from the conventional non-linear theory. In this analytical solution the cubic term of convergence in eqn. 2.24 was neglected, however it can be included by numerical integration. The TCC with envelopes are shown in Figure 2.4.

§2.3.3 The $\alpha\Delta$ Cross-terms

The analytical solution given in eqn. (2.27) includes the second order terms of the beam convergence but neglects the cross-terms as in Wade and Frank (1977). However, the cross-terms between the focal spread and convergence can also be included in the solution, for mathematical rigor. The following derivation recasts the transmission cross-coefficient in a matrix formulation which is somewhat more elegant (Bonevich 1990).

Starting with the complete equation for the transmission cross-coefficient in reduced units;

$$\begin{aligned}
\text{TCC}(\mathbf{u}, \mathbf{q}, \Delta z) = & \iint \exp\{ (i \pi/2) \{ 2(\Delta z + f)[q^2 + 2\mathbf{w} \cdot (\mathbf{u} - \mathbf{q}) - u^2] \\
& + [q^4 - 2w^2(u^2 - q^2) - u^4 + 4\mathbf{w} \cdot (u^2\mathbf{u} - q^2\mathbf{q}) \\
& - 4(\mathbf{u} \cdot \mathbf{w}|^2 - |\mathbf{q} \cdot \mathbf{w}|^2) + 4w^2\mathbf{w} \cdot (\mathbf{u} - \mathbf{q})] \} \} \\
& \times \sqrt{\beta/\pi} \exp(-\beta f^2) df (\alpha/\pi) \exp(-\alpha w^2) dw \quad . \quad (2.28)
\end{aligned}$$

The constant terms,

$$(\alpha/\pi) \sqrt{\beta/\pi} \exp(i \pi [\chi(\mathbf{q}) - \chi(\mathbf{u})]) \quad (2.29)$$

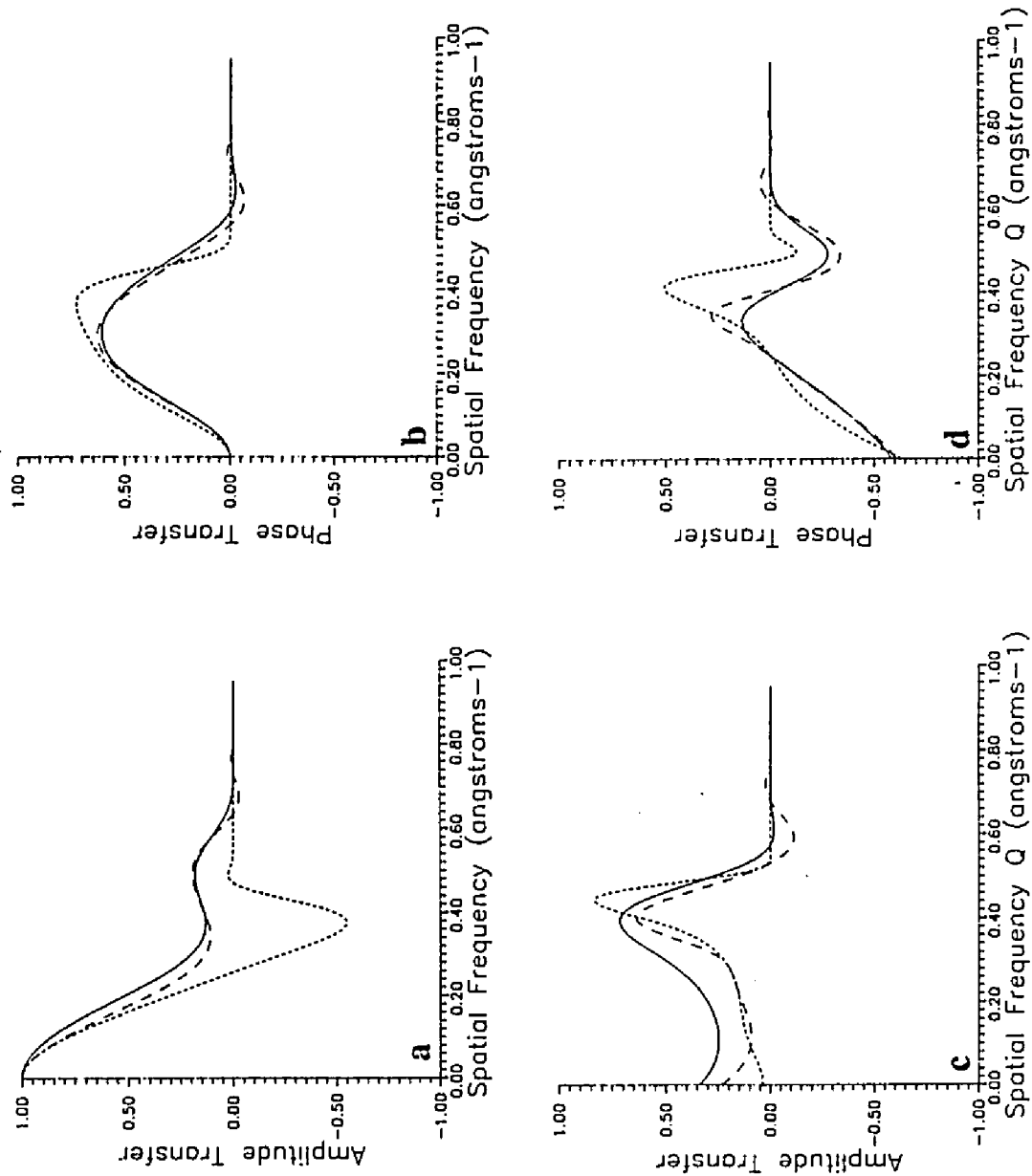


Figure 2.4. Contrast transfer function for linear imaging (a) and (b) and non-linear imaging with g_{100} (0.25 \AA^{-1}) in (c) and (d). In all plots the conventional theory (dashes), JEB/LDM analytical solution (long dashes), and full solution (line) with the conditions of 300 keV, $C_s=0.9 \text{ mm}$, $\Delta z=-500 \text{ \AA}$, rms convergence and focal spread of 3 mrad and 80 \AA .

are removed from the integral. The integral may be represented to second order in x , y , and f as;

$$\iiint \exp[-i (Ax + By + Cf + Dxy + Exf + Gyf) - Hx^2 - Iy^2 - \beta f^2] dx dy df, \quad (2.30)$$

where x and y are the orthogonal components of w as before. Eqn. (2.30) can then be expressed as the vector matrix integral;

$$\iiint \exp \left\{ -\frac{1}{2} [x \ y \ f] W \begin{bmatrix} x \\ y \\ f \end{bmatrix} - i V \begin{bmatrix} x \\ y \\ f \end{bmatrix} \right\} dx dy df, \quad (2.31)$$

$$\text{where } W = \begin{bmatrix} 2H & iD & iE \\ iD & 2I & iG \\ iE & iG & 2\beta \end{bmatrix} \text{ and } V = [A \ B \ C]. \quad (2.32)$$

In this matrix form, we have the following constants;

$$\begin{aligned} A &= - [|\nabla\chi(u)|\cos\theta_2 + |\nabla\chi(q)|\cos\theta_3] \\ B &= - [|\nabla\chi(u)|\sin\theta_2 - |\nabla\chi(q)|\sin\theta_3] \\ C &= \pi[u^2 - q^2] \\ D &= 2\pi[u^2\cos\theta_2\sin\theta_2 + q^2\cos\theta_3\sin\theta_3] \\ E &= -2\pi[ucos\theta_2 + qcos\theta_3] \\ G &= -2\pi[usin\theta_2 - qsin\theta_3] \\ H &= \alpha + i\pi[u^2[1 + 2\cos^2\theta_2] - q^2[1 + 2\cos^2\theta_3]] \\ I &= \alpha + i\pi[u^2[1 + 2\sin^2\theta_2] - q^2[1 + 2\sin^2\theta_3]] \end{aligned} \quad (2.33)$$

where E and G are the cross-terms between beam convergence and the focal spread, the $\alpha\Delta$ interaction (O'Keefe 1979).

The analytical solution of the transmission cross-coefficient integral is,

$$\begin{aligned} \text{TCC}(\mathbf{u}, \mathbf{q}, \Delta z) = & (\alpha/\pi) \sqrt{\beta/\pi} \exp(i \pi [\chi(\mathbf{q}) - \chi(\mathbf{u})]) \\ & \times \sqrt{(8\pi^3/\text{Det } W)} \exp\left(-\frac{1}{2} \mathbf{V} W^{-1} \mathbf{V}^T\right) \end{aligned} \quad (2.34)$$

where $\text{Det } W$ and W^{-1} are the determinant and inverse of W , and \mathbf{V}^T the transpose of \mathbf{V} . The cubic term of the beam convergence is neglected in this solution and, as before, the full solution of the transmission cross-coefficient can be found by numerical integration. The result of these cross-terms is a slight attenuation of the envelope term which is exacerbated by both high focal spread and beam convergence. In the case of conventional HREM imaging mode where α is ≈ 1 mrad and β is ≈ 80 Å these cross-terms have no effect.

§2.4 Multislice Method

In the previous sections, we have treated the electron microscope as an electron-optical system neglecting the complex interactions between the electrons and the specimen. The result of this treatment allows one to evaluate the limitations on resolution imposed by the microscope, however it does not give any indication about the information one actually perceives in the final image. In order to correctly interpret an image, one must be able to also calculate the image numerically taking into full account the electron scattering due to the specimen. The derivation that follows, from the approach of Marks (1987), is called the multislice method and is used by many standard programs to calculate HREM images.

Starting with the Schroedinger equation for electrons travelling through a solid;

$$\nabla^2 \psi(\mathbf{r}) + (8\pi^2 m_e / h^2) [E + V(\mathbf{r})] \psi(\mathbf{r}) = 0 \quad , \quad (2.35)$$

where $V(\mathbf{r})$ is the crystal potential and the remaining notation is in the standard form. Knowing that in electron diffraction the scattering angles are generally small, we can factorize out the wavevector of the incident wave, $|\mathbf{k}| = 1/\lambda$, giving

$$\psi(\mathbf{r}) = \varphi(\mathbf{r}) \exp(2\pi i k z) \quad . \quad (2.36)$$

If eqn. 2.36 is substituted into eqn. 2.35 and apply the fact that

$$\nabla_{\rho}^2 \varphi(\mathbf{r}) = d^2 \varphi(\mathbf{r})/dx^2 + d^2 \varphi(\mathbf{r})/dy^2 \quad , \quad (2.37)$$

and that $(8\pi^2 m_e / h^2) E = 4\pi k^2$, we obtain

$$d\varphi(\mathbf{r})/dz = \varphi(\mathbf{r}) [(i/4\pi k) \nabla_{\rho}^2 + i\sigma V(\mathbf{r})] \quad , \quad (2.38)$$

where $\sigma = 2\pi m_e / h^2 k$ is the interaction constant in kinematical theory. In the simplest approximation, the second order differential terms are neglected in x and y leaving

$$d\varphi(\mathbf{r})/dz = i\sigma V(\mathbf{r}) \varphi(\mathbf{r}) \quad , \quad (2.39)$$

which has the solution

$$\varphi(\mathbf{r}) = \varphi(x, y, z=0) \exp(i\sigma \int_0^z V(\mathbf{r}) dz) \quad , \quad (2.40)$$

where the crystal has a thickness t. This solution is the phase grating approximation since the crystal acts only to change the phase of the wave.

In the multislice algorithm (an extension of the phase grating approach), the full integral in eqn. 2.40 is broken down into smaller integrals where the crystal potential $V(\mathbf{r})$ is considered to be a series of planes of point scatterers. Essentially, the wave above and below the plane of scatterers (atoms) are related by the phase grating;

$$\varphi(x, y, z+d/2) = \varphi(x, y, z-d/2) \exp(i\sigma \int_{z-d/2}^{z+d/2} V(\mathbf{r}) dz) \quad (2.41)$$

After scattering, the electron wave propagates through the 'vacuum' until the next plane of scatterers is reached also at a distance d , i.e. we can apply the Fresnel propagator

$$\begin{aligned} \varphi(x,y,z+d/2) = & \iint \exp\left(-ik\frac{(x-x')^2 + (y-y')^2}{2d}\right) \\ & \times \varphi(x',y',z-d/2) \exp\left(i\sigma \int_{z-d/2}^{z+d/2} V(r) dz\right) dx'dy' \end{aligned} \quad (2.42)$$

This process is repeated through the whole thickness of the crystal and, provided that the slice thickness d is small enough (2\AA), is a method of integrating Schroedinger's equation. In practice it is advantageous to write eqn. 2.42, a convolution in the xy plane, in terms of Fourier transforms, hence

$$\varphi(x,y,z+d/2) = \text{FT}^{-1}\left\{\exp(-i\pi d u^2) [\text{FT} \exp(i\sigma \int_{z-d/2}^{z+d/2} V(r) dz) \varphi(x,y,z-d/2)]\right\} \quad (2.43)$$

This is the method by which the exit wavefunction is determined. In practice, this slice sequence is repeated until the desired thickness is calculated, the wavefunction is then outputted from the calculation. The multislice technique is extremely versatile as the array of point scatterers does not have to be periodic, thus crystal defects such as stacking faults and grain boundaries can be easily modeled, one need only input the proper atomic positions.

§2.5 Microscopy Techniques

In this section the microscopy techniques that were used throughout this research are elaborated. The major technique of structural characterization was high resolution electron microscopy, specifically surface-profile imaging. The other techniques included bright-field/dark-field, nanodiffraction, and electron spectroscopies.

§2.5.1 High Resolution Imaging

It is well established that detailed structural information can be obtained from crystalline specimens by means of HREM. The microscope acts as a finely tunable filter of spatial frequencies that, in real space, provides a map of the atomic potential of the diffracting species. This atomic potential map can be achieved by using optimal diffraction conditions. That is, with the crystal oriented along a zone axis, the microscope well aligned and localized imaging conditions (Marks 1985a), a one-to-one mapping of the structure results where, in the most general case, 'black dots' correspond to atomic columns and 'white dots' to the channels in between them. Typically, high resolution images are obtained from crystals no thicker than 40 nm making the technique ideal for investigating UFPs. While plan view imaging where a thin section of the crystal is viewed through the top and bottom surfaces is well established, a relatively recent development is the surface-profile imaging (SPI) technique (Marks and Smith 1983). In SPI those crystal surfaces lying parallel with the electron beam are imaged, hence the profile surface. SPI is useful to examine structures such as reconstructions, relaxations, surface steps, etc. In the case of UFPs, the entire crystal is essentially all surface and thus both plan view and SP images are obtained from the same particle (see Figure 2.5).

In high resolution microscopy, the image is essentially an interference pattern resulting from the complex interaction of the electron beams with the specimen, each other and the microscope system. The imaging conditions, being dependent upon these many variables, must be carefully controlled if meaningful information is to be obtained from the image. As indicated from contrast transfer theory, periodicities in the image may arise from both structural and electron-optical artefacts; thus 'seeing is not always believing.' An important component in the analysis of high resolution images is the ability to calculate an image as a function of the imaging conditions. For example, a proposed structure

model may reproduce the image contrast at a particular imaging condition (say lens defocus) but give inaccurate results for another. Typically one takes a high resolution focal series of the specimen in steps of 5-10 nm (underfocus) in order to determine the validity of a structure model where the 'goodness-of-fit' is evaluated by matching at least

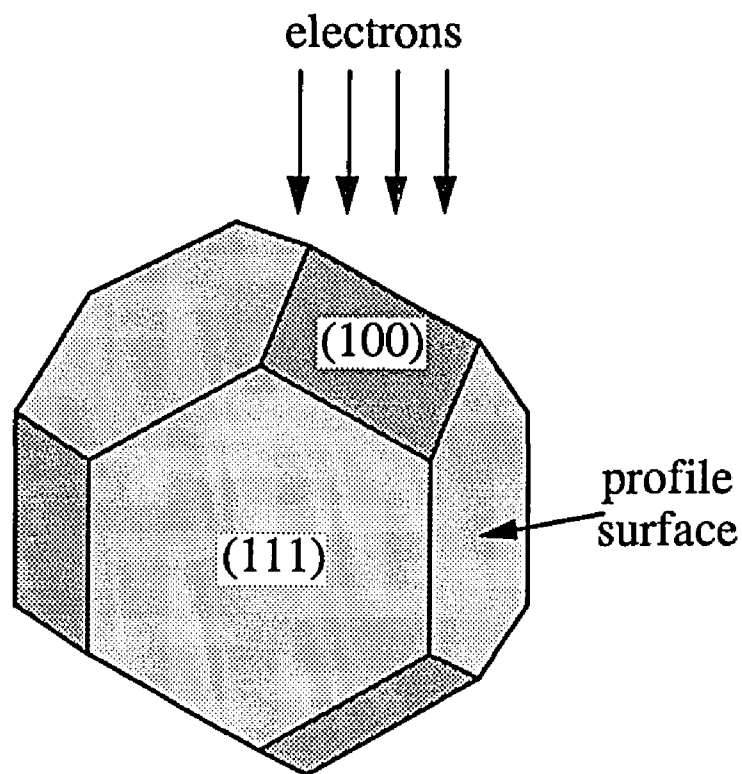


Figure 2.5. The orientation of the specimen for high resolution imaging. A small particle of alumina, comprised of $\{111\}$ and $\{100\}$ facets, is viewed along the $[110]$ zone. The particle has both profile and plan view surfaces available for investigation. For example, the indicated (100) facet is a plan-view surface while the (111) facet is a profile surface.

three of the calculated/experimental images in the focal series. For ultrafine alumina particles, where the crystal tilt exactly along a zone axis is difficult to obtain, the image can be calculated with a small amount of crystal tilt to validate the structure model. As it turns out, due to the complicated atomic arrangement in the spinel structure, crystal tilt of only 1 milliradian can substantially change the contrast in the high resolution image (see Chapter Four for more details on image matching).

§2.5.2 Bright-field / Dark-field Imaging

In HREM typically no objective aperture is used, and all diffracted beams are combined to form the structure image. However, if one uses an aperture then the image is formed by the resulting 'diffraction contrast.' In modern electron microscopes, it is very simple to switch between the different modes of operation; for example the H9000 has a CPU memory to store the lens and deflection settings for one BF and three DF channels all accessed by push-button control. In BF/DF, a small objective aperture is placed around the transmitted beam excluding all diffracted beams; this creates the BF image. Then, in DF mode, one of the diffracted beams is tilted by a double deflector system so that it lies along the optic axis; i.e. the diffracted beam in DF is now where the transmitted beam is in BF. This is called high resolution DF imaging as the diffracted beam travels along the optic axis (to minimize the effect of spherical aberration).

There are two BF/DF scenarios; one may choose a strongly diffracted beam to perform the DF imaging, or one may use a weakly diffracted beam. In the case of the strongly diffracted beam, conventional BF/DF, only those regions of the crystal(s) oriented to give the desired diffraction contribute to the image obtained in DF. In addition, this technique is useful to study crystal defects such as dislocations, stacking faults, grain boundaries, etc. For the current situation where UFPs are investigated, conventional BF/DF allows one to examine the internal strains associated with the contact stresses due to

adhesion and sintering. With UFPs, where thickness rapidly changes with position, the proper technique to image strain fields is strong or medium intensity DF. As shown by Marks (1985b), the strain fields in UFPs are almost always inhomogeneous and are discerned in the image by intensity modulations along contours of constant intensity (or 'thickness' fringes). For the case where diffracted beams of low intensity are used, i.e. weak-beam DF, the strain fields may be still imaged. However the response is small and contrast stems mainly from the highly distorted regions near the core of dislocations. In addition, weak-beam DF can be used to determine the 3D shape of UFPs (Saito 1979; Heinemann et al. 1979; Yacaman et al. 1979). An important point made by Marks (1985b) is that with UFPs any source of stress, either through contact with a substrate, other particles, or contaminants, gives rise to the same type of strain contrast in the DF image and so distinguishing the source of stress is exceedingly difficult.

§2.5.3 Nano-diffraction

The HREM is typically designed with a weak condenser lens system such that plane waves illuminate the specimen with a small amount of beam convergence. A direct consequence of this design is that the probe forming capabilities of the microscope are limited. That is, the ability to obtain diffraction patterns from a small region of the specimen is limited by the probe size of the electron beam. For the UHV-H9000 the smallest obtainable probe, using CAUX, is approximately 50 nm in diameter. As a result, the microscope can obtain discrete diffraction patterns only from those particles with dimensions much greater than 50 nm. In a typical sample, the UFPs cluster together in an ensemble of 10-20 particles, thus with a large probe one obtains a polycrystalline, or textured, diffraction pattern. Additionally, an unfortunate side effect of using a small probe is that the intensity in normal imaging mode is very low, i.e. it is only effective to operate in diffraction mode.

One may obtain diffraction patterns by means of a microscope which has been designed with 'nano-probe' capability. The HF-2000 has a field-emission filament, an extremely coherent point source, that can form a 1 nm probe with high intensity. The microscope also has a resolution of ≈ 0.25 nm which is good enough to examine most specimens. Use of this high intensity, coherent source does impose some constraints on the specimen. For instance, radiation sensitive materials may suffer rapid structure changes under illumination and, in the extreme, holes may actually be 'drilled' into the specimen (see Appendix One: Electron beam - solid interactions).

§2.5.4 Electron Spectroscopies

The electrons passing through and diffracted by the specimen are used to form the resulting image. Most of these electrons (99%) have interacted with the specimen elastically, that is the electrons have changed their direction (i.e. diffraction), but not their energy. However the remaining 1% which also arrive to form the image have interacted with the specimen, either through electron-nuclear or electron-electron collisions, in such a way that they contain information about the chemical structure of the specimen. That is, inelastically scattered electrons (primary electrons) have lost a certain discrete amount of energy that can be related to the chemical identity / structure of the atom with which it has collided. In addition, the electronic excitations from these collisions may result in the emission of a variety of radiation (i.e. secondary emission), such as Auger electrons. Thus while electron microscopy provides structural information, electron spectroscopy provides a wealth of chemical information with high spatial resolution. This section will treat only those inelastic interactions resulting from electron-electron collisions (see Appendix One for details on electron-nuclear ballistic collisions).

§2.5.4.1 Energy Loss Spectroscopy

Those transmitted electrons which inelastically collide with the electrons in the specimen, losing an amount of energy in the range of E to $E + \Delta E$, are collected in the energy loss spectrometer situated below the camera chamber. The EEL spectra of number of electrons or counts, $N(E)$, versus E contains three important general features; the zero-loss peak, the plasmon peak and the inner-shell ionization edges. The zero-loss peak contains by far the largest number of electrons which, as mentioned above, do not transfer any energy to the specimen. This peak has a width related to the energy spread of the incident electrons; i.e. a LaB₆ filament is broader than field-emission one. In the low-loss region (0 to 50 eV) the energy peaks are associated with plasmons which are created as a result of the interactions between the incident and outer-shell electrons (or the free-electron gas). The plasmon energy, E_p , is

$$E_p = (\hbar/2\pi) \omega_p = (\hbar/2\pi) (ne^2/\epsilon_0 m_0)^{1/2} \quad (2.44)$$

where ω_p is the plasmon frequency and n the number of electrons per unit volume that contribute to inelastic scattering.

In addition to the plasmons, the loss spectra from each element contains a discrete set of energies (peaks) with which it can be identified, e.g. the inner-shell ionization edges. Furthermore, the structure and shape of these edges can be related to the chemical bonding state of the element. The edge structure results from both the electronic environment of the element and its structural coordination. Consider the difference in the spectra for aluminum in MgAl₂O₄ spinel occupying octahedral sites and in orthoclase on tetrahedral sites (Taftø and Zhu 1982), see Figure 2.6. Here, though the valence of aluminum remains the same, its structural coordination and electronic environment are dramatically different. For a more than thorough review of EELS, see Egerton (1986).

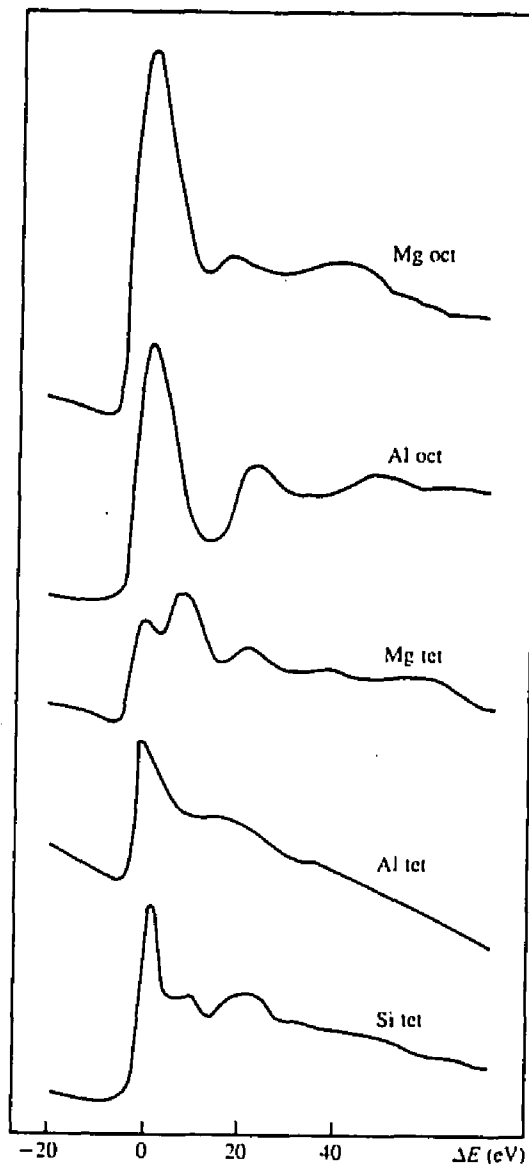


Figure 2.6. Electron-loss near-edge structure of Si, Al, and Mg atoms in different local crystallographic environments. The K edges of Mg in olivine (octahedral), Al in spinel (octahedral), Mg in spinel (tetrahedral), Al in orthoclase (tetrahedral), and silicon in olivine [from Taftø and Zhu 1982].

§2.5.4.2 Auger Spectroscopy

When a primary electron collides with an atom in the specimen, it imparts to the atom a certain amount of energy. If enough energy is transferred, this collision may result in an inner-shell (e.g. K) electron being 'knocked off', leaving the remaining ion in an excited state. The excited ion may then de-excite by having another valence electron from a higher energy shell (L_{II}) fall into the inner-shell hole, a process which leaves an excess energy of $E_K - E_{L_{II}}$ to be either released as X-rays (photon) or given to a third electron, for example the L_{III} . In the case of the latter process, the ejected electron has an energy of

$$E_A = E_K - E_{L_{II}} - E_{L_{III}} \quad (2.45)$$

and is known as a $KL_{II}L_{III}$ Auger transition. Auger electrons emitted with kinetic energy of 50-1500 eV have mean free paths of 0.3-1.5 nm in typical solids. These electrons escape from only the first few monolayers of the surface and, hence, provide chemical information with a high degree of surface sensitivity.

Typical surface science chambers equipped with Auger analyzers (CMA, HMA, or ESA) measure the surface composition over a large specimen area, i.e. 1 cm^2 . While a well prepared surface can be expected to have a reasonably uniform surface composition, usual experiment designs necessitate that the spectrometers collect Auger electrons from the entire surface and thus average out any inhomogeneities that may exist. Recent efforts have focused on avoiding this problem by placing the Auger spectrometer directly in the electron microscope. The advantage of this approach is that the Auger electrons collected by and large result from interactions of the primary electrons with the specimen which is, by nature, a very localized region of the surface of interest. Concurrent with this advantage are the disadvantages of poor collection efficiency and having only one surface available for analysis. These limitations at present preclude the use of in-situ Auger

spectroscopy for all but qualitative composition analysis. For the scope of this work, the spectrometer must reside in the microscope as an averaged collection includes Auger electrons from not only the UFPs but the SiO support film and the copper in the grid and cartridge. (Author's note: at the time of this writing the Auger spectrometer residing in the UHV-HREM was not optimized and, unfortunately, could not be used to obtain spectra from the UFPs. Future work would certainly need Auger studies to examine the surface chemistry, for example the segregation of dopants. In fact, a well-designed system would take advantage of computer controls to combine the Auger and EEL spectrometers to obtain both bulk and surface chemistry simultaneously.)

Chapter Three. Experimental Methods and Apparatus

This chapter details all of the experimental equipment and procedures which had to be developed in order to make the sintering of UFPs a success. The sintering project was split between two students; myself (JEB) and Mao-Hua Teng (MHT). With respect to equipment, my project goals were to design and perfect the ultra-high vacuum (UHV) systems. Teng's goals were to develop and refine the particle production and furnace systems. We were to then combine these into a functioning system. Thus all of the particle production and furnace characteristics given in this chapter were determined by Teng and will be noted as such. The remainder, including the vacuum systems and the microscopy component, were done by myself.

§3.1 Arc Discharge Method

The ultrafine alumina particles are produced by means of an arc discharge between two high purity aluminum electrodes. One of the usual methods used to create UFPs is the gas evaporation technique whereby the material of interest is heated in an (inert) atmosphere at low pressure. However, the arc method is necessary in light of the fact that aluminum, being non-thermionic (Guile 1984), does not 'smoke' in an oxidizing atmosphere as do tungsten and molybdenum. That is, when an aluminum wire is resistively heated at about 10 kPa of air a continuous smoke is not generated, instead the filament simply heats locally and then breaks. By using an arc discharge, the aluminum electrodes can be made to evaporate into an oxygen-rich atmosphere where coalescence into the ultrafine oxide particles occurs.

The electrodes consist of 99.999% aluminum in a 2 mm wire and $4 \times 4 \times 0.2$ cm plate configuration. The wire acts as the anode (+) and also the ground in the system whereas the plate is the cathode (-). This experimental configuration was determined to

give the best powder products (by MHT). An alumina retaining ring, measuring 1 cm in diameter and 0.5 cm high, confines the arc on the plate to provide more localized evaporation. The experimental arc conditions used to produce the alumina particles are as follows;

Table 3.1: Experimental Arc Characteristics
(with 750 Ω ballast resistor)

<u>Pressure</u>	<u>Voltage</u>	<u>Arc current</u>	<u>Electrode gap</u>	<u>Mean size</u>
6.5 kPa	1000 V	0.84 - 0.86 A	1 mm	15 nm
10 kPa	1000 V	0.84 - 0.86 A	1 mm	35 nm

The ballast resistor is added to the circuit to reduce the arc current as large currents induce such intense arcing that the electrodes melt in a very short time.

The arc has three distinct regions; the electrodes, the arc-associated plasma, and the smoke plume, see Figure 3.1. The intense arc creates a plasma between the electrodes resulting in local melting. The arcing plasma is confined on the plate by the retaining ring. The elevated temperatures near the arc create convection currents which carry the metal vapor up into the oxidizing gas where the condensation forms the smoke plume. As noted in Table 3.1 given a constant electrode configuration, raising the pressure results in a larger average particle size, see Figure 3.2. These results follow from the earlier work of Uyeda et al. (1963, 1972, 1973, 1976, 1977, 1990) and Tholen (1979, 1981, 1982) on gas evaporation systems. Essentially, the arc produces localized melting of the electrodes and the gas molecules provide a large undercooling allowing many small nuclei to form. These nuclei grow by coalescence into stable particles whose size is proportional to the gas pressure; this functionality is attributed to slower convection currents at higher pressures allowing the particles to stay at their growth temperature for longer periods. In addition, the use of a higher molecular weight gas results in slower convection currents and hence larger particles.

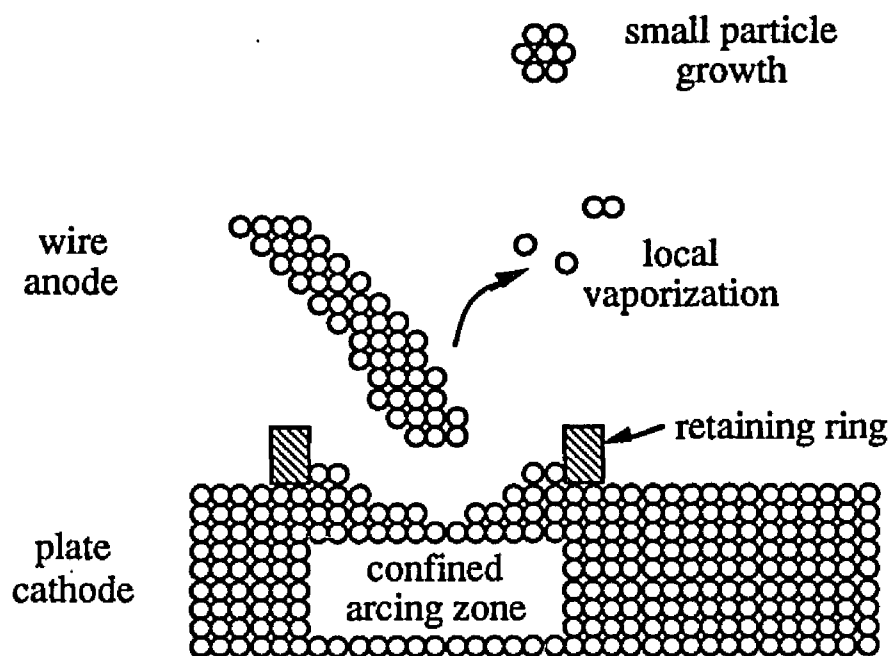


Figure 3.1. Schematic representation of the arcing process. The electrodes locally melt during arcing to form the ultrafine particles. The arcing is confined by the retaining ring.

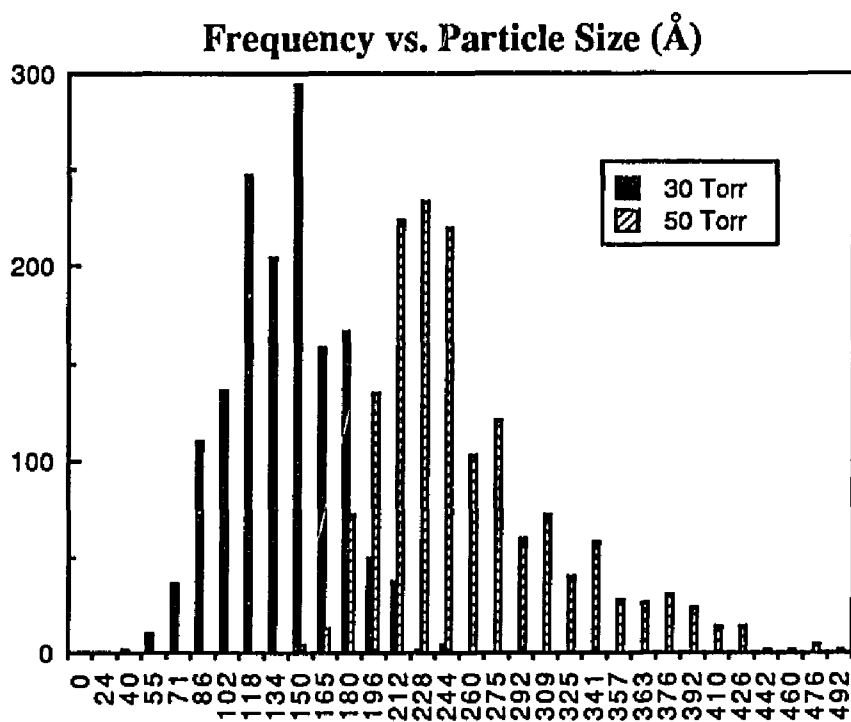


Figure 3.2. The particle size distribution as a function of arcing pressure.

§3.2 Experimental Equipment

In order to study the sintering behavior of the ultrafine ceramic particles, three objectives must be met. Firstly, the particles must be produced and collected for microscopic observation. Secondly, the particles must be sintered in a well characterized furnace. And finally, the whole process, including the structural characterization in the microscope, must be conducted in a clean environment that minimizes the probability of surface contamination and reactions.

To achieve these objectives, a whole host of equipment had to be constructed, each one custom-made to perform its particular function. The UHV furnace system was designed and constructed to produce, sinter, and collect the UFPs and also to function under near-UHV conditions. The UHV-HREM was conceived as a surface science instrument and, even though the sintering project does not require all of its capabilities, was substantially modified to provide this degree of sophistication. The following sections outline the design considerations and capabilities of both the UHV furnace and the UHV-HREM systems to provide an overall view of the complexity required to investigate the sintering behavior in UFPs.

§3.2.1 The UHV Furnace System

The flowing gas furnace serves a dual purpose. On the one hand, the furnace tube must be narrow enough to adequately collimate the flow of the UFPs. And on the other, the furnace tube can not be so small as to preclude the attainment of UHV. The resulting design of the furnace represents a balance between these conflicting goals that enables the furnace to achieve both near-UHV and effective particle collection. In what follows the design details of the furnace are elaborated, in addition to the performance characteristics of the furnace/vacuum system as a whole which is shown in Figures 3.3 and 3.4.

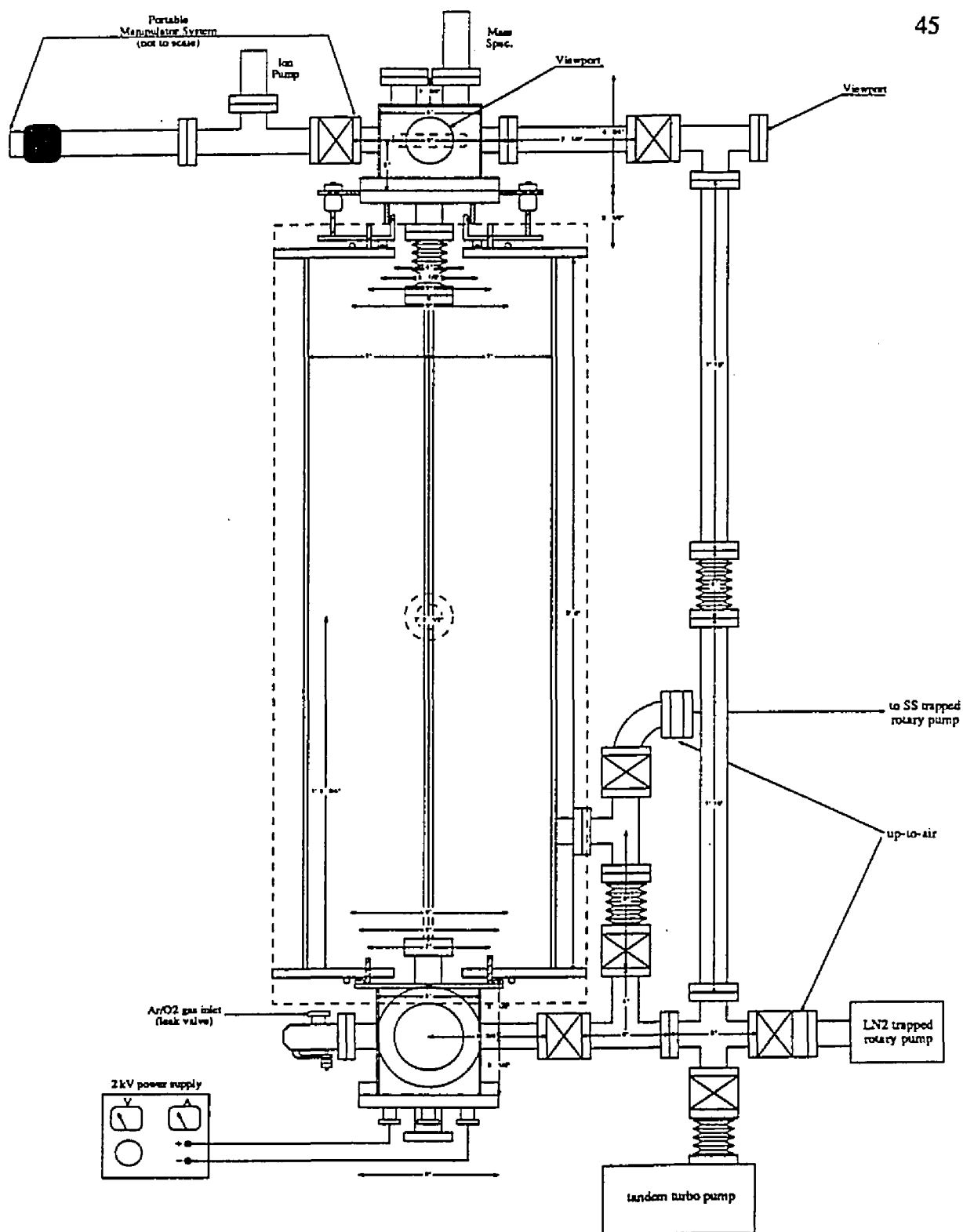


Figure 3.3. Schematic of the entire UHV furnace system. The large furnace tube vacuum chamber supports the whole structure and rests upon an angle iron frame (not shown).

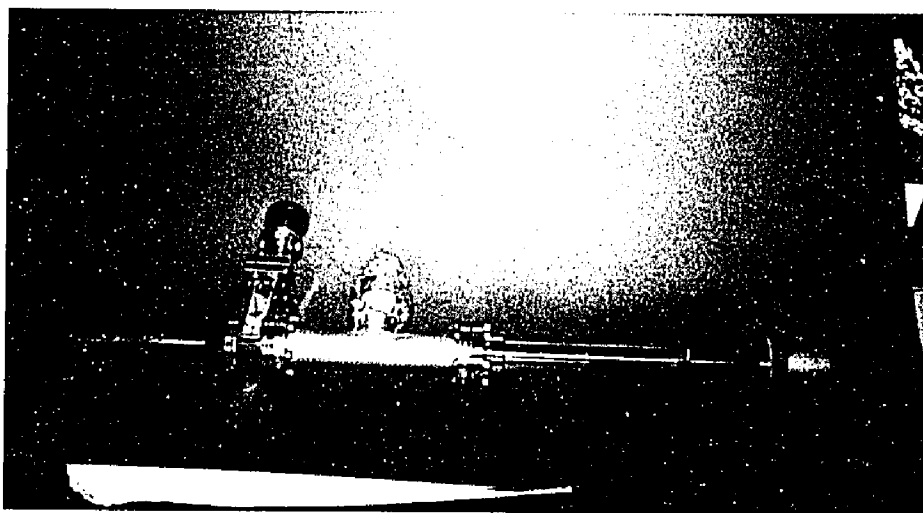
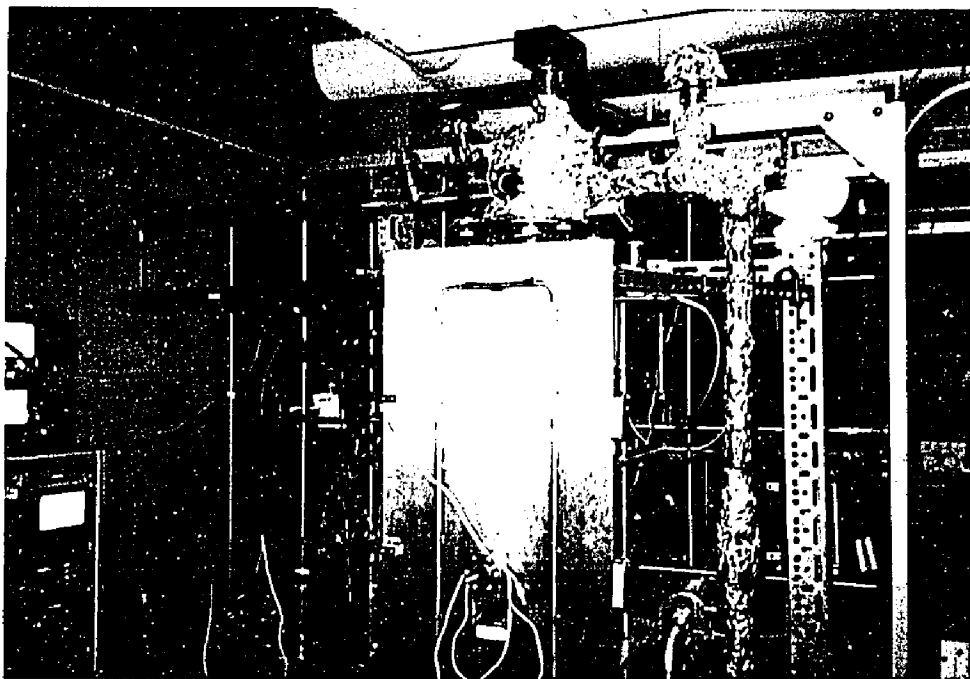


Figure 3.4. The UHV furnace system showing the transfer rod and collection chambers (a) and the specimen transfer chamber with the cartridge exposed (b).

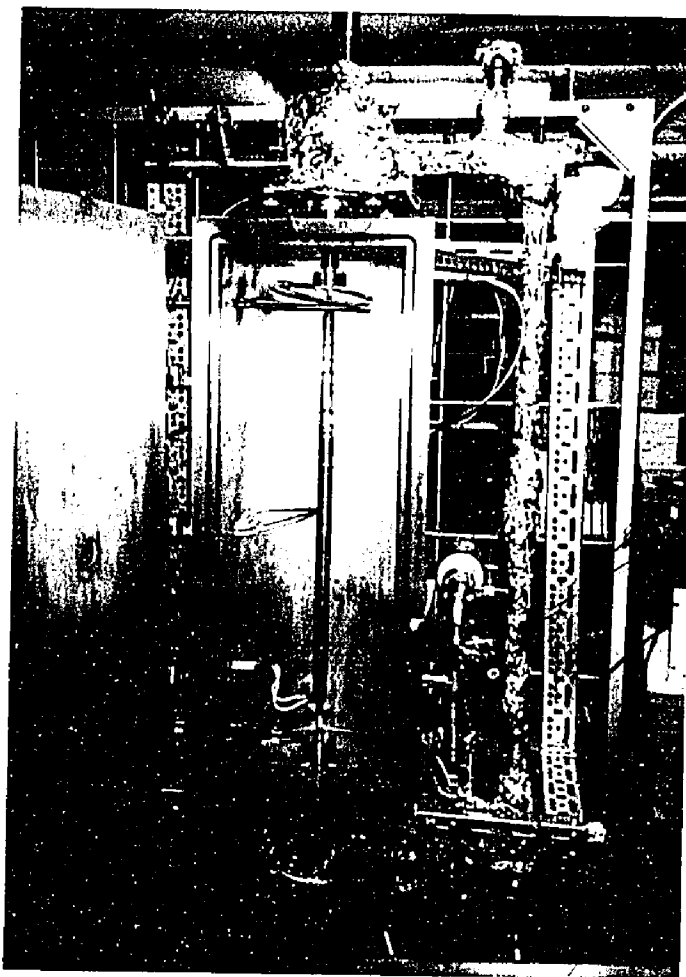


Figure 3.4 (c). The UHV furnace tube and vacuum chamber. The large furnace tube vacuum chamber has been opened revealing the tube with the flexible UHV bellows and water lines at top. The thermocouple connections are in the middle. The power feedthrough and water lines at the bottom. The furnace tube is wrapped in Mo foil which has blackened due to the burnout of binder materials in the furnace tube cement.

The furnace tube used in the present system consists of an extruded tube of 99.998% alumina (McDanel Corp.) with inner and outer diameters of 0.5 and 1.1 cm, respectively. The overall length of the tube measures 100 cm and brazed on the ends are stainless steel sleeves. Welded to these sleeves are UHV knife-edge flanges. The Kovar braze material (Ceramaseal) must be kept below $\approx 700^{\circ}\text{C}$ to maintain vacuum integrity and so the flanges are water-cooled and the extent of the heat zone terminates 10 cm from the braze junctions. The furnace heat zone is a non-inductive winding of 0.1 cm Mo wire along the central 80 cm of the tube. The Mo wire is encased in alumina cement and four type R (Pt/Pt-13%Rh) thermocouples are attached at 15 cm intervals. The furnace tube is surrounded by three concentric radiative heat shields made of Mo foil.

Originally, the furnace was designed to have a hole in the Mo heat shields and the alumina cement to enable the temperature at the center of the tube to be measured by an optical pyrometer aimed through a sapphire viewport. However, the heat losses through the opening in the cement and foil were large enough to seriously distort the temperature profile along the furnace and the pyrometer option had to be discarded. The convective heat loss through the heat shields is minimized by lowering the gas pressure in the furnace chamber. In addition, there remains a central hole in the heat shields for the four thermocouples resulting in some heat loss and a small dip in the temperature profile, see Figure 3.5.

The furnace tube is surrounded by a large vacuum chamber that has flanges for feedthroughs. These ports include an electrical feedthrough for the Mo heat winding, two water feedthroughs to cool the top and bottom flanges, an eight pin feedthrough made of extension wire for the thermocouples, a forming gas ($\text{N}_2\text{-}5\%\text{H}_2$) inlet valve, a pumping port, and sapphire viewport in the door intended for the optical pyrometer. This vacuum chamber, designed by MHT and constructed for Northwestern University by Ability Engineering (S. Holland, IL), also has 10 cm holes in the center of the top and bottom

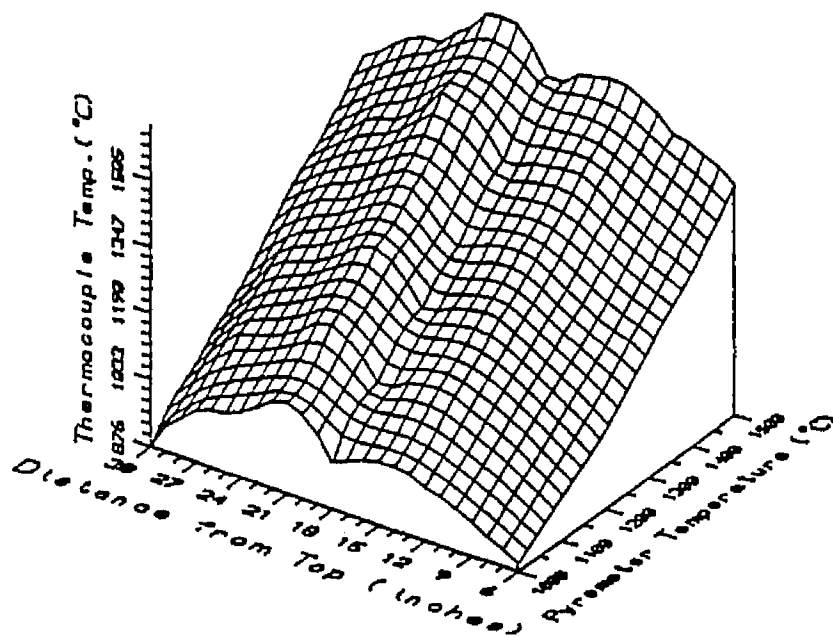


Figure 3.5. The measured temperature profile of the furnace tube (courtesy of MHT).

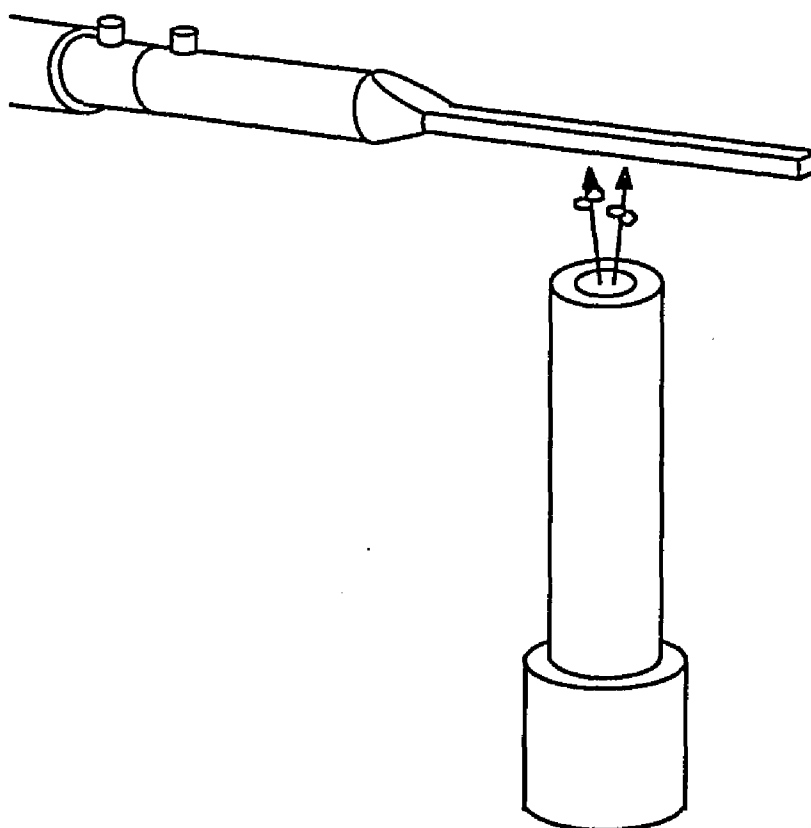


Figure 3.6. The extender tube transports the ultrafine particles through the bellows to the specimen cartridge.

plates for the attachment of the particle production and collection chambers. The chamber is sealed by means of O-rings for the door and the top and bottom chambers; the feedthrough ports have knife-edge seals. The chamber is pumped down simultaneously with the UHV chambers to minimize any pressure differential across the furnace bellows. However, the chamber is only connected to a rotary pump and is maintained at about 1 Pa at all times with the exception of particle production when the pressure is increased, in conjunction with the production chamber, to about 5 kPa.

The furnace tube is connected to the particle production and collection chambers in order to achieve UHV conditions and to isolate the furnace and UHV chambers during particle production. This isolation is necessary because when the furnace is in operation, the Mo windings and heat shields must be kept in a reducing atmosphere, i.e. the N_2 -5% H_2 forming gas. However, the UFPs of interest are created in an oxidizing atmosphere of Ar-20% O_2 . The incompatibility of these two requirements demands isolation seals of the highest integrity, for if these seals should fail the result is an uncontrollable fire and possible explosions. For further information see Appendix Three: What Not To Do.

In the current design configuration the furnace tube is rigidly connected to the flange of the particle production chamber which protrudes through the 10 cm hole in the bottom plate of the furnace chamber. The connection of the Mo winding leads and the lower cooling lines are also made at the bottom of the furnace chamber. This allows the top of the furnace tube to be 'free-floating' in order to accommodate the thermal expansion of the tube and also to minimize any bending moments upon the tube that would result in the breaking of the seals or the tube itself. It should be noted, however, that the thermocouples are physically attached at the center of the tube and that the top flange has cooling lines connected to it. The obstacles these connections pose to the free motion of the tube are circumvented by providing slack in the case of the thermocouples and using a

wide radius cooling line, made of light-weight flexible tubing, that encircles the top flange.

The connection between the particle collection chamber and the furnace tube is accomplished by means of a flexible bellows which, in addition to minimizing any bending moments on the tube, allows the tube to expand and contract freely during a temperature cycle (the tube expands by ≈ 2 cm at 1500°C). The collection chamber is attached to a specimen stage that, by means of sliding O-rings, allows for three degrees of freedom. That is, the particle collection chamber and flexible bellows can be aligned as perfectly as possible with the furnace tube so that the combination functions cooperatively. As a result of this system, however, there exists a gap of 22 cm between the exit hole of the furnace and the microscope specimen cartridge where the particles are to be collected. To minimize any spread of the particle stream and also avoid the high surface area of the bellows, a tube extender is placed in the gap. The extender, constructed from the same material as the furnace with a wide base to provide stability, rests upon the top flange of the furnace tube and terminates a short distance below the height of the specimen cartridge. The extender is allowed to rise and fall in conjunction with the furnace tube, however it does not reach the high temperatures that exist within the furnace. The distance between the exit of the extender and the specimen cartridge therefore varies as a function of the furnace temperature; at 1000°C the distance is 1 cm and 6-7 mm at 1200°C . The short distance ensures that nearly all of the particles produced are collected with very minimal losses to the chamber walls, see Figure 3.6.

The UFP production chamber is designed so that the entire electrode configuration is confined to a single flange. The flange contains the electrical feedthroughs, a high pressure (Granville-Phillips convectron) gauge, and a rotary feedthrough for the manipulation of the wire electrode. The advantage of this system is that the electrode configuration is fixed and new material can be supplied while only one UHV seal need be

replaced, see Figure 3.7. The remainder of the production chamber consists of a leak valve inlet for the gas mixture and an ionization gauge. The ionization gauge can be isolated from the production chamber by a butterfly valve; this eliminates the arcing problems caused when the UFP chains fill the chamber before rising to the furnace.

As the particles exit the tube extender they are collected upon a microscope grid (holey film on a copper mesh) that is held in a microscope cartridge. The cartridge is manipulated by a rotary/linear magnetically-coupled feedthrough that has cerium-based magnets to allow for the exact positioning of the cartridge directly in the UFP/oxidizing gas stream. The positioning of the cartridge is facilitated by two viewports in the collection region to ensure exact alignment; the importance of this feature is that the microscope grid presents only a 1 mm cross-section to the particle stream and the particles of interest are those which travel along the central axis of the furnace tube. If a wider cross-section is desired, however, the specimen holder can be replaced with one designed (by JEB) for 3 mm holey grids.

The specimen cartridge, connected to the rotary/linear feedthrough, can be retracted fully from the collection chamber. Once retracted into the portable transfer system (PTS), the specimen can be isolated from the rest of the vacuum system by a gate valve. If so desired, the isolated region can be pumped by a small battery-powered 1 ℓ /sec ion pump. The PTS concept is that once the specimen has been collected, it can be transferred to the UHV-H9000 microscope under high vacuum. A pressure of 10^{-6} Pa is attainable within an hour after collection; UHV can be achieved by baking the entire system. The PTS ensures that the specimen does not 'see' contamination from the atmosphere or residual gases during transfer to the UHV microscope. Minimization of contamination is very important to the study of the virgin surfaces of the alumina UFPs which act catalytically in the

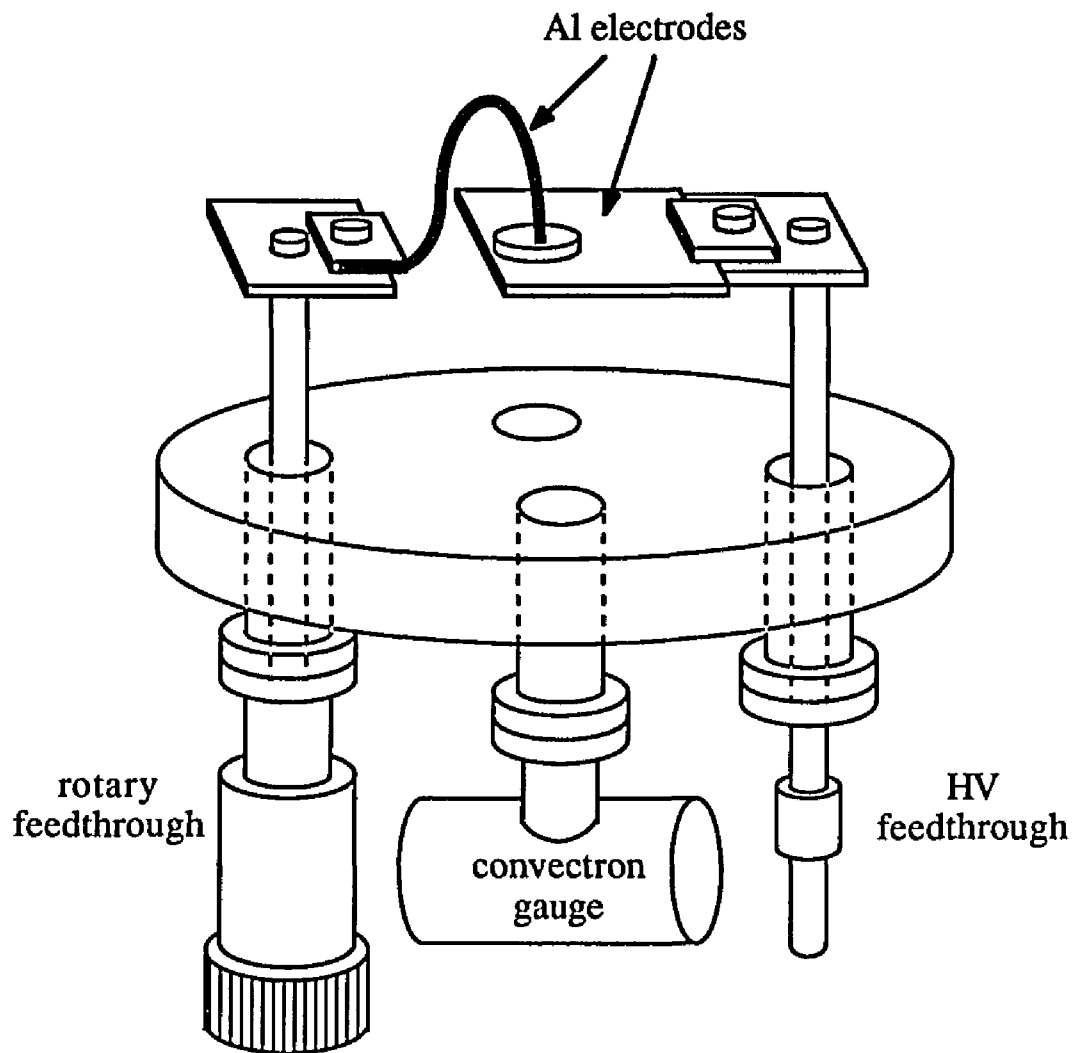


Figure 3.7. The arcing apparatus is designed to occupy only one 8 inch flange. Thus when the electrode materials are replaced, only one UHV seal need be changed. The alignment of the electrodes is done at atmosphere.

atmosphere, i.e. they act as a 'getter' for oils and other hydrocarbons, etc. Of course, control of the purity of the Ar/O₂ gas is very important since the alumina UFPs 'see' these gases from their inception. At present, the arcing gases are delivered to the system at a pressure of 5 psig and are blended by flow meters individually calibrated for their respective gases. Then the mixture is fed into a Varian leak valve that is equipped with a particulate filter.

§3.2.2 UHV Furnace Conductance Analysis

It is appropriate whenever designing a vacuum system to analyze its conductance properties to determine the ultimate obtainable pressure of the chamber. Consider Figure 3.8 showing a schematic layout the UHV furnace system. The total surface area of the vacuum system was calculated to be approximately 6300 cm²; each chamber and connecting tubing is labeled separately. The conductances for the tubing can be calculated by the standard equation for molecular flow (pressures below 0.1 Pa);

$$C_p = 11.6 \frac{D^3}{L} \quad \ell/\text{sec} \quad (3.1)$$

where D and L are the tubing diameter and length (in cm). The conductance of a given tube limits the nominal pump speed by the following equation;

$$\frac{1}{S_{\text{eff}}} = \frac{1}{S} + \frac{1}{C_p} \quad \text{sec}/\ell \quad (3.2)$$

where S and S_{eff} are the nominal and effective pumping speeds. From eqn. 3.1 it is obvious that the furnace tube is conductance limited having a maximum conductance of ≈0.012 ℓ/sec. To summarize the rest of Figure 3.8, the electrode chamber tubing has a conductance of 15.5 ℓ/sec and the side tubing of 4 ℓ/sec. Factoring in the 80 ℓ/sec speed of the turbo-molecular pump results in the electrode chamber pumping at an S_{eff} of 12 ℓ/sec and the specimen chamber pumping at 3.7 ℓ/sec.

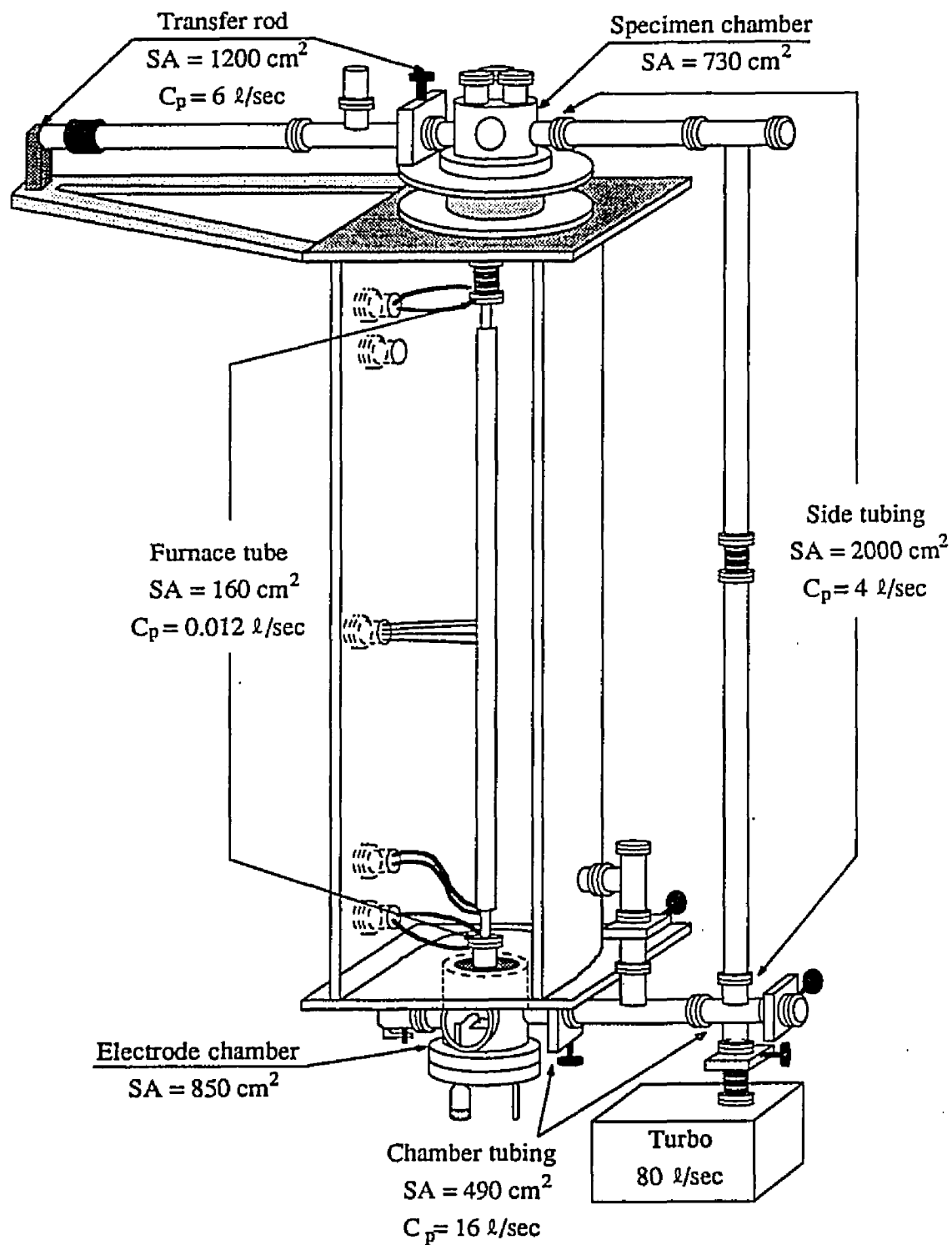


Figure 3.8. Perspective view of the UHV furnace system. The conductances are broken down into the labeled components.

The above analysis treated each chamber as a separate entity, however the turbo pump must simultaneously evacuate both chambers. To treat the furnace system as a whole the conductances must be combined. Given the law of conductances and assuming that the furnace tube effectively isolates each vacuum chamber, then total conductance is;

$$C_T = \left(\frac{1}{50} + \frac{1}{16 + 4} \right)^{-1} \quad \ell/\text{sec} \quad (3.3)$$

or a C_T of 14 ℓ/sec . Combining with eqn. 3.2 results in an S_{eff} of 12 ℓ/sec . This value represents the tradeoff between adequate conductance and overall expense. For example, the conductance could have been increased by use of larger diameter tubing, however then the total cost of the furnace system would have been prohibitively high.

It should be noted at this point that the dimensions of the furnace tube were dictated by the need to maintain a proper gas flow during the sintering process. The obvious drawback to this design strategy is that the furnace tube could not *ever* be adequately pumped to UHV regardless of how large a pump is used. Such a result stems from the considering the total outgassing rate of the vacuum chamber walls. For example, the ultimate pressure of a vacuum system, P_u , is determined by the ratio of the total outgassing rate, Q , to the effective pumping speed, S_{eff} :

$$P_u = \frac{Q}{S_{\text{eff}}} \quad \text{Pa} \quad (3.4)$$

where typical values of Q for 'clean' stainless steel are $\approx 10^{-8} \ell \cdot \text{Pa}/\text{sec}$. Considering that the furnace tube pumps at an S_{eff} of 0.012 ℓ/sec , the ultimate pressure attainable is 8×10^{-7} Pa. Baking the furnace tube at high temperatures of 1200°C can improve the situation, however, the porous nature of alumina surfaces will limit the overall Q improvement.

Another mitigating factor in the conductance analysis of the furnace chamber is the total surface area to be pumped. The standard rule-of-thumb in UHV is that for every 100 cm^2 of steel surface area, one needs to supply at least 1 ℓ/sec of effective pumping speed.

The analysis of the furnace tube and UHV chambers reveals that a total of 6300 cm^2 , including the transfer mechanism, needs to be pumped at an S_{eff} of 63 l/sec ; however, the conductance limitations imposed by the design constraints only provides for $\approx 4 \text{ l/sec}$. In addition, the turbo-molecular pump, even though it has a pumping speed of 80 l/sec , also has a base pressure of $2 \times 10^{-7} \text{ Pa}$ below which the pump begins to back-stream. When one considers these limiting factors on the vacuum performance of the furnace system, it is not surprising that the best vacuum attained in the electrode chamber has been $\approx 5 \times 10^{-7} \text{ Pa}$.

§3.2.3 *The Furnace Vacuum System*

As mentioned above, the furnace chamber is pumped by a 3.3 l/sec rotary pump and can be isolated from the UHV system by a gate valve. To minimize any pressure differential between the furnace chamber and the UHV system, the chambers are initially pumped down simultaneously by the trapped rotary pump. In the presence of a pressure difference, the welded bellows above the furnace would either expand or contract stressing the fragile alumina tube, or Kovar seals, resulting in mechanical failure. Once the chambers have achieved pressures lower than 10 Pa , the chambers are isolated by the furnace gate valve and the 80 l/sec turbomolecular pump (which is isolated from the vacuum system by a gate valve) brings the UHV system to its ultimate vacuum while the rotary pump maintains the furnace chamber at 1 Pa . The turbo pump is located at the bottom of the vacuum system and thus the specimen collection chamber, located at the top, is not effectively pumped. To alleviate this problem a 20 l/sec triode ion pump is attached to the specimen chamber and can also be isolated from the chamber by a gate valve.

Even with both the turbo and ion pumps the furnace tube remains conductance limited in its pumping speed. This is not a major problem though because during the bakeout of the system, the furnace tube must reach temperatures around 1400°C . That is, the furnace must be run hotter during a bake than during particle production to ensure its

cleanliness. The resulting temperature gradient between the furnace tube and the adjoining chambers (baking at $\approx 150^{\circ}\text{C}$) is large enough to drive impurities, such as water vapor and hydrocarbons, out of the furnace tube. Once in the larger chambers, the impurities can be effectively pumped away. The result is that once UHV has been attained, the furnace tube can reach 1000°C before there is a large pressure rise (outgassing) in the vacuum chambers. Actually, as the furnace is heated up there is a pressure burst at 200°C , but then the total pressure in the system decreases as the furnace temperature continues to climb until 1000°C is reached; i.e. the pressure rises from 5×10^{-7} Pa to 2×10^{-6} Pa at 1000°C .

§3.2.4 Particle Production Procedure

The method of producing the alumina UFPs, as mentioned before, is an arc discharge between two high purity aluminum electrodes in an oxidizing atmosphere. The following procedure is currently used to produce the UFPs; first we attain UHV in the vacuum system and then, in UHV, the furnace is heated to the desired temperature slowly over approximately 2-3 hours. During the heating process the vacuum level and gas species are monitored to ensure the cleanliness of the system. Once the furnace has stabilized both the furnace chamber and the UHV chambers are backfilled, isolated but in conjunction, with forming and oxidizing gases, respectively. The introduction of these gases cools the furnace temperature and the power to the furnace is increased to maintain the proper setting. Once the required pressure is attained, about 6 kPa, the oxidizing gas is forced to flow up the furnace tube at the desired flow rate and exits the system through a liquid nitrogen-trapped (LN₂) rotary pump. After both the furnace temperature and the gas flow have reached steady state, the arc discharge can be started and the specimen cartridge brought into the rising gas/particle stream for collection.

The arc is typically run for about 3-4 minutes after which the specimen is retracted into the PTS, the length of collection being governed by the number of smoke bursts in the

arcing process to give a good particle density on the grid. The furnace and UHV chambers are then rough pumped simultaneously down to about 10 Pa, all the while maintaining pressure equilibrium across the welded bellows and isolation between the furnace and UHV chambers. At this vacuum level the LN₂-trapped rotary pump is isolated and the turbo and ion pumps take over to bring the UHV chambers into the 5×10^{-6} Pa range within a hour. A full bake of the system will give UHV; however this process takes about twelve hours and may not be as crucial to the cleanliness of the particle surfaces. What is important, however, is that the UFPs avoid contamination from rotary pump oil and the atmosphere. During this pumpdown interval, the furnace tube is cooled down to room temperature after which the PTS is isolated by its gate valve and the furnace/UHV systems are brought up to air. The PTS can then be detached from the collection chamber and, under vacuum, transferred to the UHV-H9000 microscope by means of the custom-made grabber mechanism on the specimen transfer chamber (STC) described below.

§3.3 UHV High Resolution Electron Microscopy

§3.3.1 The History of UHV Microscopy

The necessity of studying crystal surfaces under UHV conditions has long been recognized, though unobtainable with the technology of the time. Early efforts were made to improve the vacuum level (Moorhead and Poppa 1969; Braski 1970) in microscopes that included UHV-type components for thin film studies. However, few results were obtain with these systems (for example, Poppa et al. 1971, 1974; Poppa and Moorhead 1981). A JEOL100B was successfully modified (Honjo et al. 1977; Takayanagi et al. 1978) to include features such as a titanium sublimation pump (TSP) and an evaporation source to observe in-situ thin film growth in the microscope (Mori et al. 1980). A drawback to the design was the need to have a liquid helium-cooled cold finger to improve the local vacuum

about the specimen. While a cold finger does indeed accomplish this goal (as evidenced by the predominance of the feature in CTEMs), they are bulky and inconvenient to work with and usually improve the vacuum at the expense of resolution loss due to vibration (bubbling). In addition, one can only infer the local vacuum state at the specimen with a cold finger, observing the oxidation rate of Fe for example (Takayanagi et al. 1978), and this introduces some uncertainty; for instance, in a stainless steel UHV chamber oxygen levels are generally at least an order of magnitude smaller than the H₂, H₂O, and CO levels. A number of other UHV microscope systems exist presently each including features that enable the user to perform certain surface science experiments (see Table 3.2 and Figure 3.9). Heinemann and Poppa (1986) circumvented the problem of non-UHV conditions in the microscope column by including a small specimen chamber within the objective lens region. This chamber can easily be pumped down to UHV ($\approx 4 \times 10^{-8}$ Pa) while the rest of the microscope remains at high vacuum. Inside the chamber, evaporation sources allow the user to study thin film growth and desired gases can be leaked into the chamber for catalysis experiments (Avalos-Borja et al. 1988). McDonald and Gibson (1984) replaced the objective lens region of a JEOL200CX with UHV components to achieve a vacuum level of 10^{-7} Pa. An inherent flaw with these microscope designs is that in order to change specimens, the microscope must be dismantled and the specimens exposed to the contaminating atmosphere. This disadvantage requires that all characterization instrumentation must be resident in a microscope that is limited by space considerations. Ohi et al. (1987) and Kondo et al. (1987) have developed the JEM-2000FXV to alleviate the space problem in UHV-HREM by including six attachment ports for instrumentation. Their design, unfortunately, also necessitates the use of cryopumping to maintain UHV and does not provide for UHV specimen transfer. Metois et al. (1989) converted a JEOL100C into a UHV microscope with TEM, STEM, REM, and SEM capabilities for crystal growth

Table 3.2: UHV microscopes and their capabilities.

Microscope	Ultimate Vacuum & Resolution	Characterization & Preparation	Comments
Hitachi UHV-H9000 (Marks et al.)	8×10^{-9} Pa (bake) 1×10^{-8} Pa (in use) 0.2 nm PT-TO-PT	LEED, AES, PEELS, SIG, inDRH, X-ray, laser, evap, annealing, $\pm 10^\circ$ tilt	No Cryo, UHV transfer
JEM2000FXV (Yagi et al.)	1×10^{-7} Pa (?) 0.22 nm PT-TO-PT	6 attachment ports and large tilting	Cryo and no side chamber
Philips EM430 (Kruit et al.)	1×10^{-8} Pa 1.0 nm probe size	PEELS, AES, evap., X-ray, MBE, PIMS, $\pm 15^\circ$ tilt	No Cryo and prep. chamber
Philips 430ST (Smith et al.)	1×10^{-7} Pa 0.2 nm PT-TO-PT	evap, SIG, heating stage, PIMS, $\pm 15^\circ$ tilt	Cryo and prep. chamber
JEOL200CX (Gibson et al.)	1×10^{-7} Pa 0.25 nm PT-TO-PT	MBE, DRH, heating and cryogenic stage	Cryo and side chamber
JEOL100B (Honjo et al.)	2×10^{-7} Pa ≈ 0.35 nm (fringe)	EBE, evap., ports and large tilting	Cryo and no side chamber
Seimens/Elmiskop 101 (Poppa et al.)	4×10^{-8} Pa ≈ 1.5 nm PT-TO-PT	MBE, OPC, SIG, heat / cryo stage, gas jet cleaning, evap. environment cell	Cryo and no side chamber
VG/STEM HB501A - FEG (Silcox, Cornell)	3×10^{-8} Pa 0.27 nm probe (DF) 0.2 nm PT-TO-PT	windowless X-ray, AES, EELS, evap., SIG, SED, heating, Si-intensifier	prep. & transfer chambers, double viton seal
VG HB501 (Patterson, IBM)	1×10^{-7} Pa ≈ 0.3 nm PT-TO-PT	ultra-thin window X-ray, PEELS, SIG, heating	prep. chamber
JEOL100C (Metois et al.)	8×10^{-7} Pa ≈ 0.7 nm PT-TO-PT	evap., heating stage, STEM, REM, SED	Cryo specimen air-lock

AES = Auger electron spectroscopy, Cryo = cryopumping needed, DRH = direct resistive heating, EBE = electron beam evaporator, evap = evaporation source, LEED = low energy electron diffraction, MBE = molecular beam epitaxy, OPC = oxygen plasma cleaning, PEELS = parallel electron energy loss spectroscopy, PIMS = precision ion mill system, SED = secondary electron detector, SIG = sputter ion gun.

Table 3.2. Summary of UHV microscopes. The equipment list may not be complete due to the continual improvement of the microscopes by the various research groups. VG/STEM information courtesy of Drs. J. Silcox and J. Patterson (private communications).

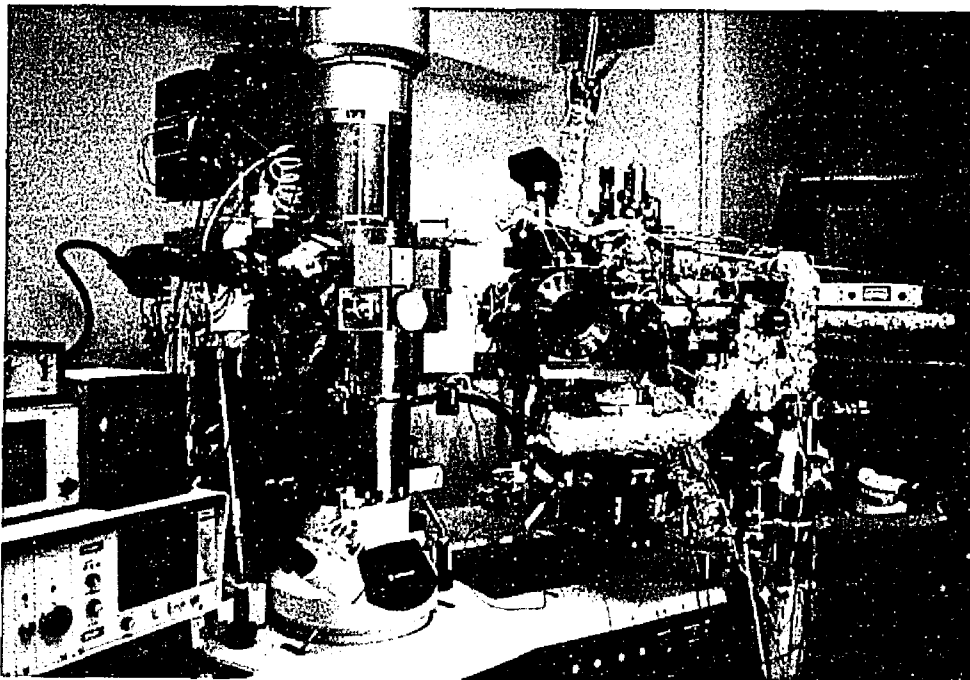


Figure 3.9(b). UHV-H9000 HREM in actual use. Here, the microscope is seen as a functioning system with the STC attached. The instrument cluster can be seen. Note: the aluminum foil that covers most of the STC is used as reflective heat shields for bakeout.

studies. As with previous efforts, the microscope requires extensive cryopumping to maintain UHV conditions and the presence of non-UHV seals such as viton allows contamination of specimens by molecular oxygen, etc. Smith et al. (1989) have modified the objective lens region of a Philips EM430 in an effort to obtain UHV. Though the pumping speed and cleanliness of their system is greatly improved, the use of O-rings precludes vacuum levels below 10^{-7} Pa for any sustained period of time. The problem of climbing vacuum levels can be circumvented by the use of a heating stage; for example a specimen at 200°C (low heating) can thermally desorb most contaminants.

The problems of Smith et al. have been circumvented by Kruit (1990) by redesigning the Philips EM430 STEM with all metal seals and the use of oil-free pumping systems. With the design no cryopumping is required to achieve UHV at the specimen. The microscope also has additional ports surrounding the specimen for the attachment of instruments such as MBE and X-ray spectrometers. In a significant advance over previous instruments, the objective lens pole pieces have been totally redesigned as a 'monopole' lens system (Bleeker and Kruit 1990a,b; Bleeker et al. 1991). This pole piece, coupled with a 90° deflector system, allows virtually all Auger electrons produced in the specimen to be collected and analyzed by a hemispheric electrostatic analyzer (ESA) attached to the side of the microscope column. When used in conjunction with PEELS, one is able to then measure both the energy lost by the primary electrons and the energy of the Auger electrons produced. These types of experiments are similar to those conducted with X-ray photoelectron spectroscopy (XPS), however with a 1 nm spatial resolution.

§3.3.2 The UHV-H9000 HREM

The UHV microscope represents the 'cutting-edge'/state-of-the-art technology melding the high spatial resolution capabilities of transmission electron microscopy (TEM) with the advantages of surface science techniques into one truly unique instrument. The

UHV-H9000, designed by Hitachi in collaboration with Drs. L.D. Marks and P.C. Stair of Northwestern University, is essentially the same microscope as its H9000-HREM predecessor in that the microscope microprocessor (CPU) and panel controls are the same, thus ease of operation is not precluded by the introduction of UHV technology in the microscope. But whereas the H9000 has a base pressure of $\approx 10^{-5}$ Pa, the UHV-H9000 has been completely redesigned to achieve an ultimate vacuum of $\approx 8 \times 10^{-9}$ Pa. The dramatic improvement in vacuum is accomplished by fully incorporating UHV technology and design philosophy. That is, techniques such as knife-edge seals (with OFHC copper gaskets) and clean, dry pumping systems are used with careful attention to the cleanliness of all components.

The region between the electron gun and viewing chamber is constructed from UHV-grade materials; for instance, the load bearing members of the column are made of 'non-magnetic' stainless steel and the segments are sealed by Helicoflex crushable O-rings. The objective lens/specimen region of the column is fully bakeable to 200°C and two quartz halogen bulbs are provided for internal baking. The halogen bulbs are a very efficient method for baking the microscope for while the internal surfaces of the column can reach 200°C, the lenses can still have cooling water flowing and never rise above 60°C. For a full bakeout of the microscope, the external lead shielding must be removed and flange heaters attached resulting in a two day downtime; however, in most cases a simple twelve hour halogen bake is sufficient to attain UHV. In addition, there are many ports that surround the specimen region allowing the user to attach a wide variety of surface science instruments as described later.

§3.3.2.1 The HREM Vacuum System

The success of the UHV-H9000 design stems from the use of clean and efficient pumping systems. The UHV-HREM does not rely upon cryogenic systems to achieve

or maintain UHV conditions, a feature that is quite unique. Furthermore, the UHV design takes advantage of the fact that the microscope column is a natural differential pumping system. Each of three sections of the column; the condensor, intermediary, and projector lens regions, all have a 20 ℓ /sec triode ion pump. While the pumping speed is not large, the volume is small. The objective lens/specimen region is pumped by a 420 ℓ /sec tandem turbo-molecular pump that has magnetically levitated bearings and is shock isolated from the microscope. In addition, a 1000 ℓ /sec titanium sublimation pump (TSP) located behind the microscope column was added as a Northwestern University modification (by JEB); at present this is needed only infrequently. As with its H9000 predecessor, the UHV-HREM has a triode ion pump for the LaB₆ electron gun, which operates at $<10^{-5}$ Pa, and a 400 ℓ /sec diffusion pump on the camera chamber.

The UHV-HREM is attached to a specimen transfer chamber (STC) to enable the user to exchange and fully characterize specimens without the microscope having to come up to atmosphere. The microscope and the STC are separated by a gate valve and welded bellows to minimize possible contamination and vibration problems. The STC is evacuated by a 60 ℓ /sec noble ion pump that removes gases such as argon well and has also been modified (by JEB) to include a 400 ℓ /sec TSP. These pumps can be isolated from the STC by a gate valve which is useful when specimen annealing cycles are performed. The STC is also equipped with a 50 ℓ /sec turbo-molecular pump that serves three functions: to rough pump the transfer chamber and assist in bakeout, to differentially pump the ion gun, and to evacuate the portable transfer system (PTS) described elsewhere. A base pressure of 1×10^{-8} Pa has been achieved in the STC so that there is no appreciable vacuum differential between it and the microscope.

It should be noted that even though the specimen region of the UHV-H9000 is clean, there still remain possible sources of contamination from the microscope. One

source is the use of viton O-rings where the column is joined to the viewing chamber and the electron gun; these represent diffusional leaks. Another is the presence of the diffusion pump on the camera chamber which contains oil and should be replaced by a turbo pump to increase its cleanliness and ultimate vacuum. Concurrent with eliminating contamination sources, the pumping speed of the microscope could be increased most notably in the projector/intermediary lens regions where the addition of small TSPs would lessen the burden on the ion pumps. These improvements to the UHV-H9000 represent continuing evolution in the marriage of microscopy and surface science.

§3.3.2.2 Surface Science Instrumentation

Both the UHV-HREM and the specimen transfer chamber are equipped with instruments to characterize surface and bulk properties. The microscope has six ports for instrumentation in the specimen region. Currently attached to these ports are an Auger spectrometer and two windows; with room for future expansion such as an optical probe for the study of desorbed species. The Auger, based upon Comstock model AC-901, is placed in the specimen chamber above the objective lens pole piece to collect signals from the region in the electron beam and is described in more detail by Ai (1989). Beneath the camera chamber is a Gatan 666 parallel electron energy loss spectrometer (PEELS) coupled with an off-axis Gatan 676 CCD-TV. An Apollo 3500 workstation, which is networked with the Northwestern University Multislice and Imaging System (NUMIS), is used to control the PEELS and to acquire digital images directly from the CCD-TV camera. Synergistic with digital image acquisition (by means of an Imaging Technology 151 frame buffer) the computer network can control the microscope CPU functions, such as beam tilt, and can be used for automatic alignment of the microscope.

The STC is equipped with a wide array of surface science instrumentation, including a Perkin-Elmer sputter ion gun, a Varian LEED/Auger optics, evaporation

sources, a Candella chemical dye laser, a high pressure (0.1-100 kPa) thermocouple gauge, and an Ametek quadropole mass spectrometer. The ion gun has Ar, Xe, He, and Ne gas sources, operates from 500 eV to 4 keV, and is used as a means of thinning bulk crystals and to clean those specimens that have accumulated carbonaceous surface contaminants. Because the ion gun is differentially pumped, it is operated at chamber pressures in the 10^{-5} Pa range. Auger spectra are acquired by means of the LEED optics and, even though the energy resolution is only about 10 eV, are still quite useful for determination of surface cleanliness and composition. In addition, the STC has a six-inch viewport, opposite the LEED screen, to which focusing optics can be attached. These optics enable the user to focus onto the specimen light from a broad-band annealing source (ILC Technology) or the pulse of the chemical dye laser for radiation damage studies. The top of the STC has four ports aimed at the specimen which can be used for a Kimball Physics electron gun (0-10 keV) to resistively anneal specimens, or any other desired instrumentation. See Figures 3.10 and 3.11 for detailed schematic drawings of the STC chamber and instrumentation.

It should be noted that the preceding description of the specimen transfer chamber has been included to give the reader an overview of the capabilities of the microscope/surface science system. In addition, the development of this 'prototype' microscope is essential to the success in the study of catalytic surfaces such as UFPs, and a great deal of effort has been expended to this goal. But while the STC has many surface science instruments and capabilities, they are ancillary to the main function of the STC for this research; namely a means to get the specimen from the UHV furnace to the UHV microscope. In this respect the STC is treated mainly as an specimen airlock and more detailed descriptions of the STC can be found elsewhere in the literature (Bonevich and Marks 1989a, 1990b).

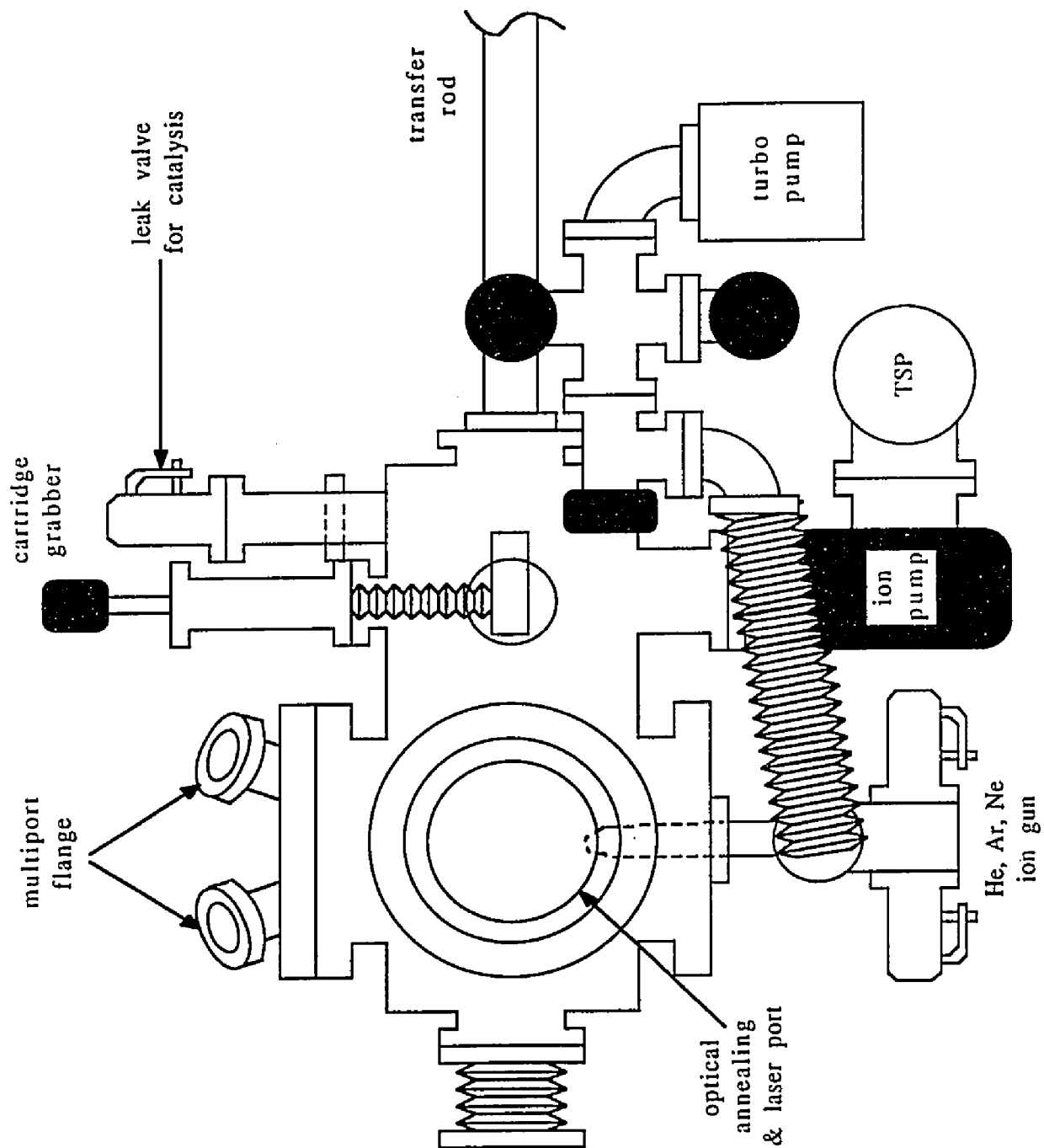


Figure 3.10(a). The side view of the specimen transfer chamber showing, among others, the ion milling, controlled atmosphere, and specimen exchange facilities.

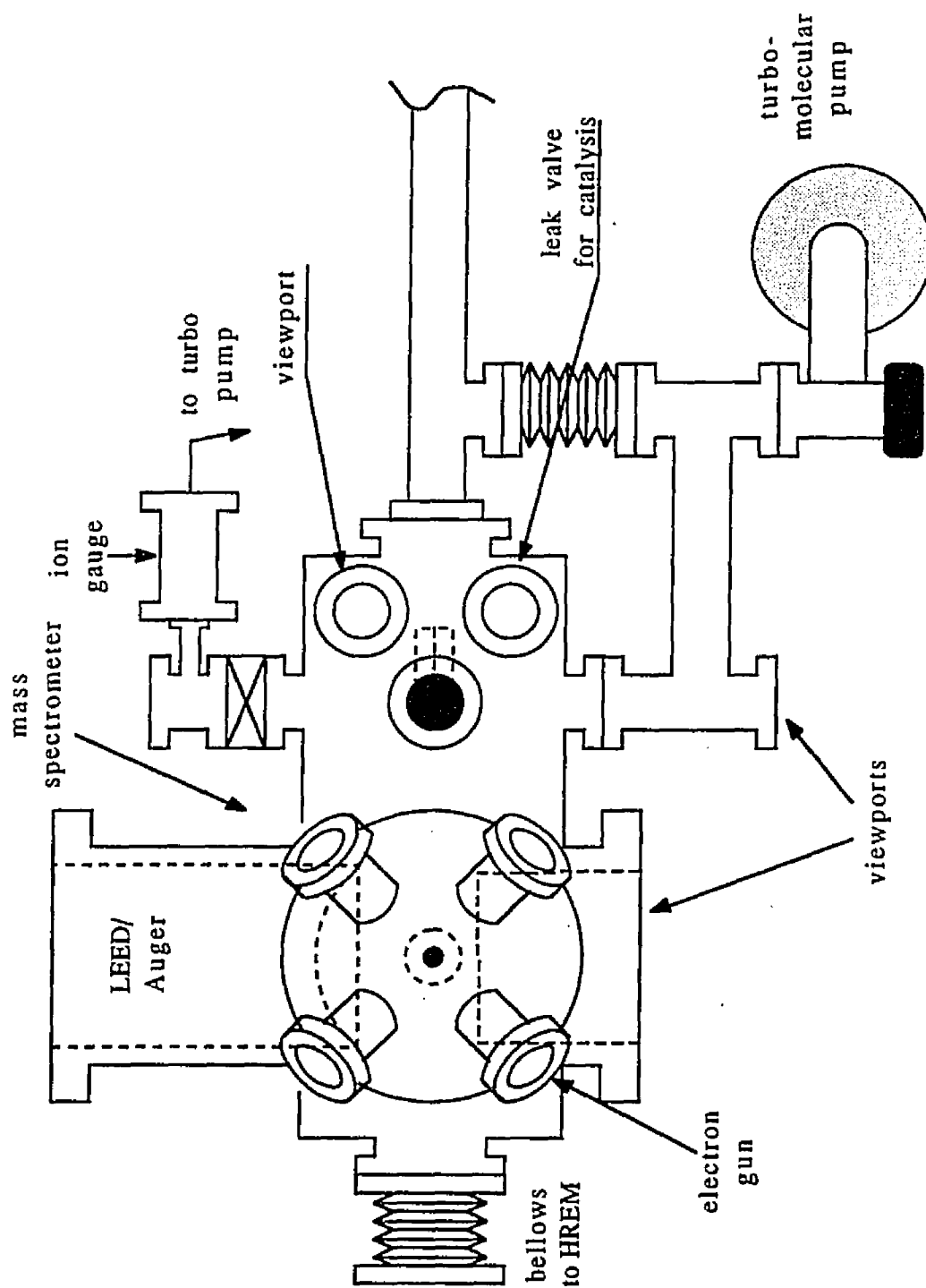


Figure 3.10(b). The top view of the specimen transfer chamber showing the multiport flange, the LEED/Auger optics, the specimen exchange port, and the recessed viewport.

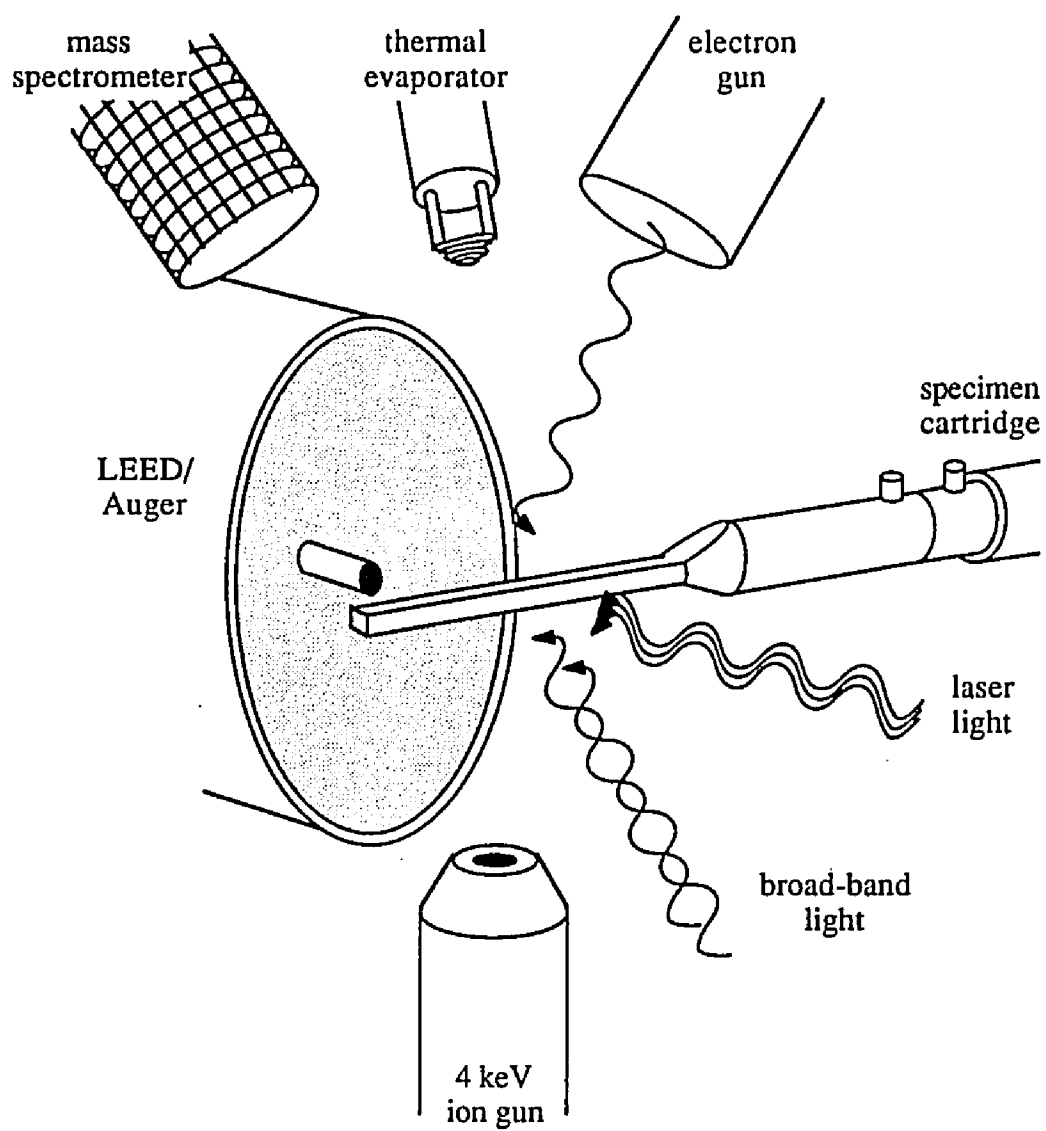


Figure 3.11. The STC surface science instrumentation with line-of-sight at the specimen.

§3.4 Specimen Exchange

Introduction of a specimen into the UHV-H9000 is accomplished by means of a custom-made (by JEB) grabber design that ensures complete vacuum transfer. The PTS is attached to a gate-valved port on the side of the STC. The space between the gate valves of the PTS and the STC is then pumped down via the turbo pump which, within an hour, can reach 10^{-5} Pa ($\approx 10^{-7}$ Pa after a bakeout) as monitored by an ionization gauge. At this time, the turbo is isolated from the system and the gate valves opened to the STC. The PTS moves the specimen into the STC where it is grabbed and detached from the rotary/linear feedthrough (the grabbing process takes less than five minutes). Once the PTS feedthrough is retracted, the gate valves are closed and the specimen is manipulated and picked up by the microscope's transfer rod. The specimen can then be immediately inserted into the microscope for observation.

The preceding sections have outlined, in some detail, the design considerations and instrument capabilities of both the UHV furnace and UHV microscope systems. It must be noted that without either instrument, the investigation of sintered UFPs would not have been a success. In addition, the fact that the daunting design challenges presented by this project were in large part surmounted provides hope for future prospects. For example, the PTS allows specimens to be introduced from a variety of remote UHV chambers and the UHV furnace can easily be adapted to a plasma or microwave system.

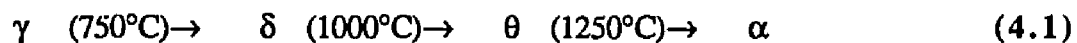
More detailed drawings which were used to design the UHV system can be found in Appendix Five.

Chapter Four. Experimental Results and Analysis

The experimental results chapter, summarizing the majority of the work done with the ultrafine alumina particles, is organized into three main sections. The first section outlines the structure of the small particles from the vantage of initial particle production. That is, these particles are not necessarily sintered, but do provide an insight to the structure resulting from the arc discharge. The second section follows the structural evolution of the ultrafine particles as they sinter in the flowing gas furnace, including phase transformations and neck formation. The final section provides an overall analysis of the sintering process and other important processes occurring during sintering.

§4.1 Initial (unsintered) Particles

The arc discharge production of UFPs, consistent with other methods, results in a wide variety of equilibrium phases. In fact, it would be fair to say that much of the Greek alphabet has been consumed in the naming of alumina phases. Nevertheless, we can classify various phases into specific groups based on some simple structural units. For example, if we consider that γ -alumina can be made by the calcination of boehmite (aluminum hydroxide), we can then follow the transformation of γ - to α -alumina as a function of temperature;



where the γ and δ phases (loosely-used names) are based upon the spinel structure, the θ phase on monoclinic units, and the well-known α is rhombohedral (hexagonal). The transformation of the low temperature γ and δ phases to the α phase can be considered as an ordering transformation where the α (corundum) structure represents the highest degree of order having only one, well-defined structure. The lower order phases have many

variants and therefore are labeled in a very loose fashion, though it is not entirely correct to do so.

A review of the published literature on transition-phase aluminas reveals a wide variety of structures that fall into the γ - and δ -alumina spinel classification. For example, there are four different cubic alumina phases classified as γ with cell parameters of 0.396, 0.775, 0.794, and 0.795 nm (Structure reports 1988). The common element in all these structures is that they are cubic, but in general no further indications of the structure are given (i.e. no space group or atom position information). The exception is the widely cited structure of 0.79 nm of Rooksby (1951) who determined that the spinel structure of space group $O_H^7 - Fd3m$ was correct.

The spinel structure is highly complex and in its simplest form consists of a double fcc packing of the oxygen anions with the metal cations filling the octahedral and tetrahedral sites (Smith 1982). A typical example of spinel is $MgAl_2O_4$ (MAO) with a unit cell parameter of 0.82 nm. In MAO the aluminum cations occupy the octahedral sites and magnesium the tetrahedral sites; this is referred to as *normal* spinel. Furthermore, only one-half of the octahedral sites and one-eighth of the tetrahedral sites are occupied in the spinel structures. In the *inverse* spinel, the tetrahedral sites are occupied by aluminum with a random mixture of magnesium and aluminum on octahedral sites. The normal and inverse variants represent the two extremes of the spinel structure and there are many crystallographic arrangements in between. For example, a completely random mixing of tetrahedral and octahedral atoms results in the *fully-disordered* spinel.

The important point to note is that with MAO the crystal form is $T^{2+}(M^{3+})_2O_4$. However, with the aluminas we can make no distinction between the different valence states of the cations in order to determine true structure as can be done in the case of magnetite, Fe_3O_4 (Dieckmann 1982). It would also be exceedingly difficult, from the

standpoint of electron scattering factors, to distinguish between Al^{2+} and Al^{3+} ions, if such ions were possible. The only recourse available is to assign occupancies to different sites in the lattice to match the experimentally observed images. For instance, in the fully-disordered spinel octahedral sites would have an occupancy of unity, whereas the tetrahedral sites are only two-thirds occupied in a random fashion to maintain the proper stoichiometry of Al_2O_3 , or $(\text{Al}^{3+})_{2/3}(\text{Al}^{3+})_2\text{O}_4$.

§4.1.1.1 *Delta Alumina*

The δ -phase of alumina is also based upon the spinel structure and, being a variant of γ , has a number of structural possibilities. Lippens and deBoer (1964) reported the formation of a tetragonal phase having the cube dimensions with the c-axis of triple cube length. Rooksby and Rooymans (1961) reported a tetragonal variant of alumina having cell parameters of 0.796 and 1.17 nm. Though no space group information was provided, the X-ray powder pattern was given along with the peak intensities. In support of this structure Dauger and Fargeot (1983) proposed a tetragonal unit cell of identical dimensions that differed from the cubic spinel by the introduction of anti-phase boundaries (APB) at $1/4\langle 110 \rangle$ in the $\{100\}$ planes. Their proposed structure did suffer from a crystallographic drawback. Their structure does not lead to a complete unit cell if the crystal is viewed down any of the original cube axes. This results from the fact that the $3/2$ expansion is not a unit cell translation vector (i.e. the crystal is not periodic). While the oxygen sublattice is actually composed of 8 fcc unit cells, 2 to a cube edge, and does not have to adjust to accommodate the $3/2$ expansion, the question then becomes where to place the cations in the new unit cell to maintain periodicity.

Fargeot et al. (1990) later refined their structure by means of X-ray and electron scattering of large crystals to conclude that the tetrahedral sites near the cell boundaries were vacant and that the remaining octahedral atoms relaxed into the open structure.

However, there were numerous typographical errors in their published structure data which was slightly orthorhombic ($a=0.998b$) and had a space group symmetry of P222. In addition, the proposed unit cell also resulted in a slight defect stoichiometry of $Al_{34}O_{48}$. However, the idea that the structure is generated by ordering on the tetrahedral sites is an appealing one for the reason that the structure of the octahedral sites closely matches the fcc packing of the oxygen sublattice, unlike the tetrahedral sites.

The δ -phase of alumina has also been reported (Jayaram and Levi 1989) to have an orthorhombic unit cell (space group $P2_12_12_1$) with dimensions of $2a_\gamma$, $3/2a_\gamma$, and a_γ where a_γ is the cell parameter of their cubic γ -alumina ($a_\gamma=0.82$ nm). This structure also required the introduction of APB's along the $3/2$ {010} planes, though no attempt was made to specify exact cation atom positions. However, their analysis of the transmission electron diffraction patterns (TEDs) revealed that there was substantial ordering along the {400} and {440} planes in the lattice suggesting that the octahedral sites remained largely unperturbed by the transformation from γ - to δ -alumina. The ordering of the octahedral sites contrasted with that of the tetrahedral sites where it was noted that the intensities of the {220} reflections (where the tetrahedral sites contribute) was much less than that expected from a totally random distribution. These results indicated that in δ -alumina the octahedral sites had full occupancy (but are slightly distorted from their original spinel sites) whereas the tetrahedral sites had an ordering of vacancies as opposed to being randomly distributed.

Table 4.1: Reported structures of δ (spinel-type) aluminas.

<u>a(nm)</u>	<u>b(nm)</u>	<u>c(nm)</u>	<u>S.G.</u>	<u>Reported by</u>
0.79	0.79	2.35	--	Lippens and deBoer (1964)
1.64	1.18	0.82	$P2_12_12$	Iijima (1985)
1.64	1.24	0.82	$P2_12_12_1$	Jayaram and Levi (1989)
0.795	0.792	1.170	P222	Fargeot et al. (1990)

Iijima (1985) also reported the formation of an orthorhombic phase of alumina, dubbed δ' (space group $P2_12_12$) with cell dimensions of 1.64, 1.18, and 0.82 nm. Since Iijima's aluminas were produced in a similar fashion to those in this study, namely the arc discharge, one would expect that the particles observed here to closely resemble those of Iijima. Iijima determined the structure on the basis of micro-beam electron diffraction from small particles and also presented high resolution electron micrographs (HREM) of the structure suggesting that twinning was the mechanism to form the new δ' -phase. As with previous studies, Iijima made no attempt to specify exact atom positions for the purpose of image simulations and only presented HREM of the [010] zone axis orientation.

§4.1.1.2 Theta Alumina

The ordering transformation from δ to α requires the formation of the θ -phase as an intermediate. The θ -phase is generally agreed to have monoclinic symmetry which can be considered as pseudo-orthorhombic if the structure is twinned. Tertian (1950) determined θ -alumina to be isostructural with β - Ga_2O_3 , but required a hexagonal unit cell. Saalfeld (1960) observed a monoclinic phase with space group $C2/m$. Other θ -phases have been reported; see Table 4.2.

Table 4.2: Reported structures of θ -alumina.

a(nm)	b(nm)	c(nm)	b(°)	S.G.	Reported by
1.181	0.291	0.562	104.1	$C2/m$	Stumpf (1950)
1.174	0.572	1.124	103.3	$C2/m$	Saalfeld (1960)
0.56	0.29	1.18	103.8	$A2/m$	Wilson (1980)
1.11	1.21	1.77	103.3	$B2/m$	Iijima (1985)
1.21	0.56	0.29	103.3	$B2/m$	Iijima (1985)

The θ -phases reported by Iijima also occurred in the powders formed by the arc discharge and were considered to be structurally different from the β - Ga_2O_3 phase reported

previously. The structures reported by Iijima were also determined by micro-beam TEDs and convergent beam (CBED). In general, the HREM images of the θ -aluminas presented by Iijima were not of the same quality as the δ '-phase and no attempt was made to calculate atomic positions or to simulate images.

§4.1.2 Present Results

This section contains the results from the present study of the formation of transition phase aluminas produced by the arc discharge. The analysis of powders observed in three different microscopes will be presented. The initial HREM work was performed in the H9000 where the contamination rates could not be controlled, the nano-diffraction patterns were obtained from the HF2000 FETEM (uncontrolled environment), and finally HREM of the sintered and unsintered powders in the UHV-H9000 was obtained.

The powders produced by the arc discharge were initially observed in the H9000 for structural characterization. The powders observed consisted of both the γ - and δ -aluminas based on the spinel structure. Figure 4.1 is a typical example of a γ -alumina aligned along the [011] zone axis. The structure can be modeled in the following manner; the MAO spinel structure is assumed, as with Rooksby, where the aluminum cations on octahedral sites have full occupancy and the tetrahedral cations are only partially occupied. In order to simulate an HREM image it is necessary to treat all of the tetrahedral sites (excluding the seven-eighths having zero occupancy) as equally occupied. That is, a random distribution of vacancies is imposed resulting in all tetrahedral sites being two-thirds occupied. The random distribution is supported by Jayaram and Levi who noticed that the transformation of γ - to δ -alumina was accompanied by an ordering process on the tetrahedral sites.

The calculated images of the γ -alumina are shown in Figure 4.2 as the function of

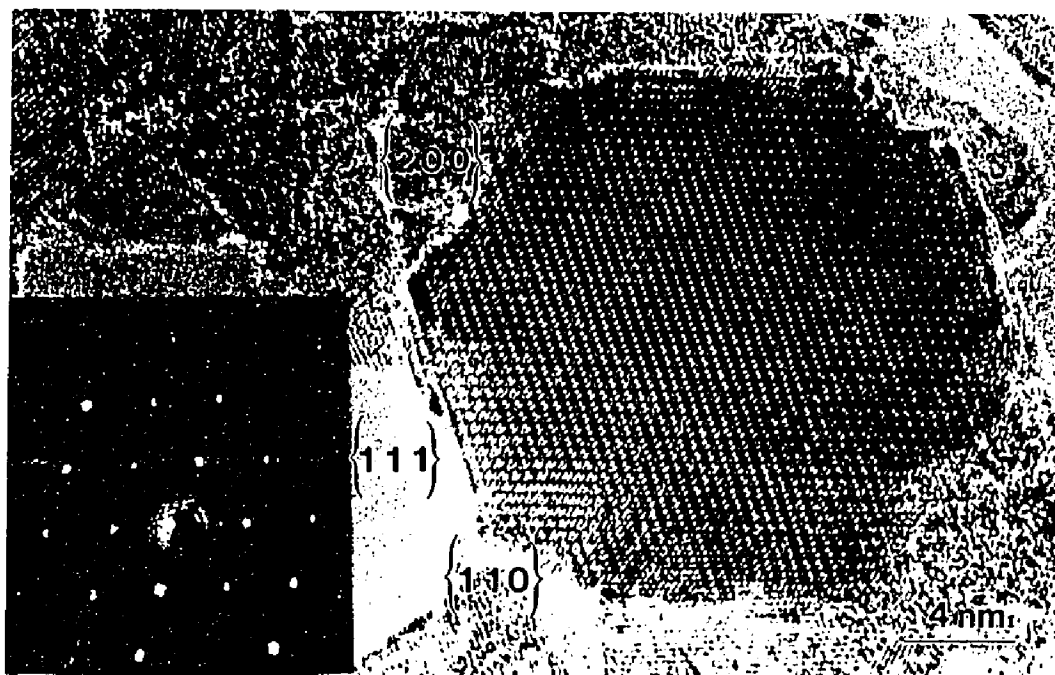


Figure 4.1. γ -alumina spinel particle aligned near to the $[011]$ type zone with ODM as inset. The $\{111\}$, $\{200\}$, and $\{110\}$ facet types are labeled.

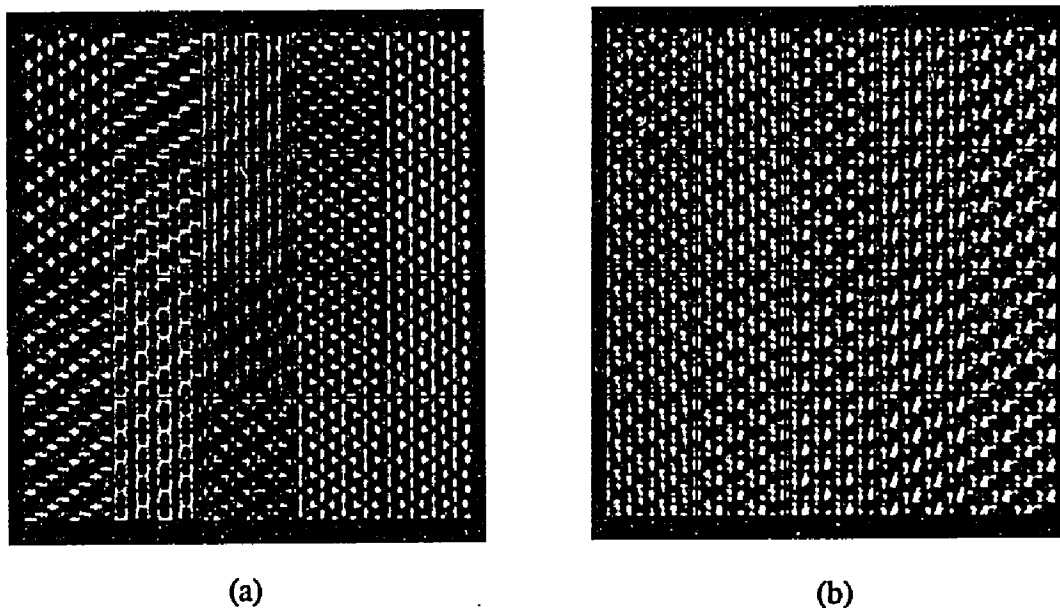


Figure 4.2. Calculated images of the alumina spinel. Thickness of 10 nm as a function of lens defocus; starting at -40 nm in steps of -2 nm. (a) no tilt and (b) 2 mrad of tilt. The focal series start at the upper left, moves down the columns to the lower right.

the objective lens defocus, i.e. a through focal series. Here the crystal thickness is held constant at ≈ 10 nm which is a good approximation of the edge thickness across a {110} facet of a 25 nm UFP. As revealed by the simulation, the white dots in the image correspond to the tetrahedral sites in the lattice where the diffuse scattering stems mainly from the octahedral sites, for a schematic representation of the structure, see Figure 4.3. The γ -phase was also observed in the $[\bar{1}12]$ zone axis orientation, see Figure 4.4. Here, though the surface is contaminated by the uncontrolled environment of the CTEM, the insetted optical diffractogram (ODM) clearly shows the crystal orientation with the correct reflections and spacings.

The analysis of these crystals was done by assigning the proper Miller indices to the given crystal reflections. The resulting interplanar spacings are calculated by the well-known formula for orthogonal unit cell materials;

$$d_{hkl} = \left[\left(\frac{h}{a} \right)^2 + \left(\frac{k}{b} \right)^2 + \left(\frac{l}{c} \right)^2 \right]^{-1/2} \quad (4.1)$$

Applying eqn. 4.1 to the measured interplanar spacings results in a lattice parameter for γ -alumina of 0.79 ± 0.01 nm. This agrees well with the previously observed structures although there are indications that our γ -phase may in fact be slightly tetragonal. Consider for example that one set of {111} spacings corresponds to 0.46 nm which gives a unit cell lattice parameter of 0.8 nm. Another set of {111} planes measures 0.45 nm which would correspond to a lattice parameter of 0.78 nm. These measurements fall within the experimental error, however the presence of distortions in the spinel structure due to defects certainly is plausible as is the case with our δ -alumina.

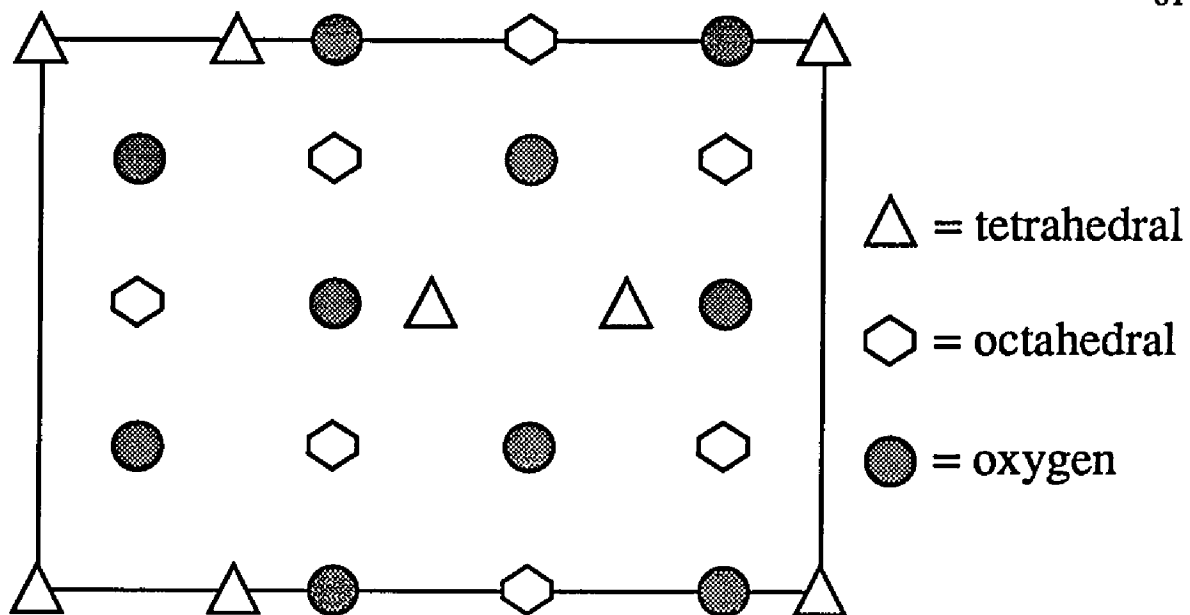


Figure 4.3. Schematic representation of the spinel structure viewed down the [011] zone.

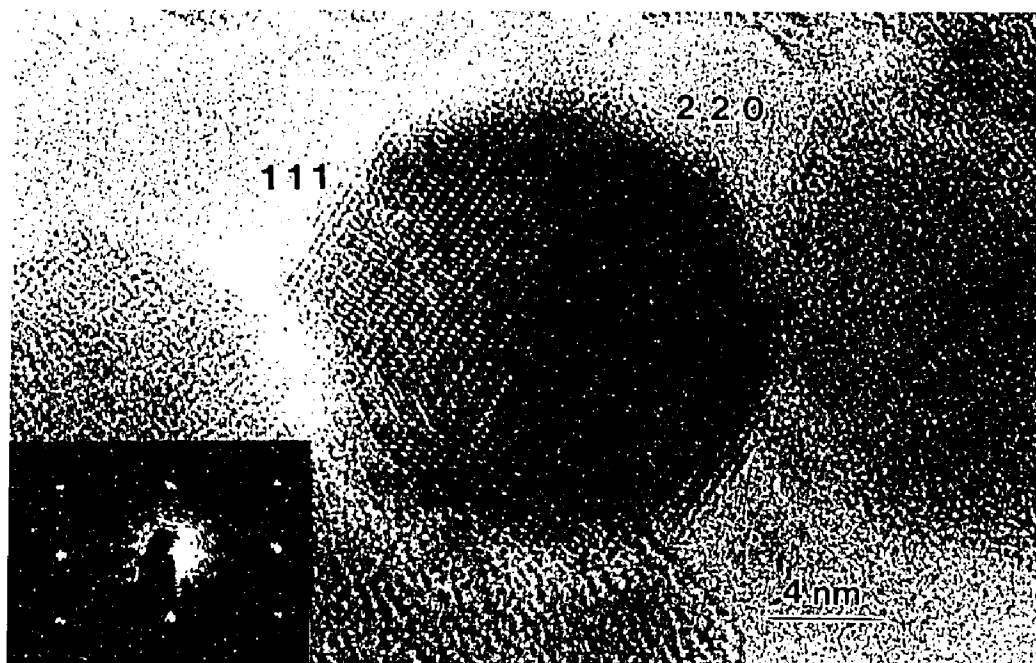


Figure 4.4. γ -alumina spinel particle oriented along $[\bar{1}12]$ zone with insetted ODM.

§4.1.2.1 Delta Alumina

The δ -phase of alumina was also observed in many of the arc discharge powders. In fact, the results of X-ray powder diffraction conducted on unsintered powders from the smoke (by MHT) revealed that the δ -phase was the majority phase, comprising some 60% of the sample with 40% γ -phase. The δ -phase, as mentioned earlier, is a variant of the spinel structure and so many of the X-ray reflections from both γ - and δ -phases overlap. But whereas the X-ray results must be interpreted carefully, the HREM images and DPs of δ -alumina clearly show the expansion of the unit cell. Consider for example Figure 4.5 the DP of a rather large particle of the δ -phase oriented near to the [011] zone axis. In this orientation, the Bragg conditions for the (100) and (0 $\bar{1}$ 1) reflections are satisfied. As the particle is much larger than those typically found in this study, an SADP was obtained which allowed the true structure of the phase to be determined. In addition, DPs without the SA were obtained revealing the structure of the particle along the electron beam. That is, the higher order Laue zones are revealed indicating that the δ -phase is indeed a large unit cell material; a schematic representation is shown, in addition to the zero-order Laue zone.

As a result of the DP analysis, the lattice parameters of the δ -phase are determined to be $a_{\delta}=1.58$ nm, $b_{\delta}=1.17$ nm, and $c_{\delta}=0.79$ nm. These values, while similar to those previously reported, represents an $\approx 4\%$ contraction of the unit cell as compared with the δ -phase of Iijima (1985) and Jayaram and Levi (1989). However, the c_{δ} dimension (cubic basis) does agree with the X-ray literature. The dimensions of this new phase, tentatively dubbed δ_{JEB} , is also supported by the examination of the same phase along different crystal orientations. Consider Figure 4.6 which shows the image and DP of another large particle of δ -alumina where the zone axis corresponds to [102]. When evaluating the δ -phase it is important to recognize that the orthorhombic phase is a direct consequence of the cubic spinel material. Thus, many of the basic reflections observed are shared with the γ -phase.

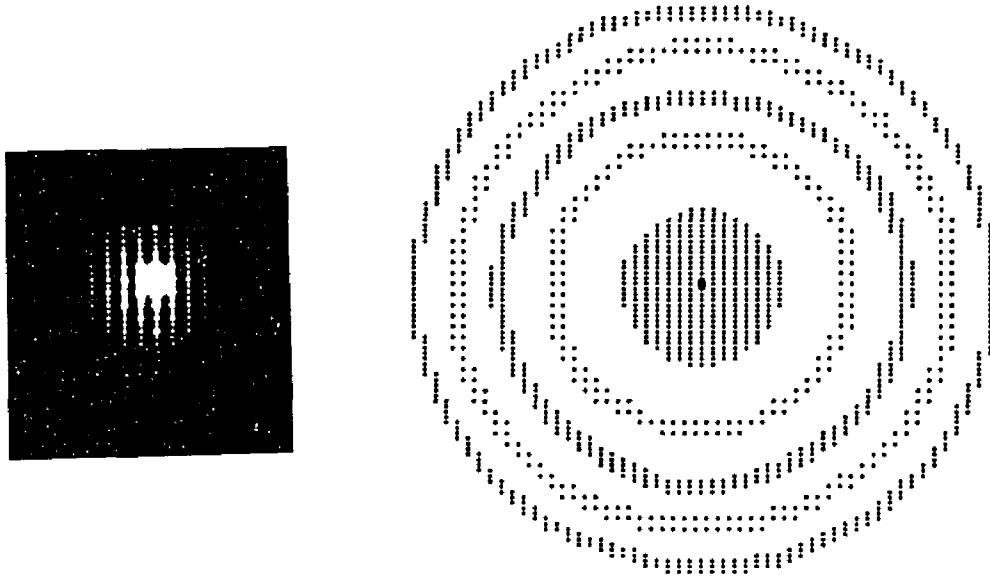


Figure 4.5. Schematic representation of the diffraction pattern from δ -alumina particle of the [011] zone. The actual zero order Laue zone is shown at the left.

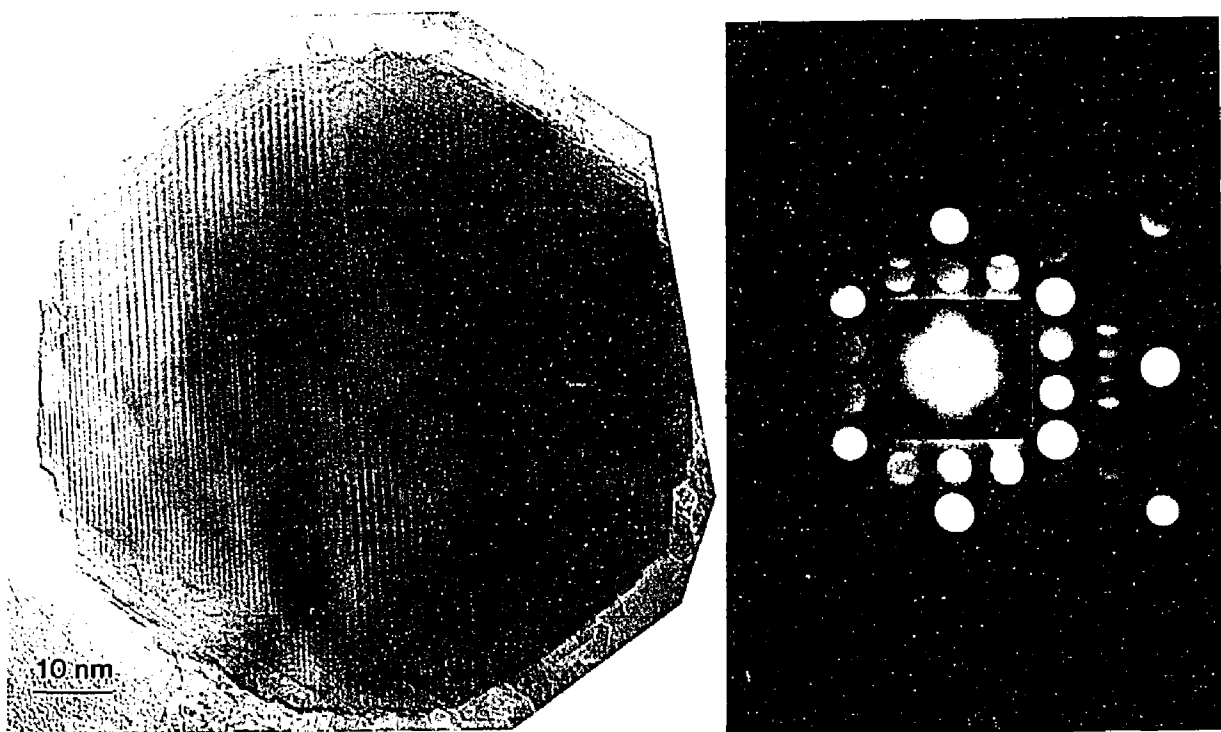


Figure 4.6. Large particle of δ -alumina oriented along the [102] zone. The DP in (b) has obviously been montaged to bring out all intensities in the pattern.

When one examines the DP, it is apparent from the strong intensity reflections that the $[102]_{\delta}$ is structurally similar to the $[101]_{\gamma}$ orientation. In fact, the ordering occurs as follows; $(400)_{\gamma}$ is synonymous with $(060)_{\delta_{\text{JEB}}}$ and $(202)_{\gamma}$ with $(44\bar{2})_{\delta_{\text{JEB}}}$.

In addition to having interplanar spacings consistent with the new δ_{JEB} phase this DP was taken under 'converged-beam' conditions. That is, the electron beam was focused to the smallest probe attainable under normal HREM conditions. These conditions allow one to use the intensities of the DP to determine the most probable space group of the diffracting crystal. From the DP it is apparent that two possible space groups are $P2_12_12$ or $P2_12_12_1$. The exact determination of the space group is impossible unless one uses true CBED (as opposed to 'CB'ED) where the distribution of intensity within the diffracted discs is analyzed for all possible crystalline symmetries. The CBED technique on the H9000 HREM is impractical when used to examine these large alumina particles where size and strains may affect the CBED results.

§4.1.2.2 Nano-diffraction Results

Most of the UFPs observed in this study fall within a size range of 20 to 50 nm. Consequently, the smallest electron probe of the H9000 HREMs invariably gives polycrystalline DPs precluding a precise determination of particle structure. In order to obtain more precise DPs from the UFPs, the HF2000 microscope was used to examine unsintered specimens. In general, this microscope has a probe size of ≈ 1 to 10 nm which is useful to obtain DPs from individual crystals. Typical DPs obtained from the HF2000 are shown in Figure 4.7. These results support the X-ray and HREM data which indicate that the unsintered UFPs consist of both γ - and δ -aluminas. Unfortunately, though the intensities within the diffracted discs contain structure information, the interpretation of this intensity is not unique, due to particle size and strain effects, and it is fraught with danger to ascribe more meaning to the patterns, other than general symmetries. Other results

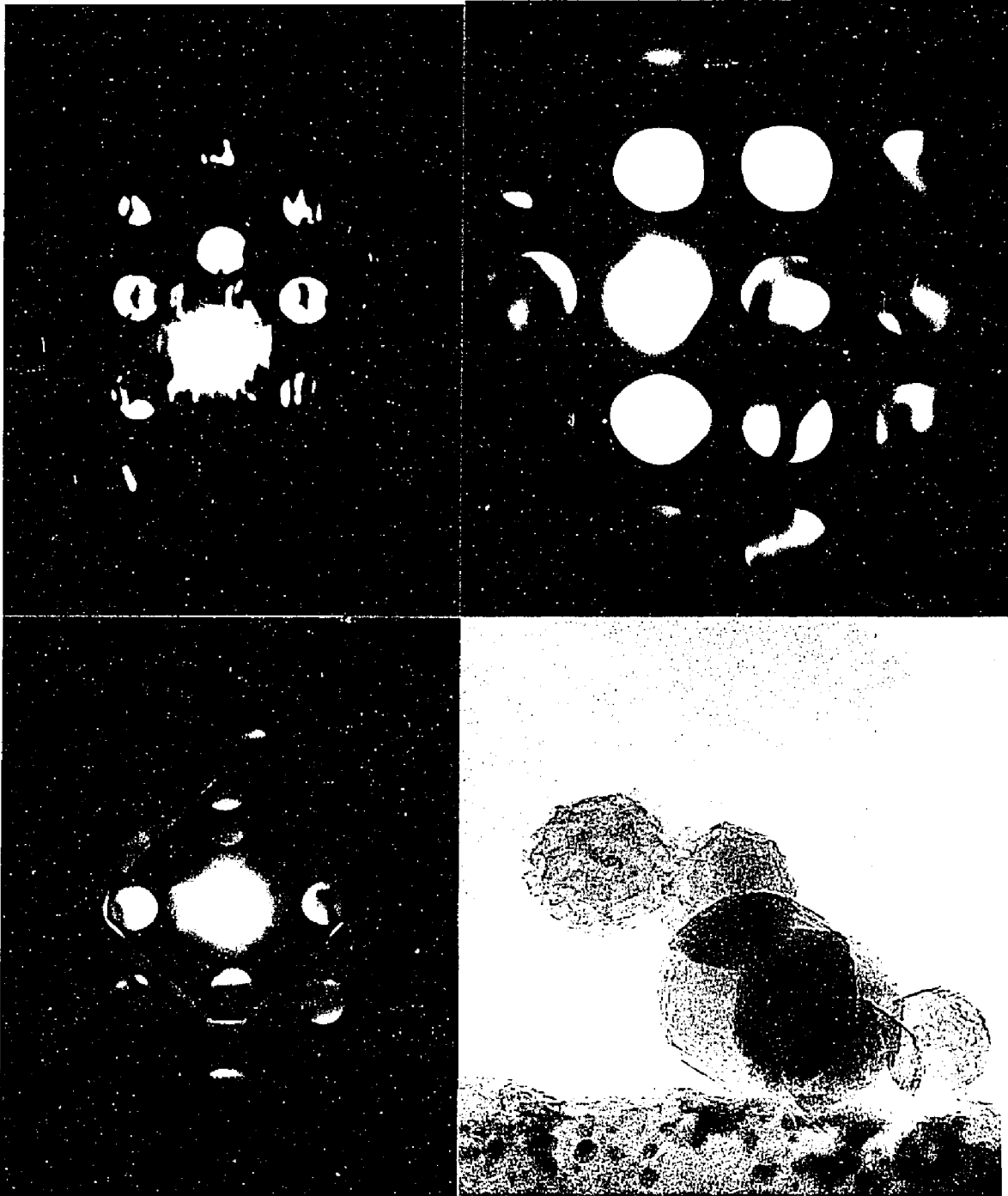


Figure 4.7. Typical diffraction patterns from the HF2000 showing in (a) the $[111]_{\gamma}$, in (b) the $[100]_{\gamma}$, in (c) the $[112]_{\gamma}$, and (d) a particle with 5 minutes beam damage (Appendix 1).

from the HF2000 are given in later sections; such as the chemical analysis (PEELS) of the unsintered particles (§4.2.3) and the effects of electron beam-particle interactions resulting in electron radiation damage (Appendix 1).

§4.1.3 Surface Faceting

It is clearly evident that virtually all of the UFPs have faceted surfaces which correspond with the close-packed planes of the crystal. Such faceting is to be expected when one considers that under equilibrium conditions the particle shape is given by the Wulff polyhedra. The Wulff polyhedra [following the derivation of Herring (1951)] is the shape that satisfies the constraint that, for a certain amount of matter in a particle, the following quantity is minimized;

$$\int \gamma dA \quad (4.2)$$

where γ is the excess free energy per unit area of the particle surface (the surface is considered to be strain-free), A the area of the surface and the integral is over the entire particle surface. This relation is only valid for those cases where the particle is under thermodynamic equilibrium. Any kinetic effects at high temperature, which may change the shape of the particle, must occur fast enough for equilibrium to occur; we shall neglect them henceforth. This surface minimization problem was formulated by Gibbs in 1878 and solutions have been given by many authors including Wulff (1901) and Dinghas (1944). Essentially, the Wulff polyhedra is constructed in the following manner (from Herring);

“Consider the γ plot, defined...as a closed surface whose radius vector in the direction of any unit vector \mathbf{n} has a length proportional to the surface tension $\gamma(\mathbf{n})$ of a plane normal \mathbf{n} . Draw a plane through the end of each radius vector of this surface and perpendicular to the radius vector. Then, according to Wulff, the body formed by all points reachable from the origin without crossing any of these planes will be geometrically similar to the equilibrium shape.”

Thus the equilibrium shapes of the UFPs are a direct consequence of the Wulff construction. It is an important point to note that for constant γ (isotropic excess surface free energy) the minimum surface area per unit volume has long been recognized to be a sphere. For the case of γ -alumina particles with the 'fcc' spinel structure, the Wulff polyhedron is comprised of facets corresponding to the {111}, {200}, and {220} families of planes. These surfaces have the highest densities of atoms and thus minimize the overall excess surface free energy. The surfaces with the lowest free energy will dominate the equilibrium shape; i.e. the facets can be ranked accordingly;

$$\gamma_{111} \leq \gamma_{200} < \gamma_{220} \quad (4.3)$$

Thus we expect that the equilibrium shape of a γ -alumina particle to present eight {111} facets, six {200} facets, and twelve {220} facets. In fact, the {220} are locally unstable with respect to the Wulff construction and decompose into smaller sets of {111} facets, e.g. Figure 4.1.

Upon observation of the UFPs, it was noticed that as the particle size decreased the faceting became more pronounced (Bonevich 1989). Large particles appear 'spherical' and upon closer examination are, in fact, comprised of many smaller surface facets. The large particle surfaces can be considered as a series of facet terraces separated by surface steps where the step-step distance is small. When the particle size decreases, the length (the 2-D projection of terrace size) of a particular facet increases, commensurate with increasing step separation, until the surface consists entirely of unstepped facets.

A number of UFPs were analyzed for their facet structure by constructing their respective Wulff polyhedra. In all cases the Wulff construction was a 2D cross-section through the [011] projection, see for example Figure 4.8. Given the Wulff construction for each particle, the relative contribution of each facet type was calculated. For the sake

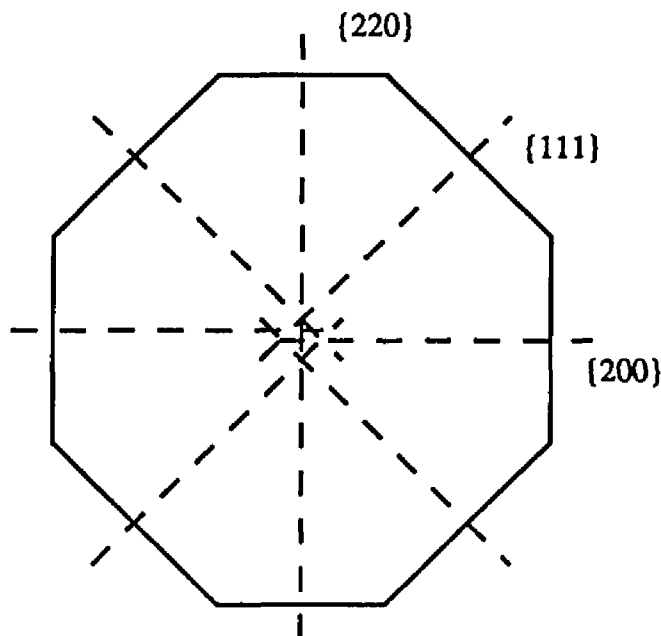


Figure 4.8. Wulff construction of the [011] zone. Each facet's perpendicular bisector intersects with the Wulff center of the particle. The {220} facets are treated as locally flat.

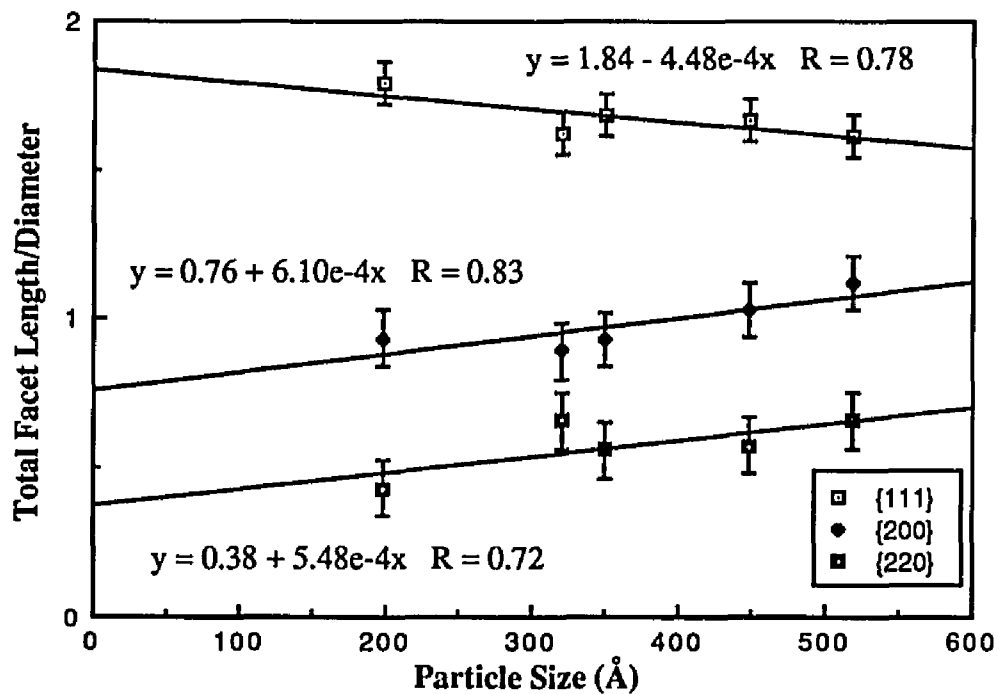


Figure 4.9. Plot of the total facet length scaled by particle diameter vs. diameter. As the size decreases, the {111} facets grow at the expense of the {200} and {220}. The linear regression fits of the facet data are shown where R is the correlation factor.

of simplicity in the analysis, the {220} facets were considered as locally flat facets; however it is obvious that in all cases they are comprised of {111} vicinal surfaces.

The total facet length was calculated by multiplying the total number of each type of facet in the projected Wulff construction by its average facet length. Thus, a natural result of this calculation is that {111} facets will contribute to a larger share of the surface structure (that is, there are more {111} facets for a given average facet length). The total facet length is then divided by the particle size to bring all particles to the same scale. If one then plots the total facet length (scaled by the diameter) versus the particle diameter, as in Figure 4.9, it is obvious that as the particle size decreases the surface develops {111} facets at the expense of the {200} and {220} facets as recognized by Marks (1985c). If one extrapolates the range of the linear regression to even smaller particle sizes, say 5 nm, then we might expect to find particles that are characterized entirely by {111} facets. This faceting behavior is not surprising given the fact that small particles of Au or Ag are known to develop sharply faceted surfaces, such as multiply-twinned particles (Marks 1984; Iijima and Ichihashi 1985, 1986, 1987; Ino 1966, 1969; Ino and Ogawa 1967; Allpress and Sanders 1967).

An interesting feature in this graph is the y-intercept due to the fit of the data. At first glance, it is not clear what is the physical significance of having a facet length almost twice the diameter. However, if we consider the simplest case where the surface energies are isotropic then the Wulff construction becomes a sphere (a circle in projection), as noted earlier. Then it is obvious that the total facet length of all facets is really a measure of the particle circumference, πD . If one then scales the circumference of the circle by its diameter, the result is simply π . Upon inspection of Figure 4.9, and adding the intercepts for all facet types together, one obtains a value of ≈ 3 which is within 10% of π .

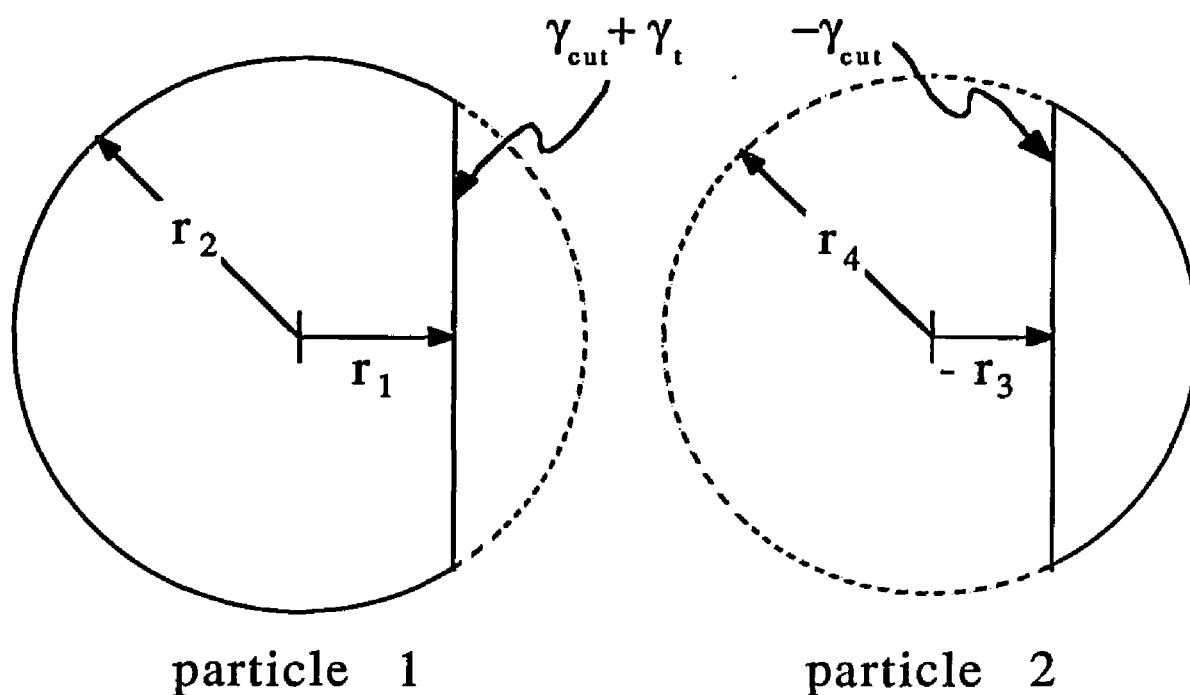


Figure 4.10. Schematic representation of a twinned particle showing the mathematical cut along the twin boundary. Values of r_i are measured from each particles' respective Wulff centers, i.e. $r_1 \neq r_3$.

An important point to note is that some particles deviate from the linear faceting behavior, as does the 32 nm particle. The deviation is caused by the presence of a twin on the $\{111\}$ habit plane which alters the nature of the surface. These particles can be treated by means of a modified Wulff construction which was used for MTPs by Marks (1983). The approach here, taken in the spirit of Marks, is based on the treatment of Ajayan (1989) where the twin is mathematically cut and the energy portioned to each side of the particle. A schematic representation is shown in Figure 4.10 where circles have been inscribed about the Wulff construction for a twinned particle. The contribution of the twin energy can be determined by knowing that;

$$\gamma_t + \gamma_{\text{cut}} = (r_1/r_2) \gamma_{111} \quad (4.4)$$

$$-\gamma_{\text{cut}} = (-r_3/r_4) \gamma_{111} \quad (4.5)$$

$$\therefore \gamma_t = (r_1/r_2 - r_3/r_4) \gamma_{111} \quad (4.6)$$

where γ_t is the twin boundary energy, γ_{cut} the mathematical cut energy and r_i the radius vectors of the γ -plot as defined in Figure 4.10. Analysis of twinned particles results in a ratio of γ_t/γ_{111} of ≈ 0.06 . Typical values of this ratio in fcc metals is ≈ 0.01 , thus our result is reasonable and it is not surprising that a ceramic material, with highly ionic bonds, would have a slightly higher twin energy. An approximate value for the twin energy can be calculated if one assumes the twin energy to be half the stacking fault energy (Coulomb 1978). The stacking fault energy for the basal plane of α -alumina was determined by Howitt and Mitchell (1981) to be 320 mJ/m^2 . If one considers this value as reasonable then the resulting twin energy in γ -alumina is 160 mJ/m^2 with a γ_{111} energy of 2.6 J/m^2 . This value is comparable to the energies of relaxed α -alumina surfaces calculated by Tasker (1984). However, these values should be tempered in light of the fact that extending the faulting behavior of fcc crystals to materials of the spinel structure is not entirely correct (Fadeeva et al. 1977).

It must be noted that the Wulff construction arguments above are only valid in the special case where the boundary between the two Wulff constructions exactly matches. That is, the mathematical cut along the twin is allowed in the case of a two dimensional Wulff construction, as shown above, or the simplest case of a 3D construction which is isotropic (a sphere). This Wulff construction treatment alone does not apply to the situation where the surface is strongly faceted in three dimensions. This situation requires some distortions to the Wulff construction in order to obtain boundary matching (see §4.3).

§4.2 Sintered Ultrafine Particles

Given that the initial particles formed by the arc discharge are a mixture of γ and δ phases, the question then becomes to determine the structure of the UFPs after sintering has occurred. From the onset of this section, it is imperative to point out that the structural evolution of the UFPs can not be determined *in-situ*. That is, the sintering conditions are determined by the temperature and flow conditions of the furnace and a matter of hours elapses before the particles can be observed in the UHV microscope. The *modus operandi* of this sintering study is to assume that the sintering process is quenched by the specimen cartridge and no further sintering processes occur, even during observation in the electron microscope. This assumption is quite reasonable, but it is still an assumption.

§4.2.1 Structure

All sintered specimens were observed in the UHV-HREM to minimize any effects of contamination on the structure and surface behavior of the UFPs. Thus all structural characterization will refer back to those structures which were determined in the CTEM for comparison. Virtually all of the particles observed after sintering could be classified into the spinel structures (γ or δ). However, a number of particles observed which exhibited a high degree of structural order were not easily indexed to fit simple γ or δ zones. But given their similar facet shape to those expected from the spinels, an effort was made to determine if a γ -alumina particle oriented along a higher order zone could give the same type of image contrast. The analysis procedure was as follows;

- Since electron diffraction patterns could not be obtained from the ultrafine particles (which would have eliminated the structural ambiguity), optical diffractograms (ODMs) were obtained from the particle of interest.
- The two smallest spatial frequencies (i.e. those closest to the transmitted beam) were chosen. The angle, ϕ , between these spatial frequency vectors,

a^* and b^* , was then measured.

- The frequency and angular data were then fed into a computer program which searched to find different combinations of a^* and b^* that matched those expected from an fcc crystal, e.g. {200}, {111}, {112}, {311}, etc.
- If any matches (the magnitude $|Na^* + Mb^*|$) were obtained they were evaluated to determine the proper zone orientation for an fcc crystal which would result in the original ODM.

Table 4.3 presents the results from the analysis of several HREM images. From the analysis, the desired zones of the spinel (γ) were simulated both as a function of thickness and focal series in order to determine whether a match existed between the calculated and experimental images. Faceting information was also used in the evaluation.

Table 4.3: Optical diffractogram analysis of ultrafine particles.

Figure #	$a^*(nm^{-1})$	$b^*(nm^{-1})$	$\phi(^{\circ})$	fcc matches	γ zone	image match?
4.11 (303)	1.28	1.56	90	{331}/{311} {420}/{313}	[136] [361]	no, [120] δ no
4.12 (311)	1.45	1.54	70	{420}/{111} {420}/{331}	[112] [123]	no yes
4.13 (334)	1.89	3.70	88	{420}/{331}	[136]	yes?
(360)	1.30	1.64	90	{311}/{331}	[103]	yes
4.15 (362)	1.64	2.13	92	{420}/{331} {420}/{313}	[123] [361]	no no
(367)	0.66	1.54	90	{331}/{200}	[013]	no, [011] δ

Figure 4.13 is an example of a possible θ -phase. As in Table 4.3, this particle may be interpreted as a spinel variant oriented along the [136] zone. However, the structure in the image can also be viewed as the [010] zone of the θ -phase. A through-focal series simulated image is shown in Figure 4.14 for the thicknesses of 4 and 10 nm. The agreement between the calculated and experimental images is reasonable. It should be

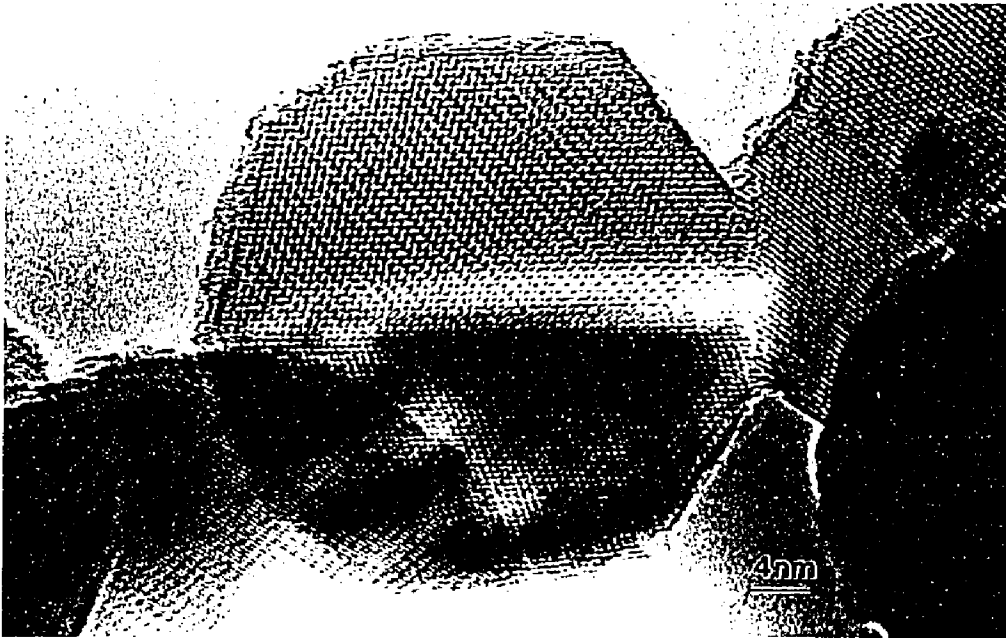


Figure 4.11 A particle of δ -alumina along $[120]$ is sintered to another particle on an irregular facet surface which corresponds to the reentrant surface of a twin, see §4.2.2.

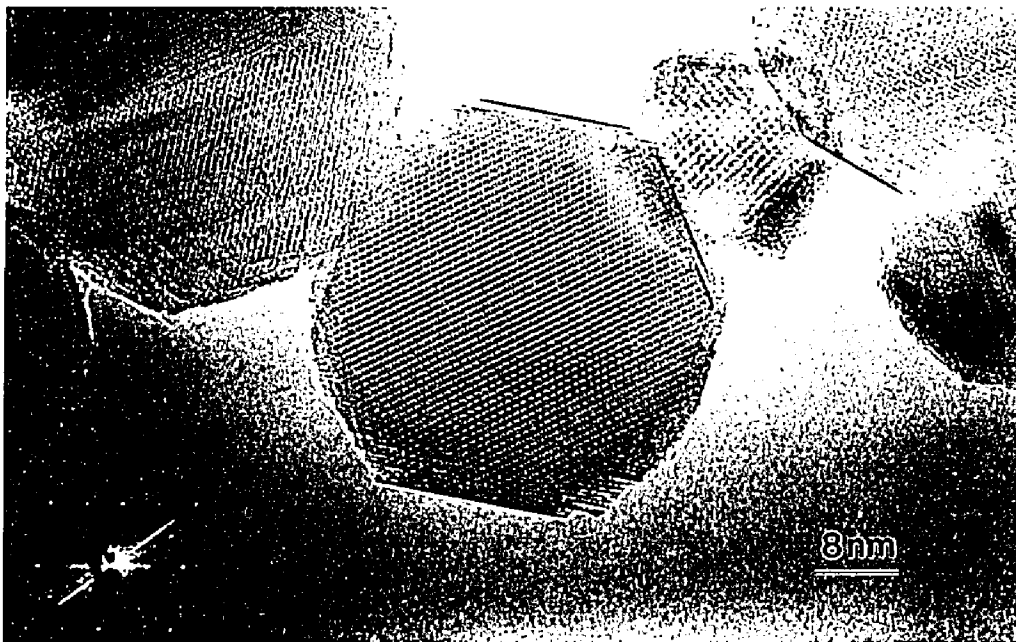


Figure 4.12 A sintered particle which is analyzed by the ODM method to be $[123]_{\gamma}$ orientation. The dark-line facets are identified as $\{111\}$ surfaces.

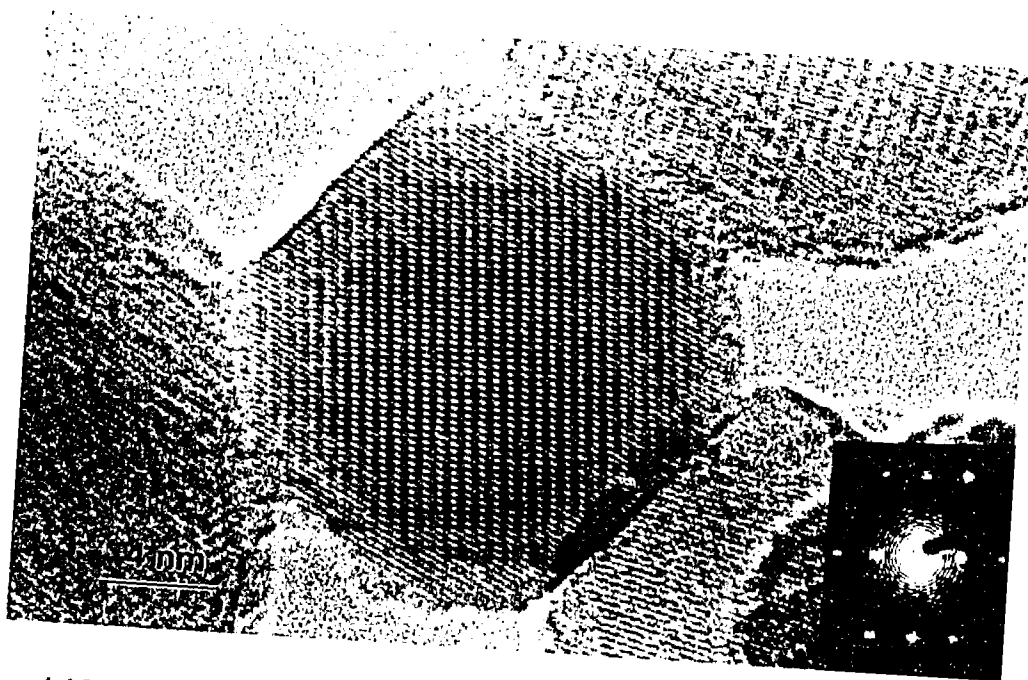
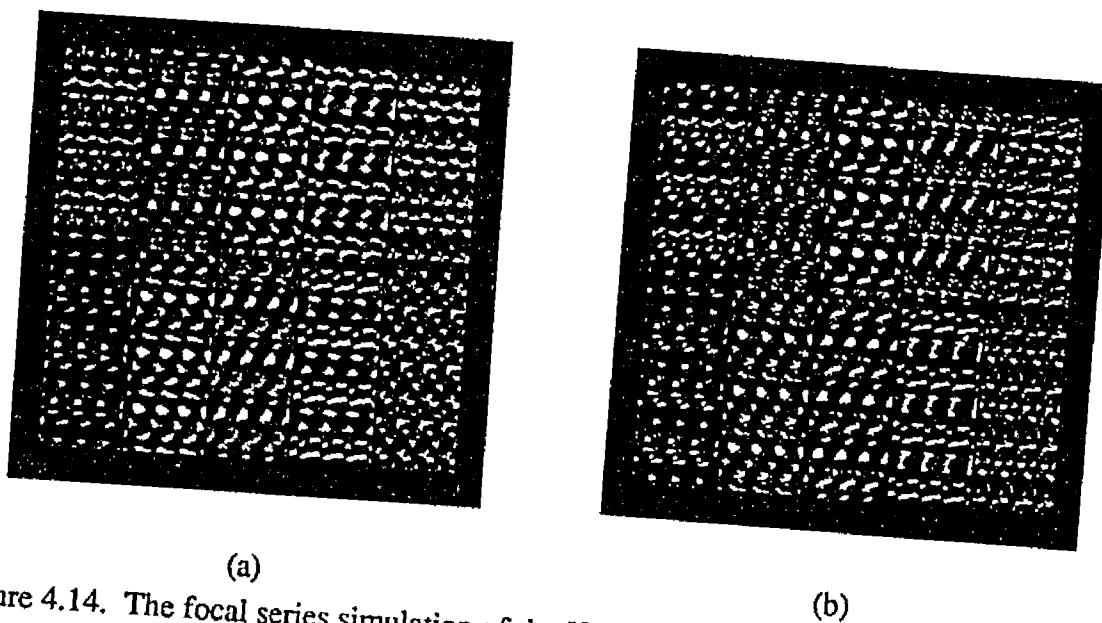


Figure 4.13 (#334-1) A particle of γ -alumina along $[136]$ according to the ODM analysis. The particle can also be identified as $[010]$ of the θ -phase which is monoclinic.



(a) (b)
Figure 4.14. The focal series simulation of the $[010]_{\theta}$ zone. The thickness correspond to 4 nm (a) and 10 nm (b) with lens defocus starting at -10 nm in steps of -10 nm.

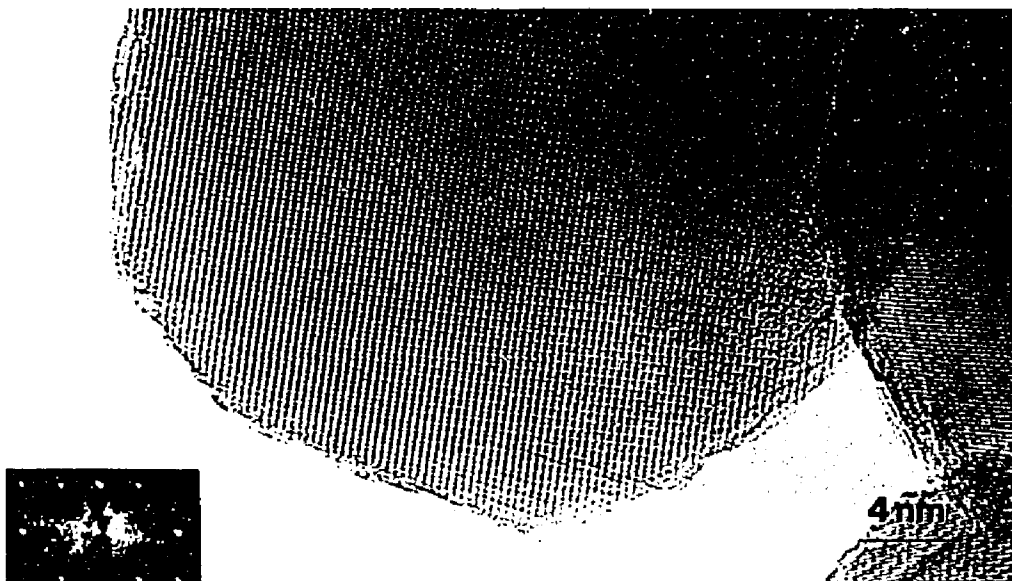


Figure 4.15. Particle which can be identified as either the $[123]_{\gamma}$ or $[361]_{\gamma}$ zones from the ODM analysis. However, there was no image match suggesting instead another phase.

noted though that the measured angles in the experimental image do not match those predicted from the θ -alumina cell parameters. In order to match both the structure of the image and the interplanar angles, new lattice parameters must be used; $a=1.09$ nm, $b=0.56$ nm, $c=0.27$ nm, $\beta=103.3^{\circ}$. These new parameters are unlike those previously reported. However, they are not so dissimilar that the differences, say with the θ -alumina of Stumpf, can not be accounted for by small distortions in the lattice, as have been noted earlier.

An interesting feature in these UFPs is the striking similarity of particle shapes even between those of different phases. This result raises the question of how does the phase transformation of alumina occur without inducing a subsequent change in the Wulff polyhedra. Consider the case of the γ to δ transformation where the ordering process occurs on tetrahedral sites leaving the octahedral sites unchanged. Practically, we can envision the process as simply an increase in the occupancy of the specific tetrahedral sites resulting in an altered symmetry but no long-range diffusion, e.g. Figure 4.16. The result is that no macroscopic shape change is required to achieve complete phase transformation, suggesting that facet formation is strongly controlled by octahedral, not tetrahedral, sites.

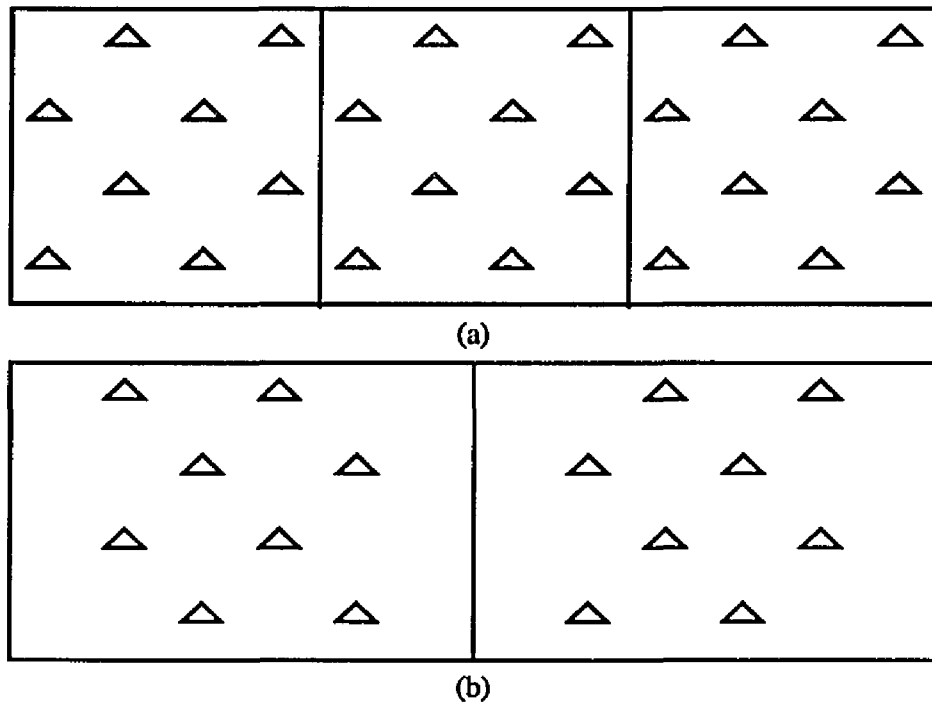


Figure 4.16. Schematic representation of an ordering process leading to a change in symmetry and lattice parameters, but not a macroscopic shape change. In (a) the initial γ -phase transforms to δ -alumina (b). The triangles are typical tetrahedral sites, [100] zone.



Figure 4.17. Two 'spherical' particles have sintered with a small neck, no densification.

§4.2.2 Sintering Process

Once the UFPs have been structurally characterized, we may then turn our attention to the process of sintering in the UFPs. There are three controllable variables in this sintering study; the particle size, the sintering temperature, and the sintering time (the residence time of particles within the furnace). For further information on the relationships between the pressure, temperature, and flow rate the reader is referred to the dissertation of Mao-Hua Teng (1991). In order to elucidate the general sintering trends, the sintering times and temperatures were varied, holding the particle size distribution constant.

§4.2.2.1 Sintering at Low Temperatures

Figure 4.17 shows two particles which have sintered together under conditions of 1000°C and a dwell time of 0.10 seconds. It is apparent that these particles have undergone initial stage sintering with only a small neck formed and there is no measurable densification. Furthermore, the neck region can not be characterized as having a radius of curvature in the macroscopic sense, appearing instead to have a discrete contact angle. Figure 4.12 is an example of the random manner in which the UFPs adhere and sinter to each other. The particle, [120]_δ orientation, has a well defined facet structure and yet it has sintered along an irregular surface corresponding to the reentrant surface of its twin. The resultant neck/grain boundary is atomically rough.

The UFPs form long chains before entering the furnace to sinter; Figure 4.18 illustrates the results. Here, three of a many-particle chain have been imaged revealing atomically rough neck regions along specific facets and discrete contact angles. In addition, it is clearly evident that the particles have adhered to each other and sintered with no apparent 'reorientation' of the sintered particles to form low energy interfaces. This result indicates that surface diffusion is sufficiently fast that the initial contact orientation is

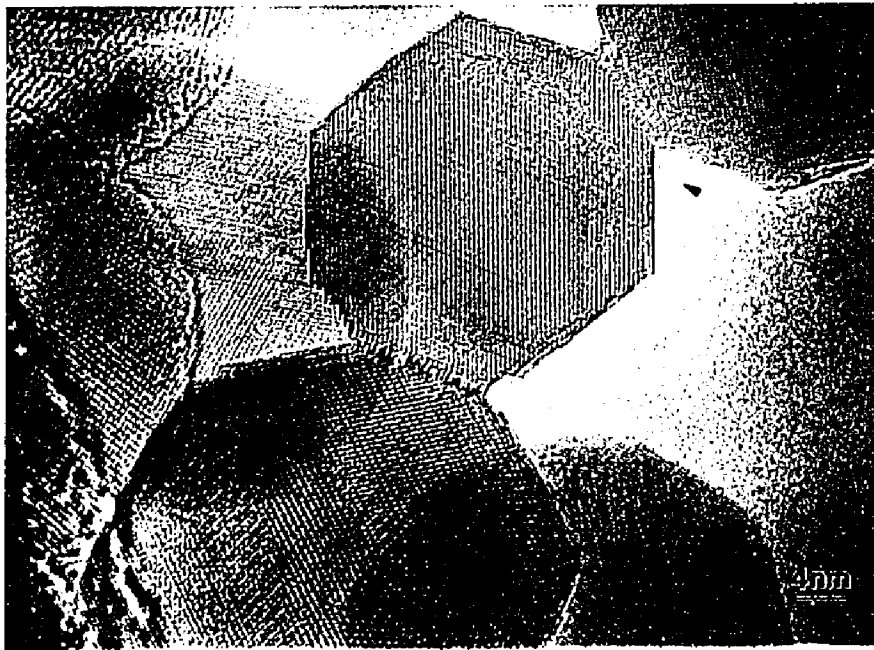
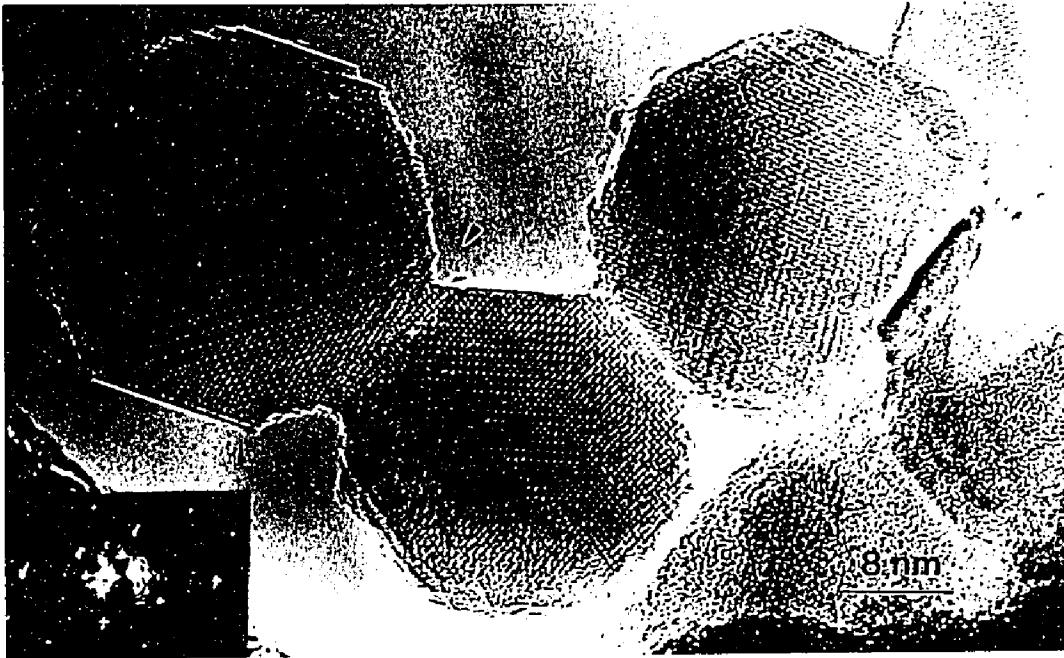


Figure 4.18. Chains of sintered particles. Here the particles have adhered with no apparent reorientation as arrowed in (a). In (b) note the distorted Wulff shape, arrowed.

'locked-in' before significant neck growth occurs.

An apparent contradiction of this argument can be found in Figure 4.19 where two particles have sintered. Here, instead of a seemingly random orientation, the two particles appear to have a high degree of coherency corresponding to the $\{311\}_\gamma$ planes. These planes have an approximately 5° misorientation which leads to a low angle grain boundary. It may be speculated that since the particles do not have the well-defined facets as in previous examples, and appear more spherical, that the particles were able to 'roll around' on their surfaces until this orientation was achieved.

Figures 4.20, 4.21 and 4.22 illustrate the sintering results when the flow rate is slowed to give a dwell time of 0.27 seconds at 1000°C . In the case of 4.20 and 4.21, the sintering process is definitely confined to the $\{111\}$ facets for *all* sintered particles and the contact angles in the neck have remained discrete despite the longer sintering time. One notable feature in 4.21 is that the sintered particles appear to have a neck region which is clearly discernable from the particles themselves. Normally, one would expect that as the particles sinter, they would approach each other as in the center-to-center approach in traditional sintering. One must note, however, that the particles are not free to approach each other as they are constrained by a third particle to which they are attached. Though the inference is indirect, Occum's razor would dictate the assumption that if the two particles have sintered to each other, it is reasonable to expect them to also be sintered to the third particle. Figure 4.22 is an example of sintering occurring in a many particle system where the particles have fully developed neck structure. In this case, the extensive innerconnectivity between the particles has prevented substantial consolidation, for example the five particle pore as shown.

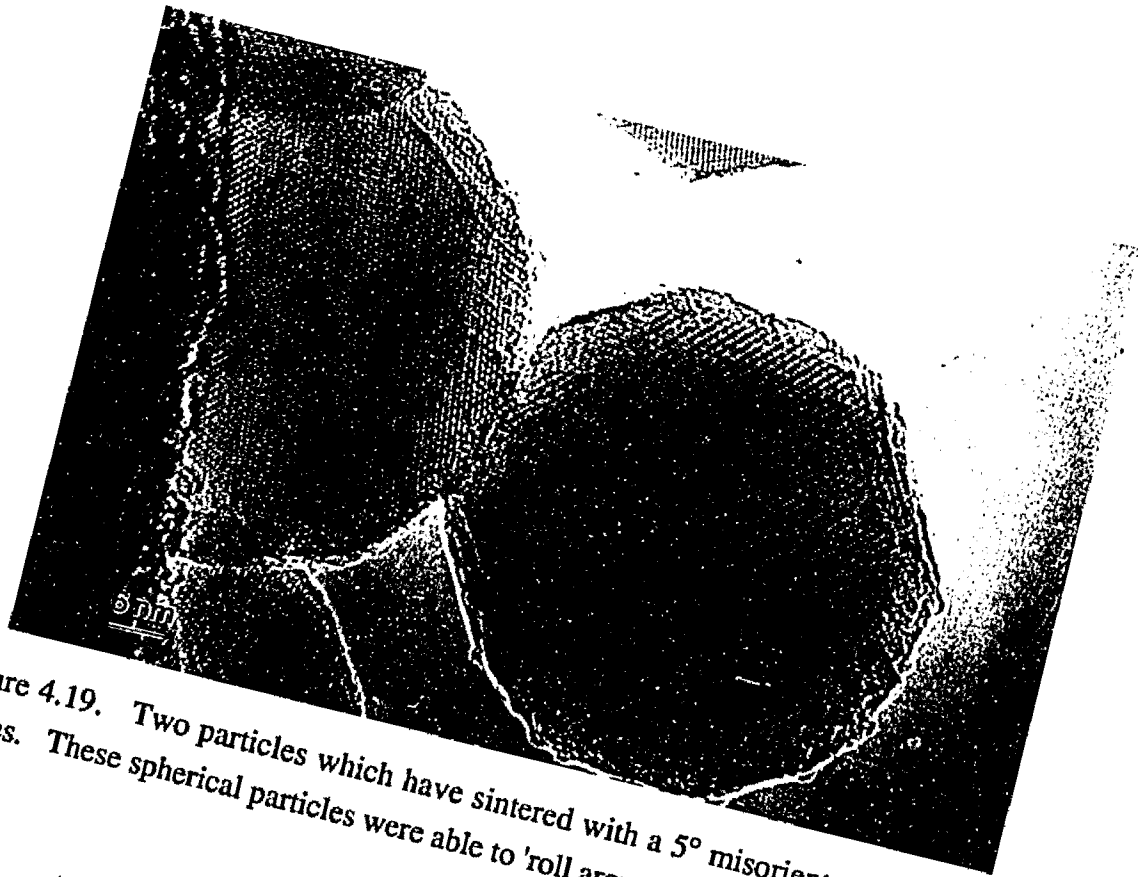


Figure 4.19. Two particles which have sintered with a 5° misorientation of their $\{311\}$ planes. These spherical particles were able to 'roll around' to achieve this orientation.

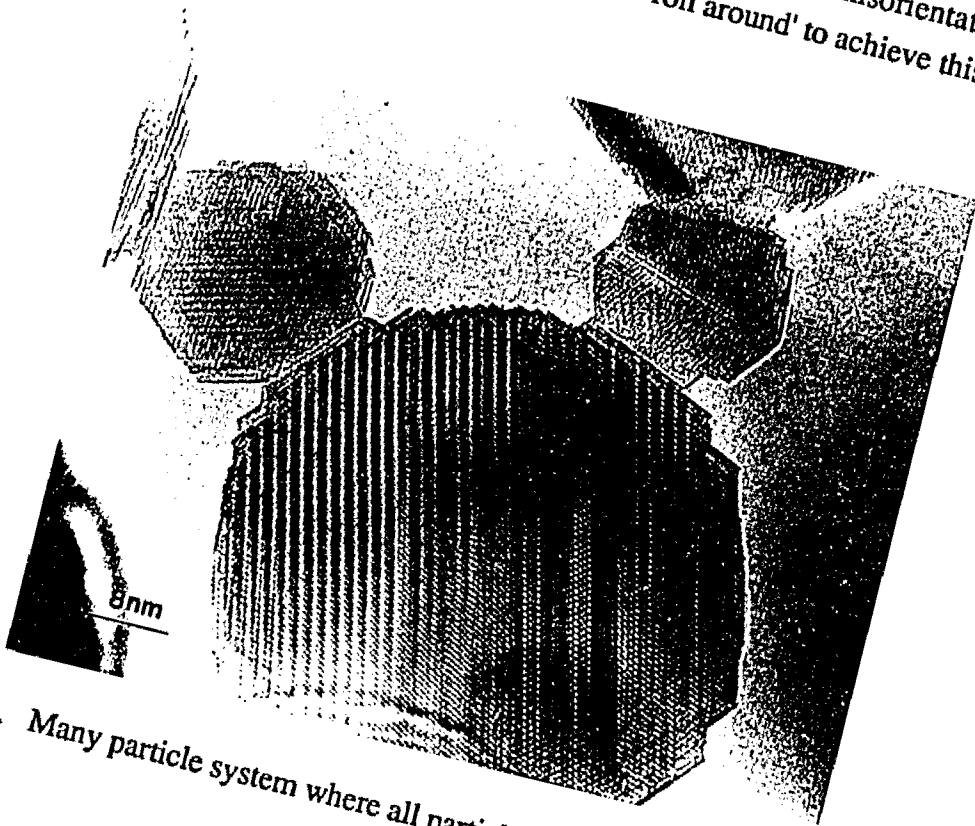


Figure 4.20. Many particle system where all particles have sintered on their $\{111\}$ facets.

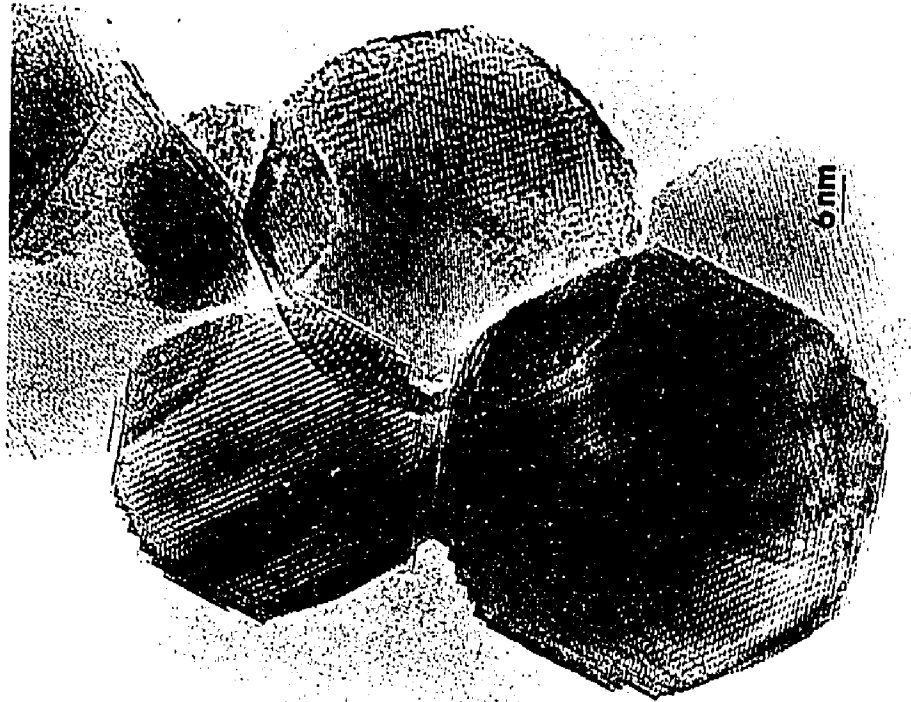


Figure 4.21. Two particles which have sintered to a third particle. The grain boundary region is distinct from the two particles.

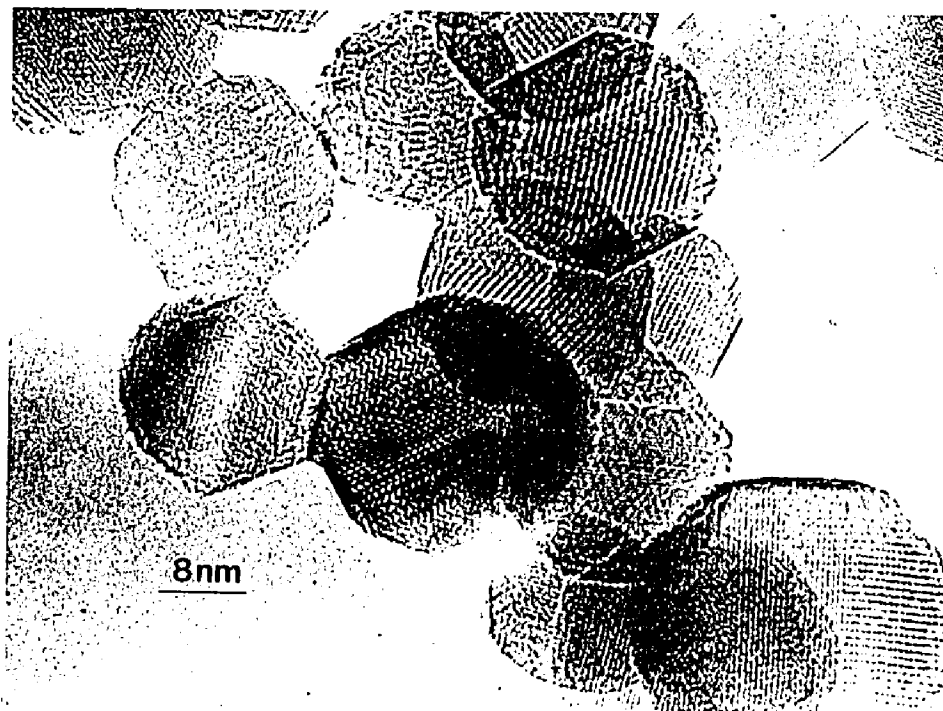


Figure 4.22. Many particles which have sintered and are constrained from densifying.

§4.2.2.2 Sintering at High Temperatures

When the temperature of sintering is increased to 1200°C, keeping the sintering times and particle size constant, the processes discussed above are accelerated. Consider Figure 4.23 where four particles have sintered together. Consistent with earlier examples, the sintering has occurred on well-defined facets with discrete contact angles. However, the attention must be focused on the arrowed particle which appears to have undergone substantial grain growth as indicated by the heavy lines in the scanned representation. Furthermore, the neck region as a result of this grain growth has considerably different contrast than either sintered particle. This result lends credence to the notion that there exists a distinct grain boundary region which has no direct structural relationship to either sintered particle, though it may be compositionally identical.

§4.2.2.3 Bright-field / Dark-field Analysis

The dark-field analysis of these samples revealed that there is little strain induced by the contact between sintered particles, see Figures 4.24 and 4.25. Instead, the stress due to adhesion seems to be accommodated by considerable internal faulting within the particles. These results are in contrast with those of Tholen (1979, etc.) where significant strain fields occurred during adhesion in small metallic particles. Whereas the metal particles are able to plastically deform in response to the contact stress, the ceramic particles can not alleviate the stress in this fashion and instead internally fault. These results, however, are consistent with those of Marks (1985b) where it was noted that virtually all of the strains evident in small metal particles were inhomogeneous in nature and that the strains induced the formation of multiply-twinned particles (MTPs). One should also note in the bright-field images the considerable surface roughening as a consequence of long (20 minutes) doses of low flux electron irradiation necessary for BF/DF work.

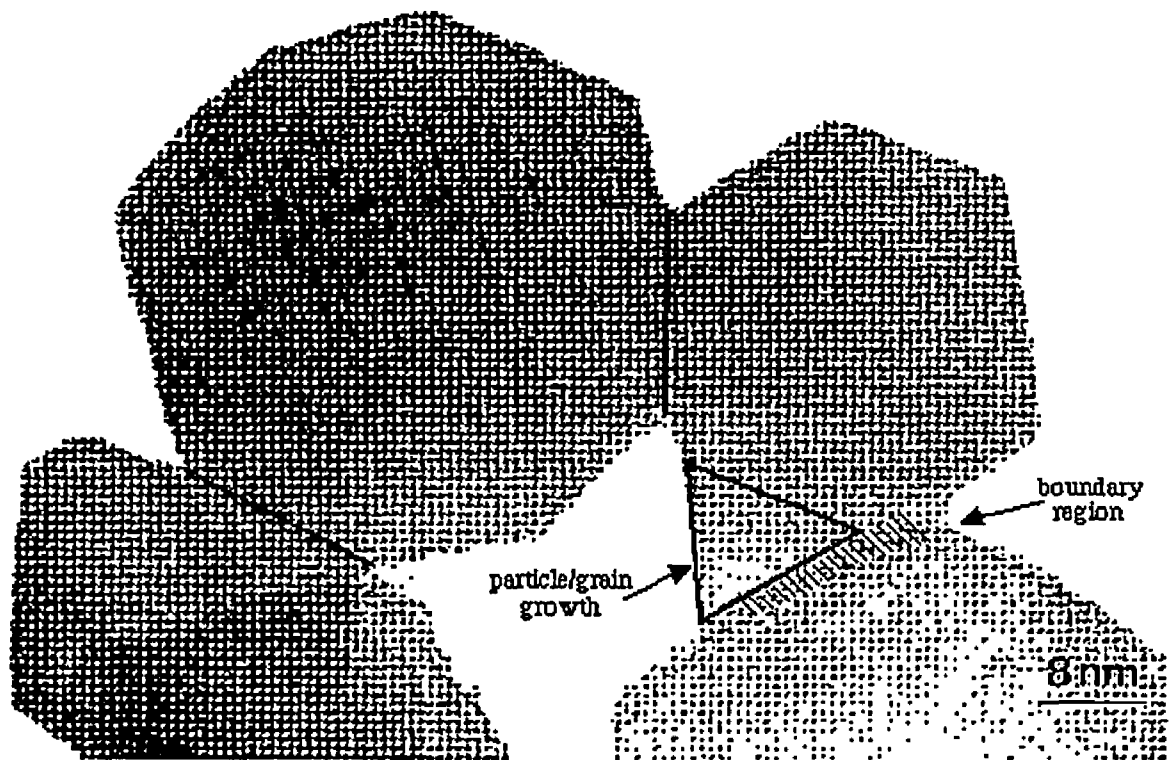


Figure 4.23. Many particle system where all particles have sintered at 1200°C . The arrowed particle has experienced particle/grain growth and has a quite distinct grain boundary region. A scanned representation of the particles is shown in (b).

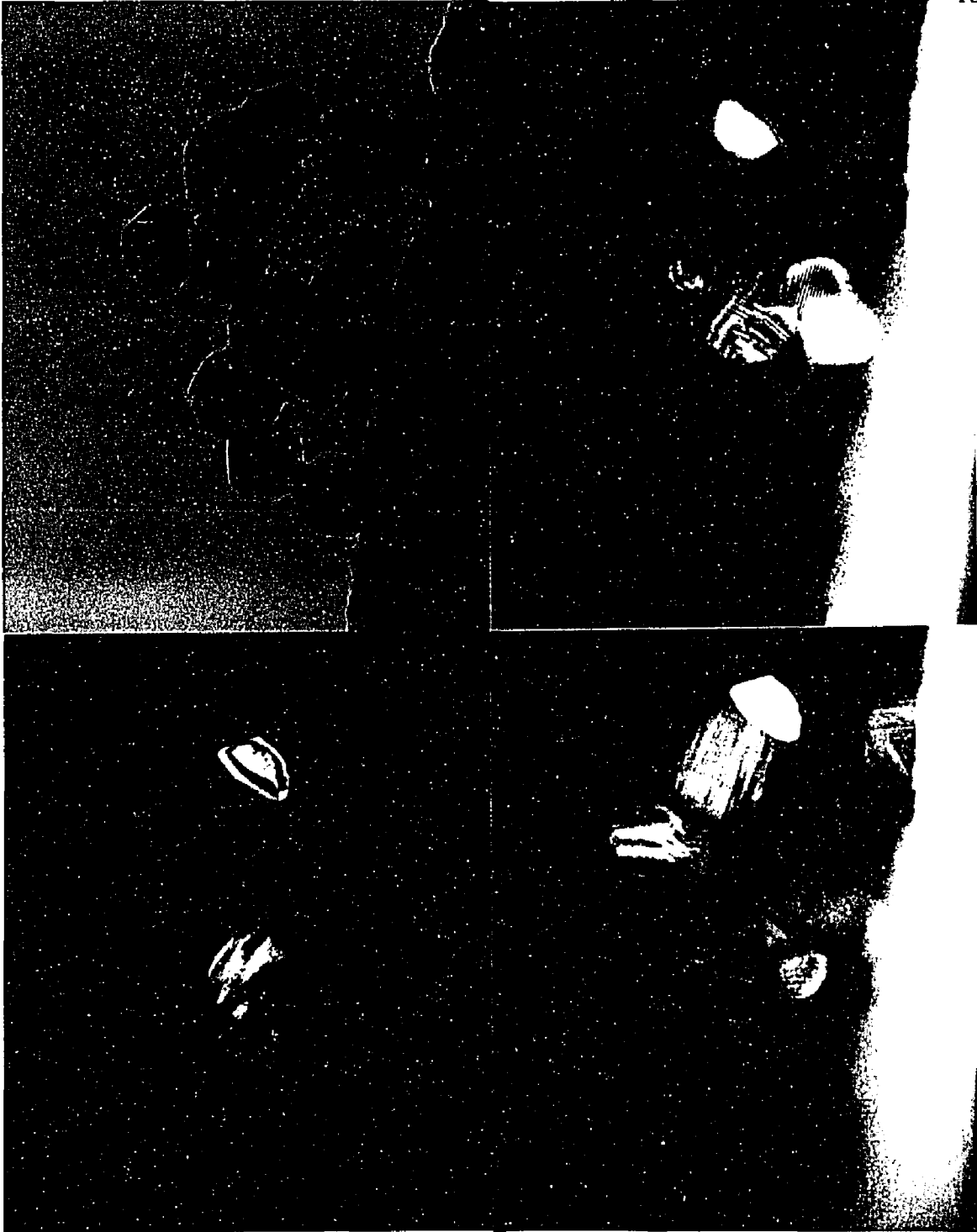


Figure 4.24. Bright field/dark field montage of sintered particles. The particles show a high degree of internal faulting and twinning as a result of particle adhesion. The scale of the images is $1.2 \text{ cm} = 40 \text{ nm}$.

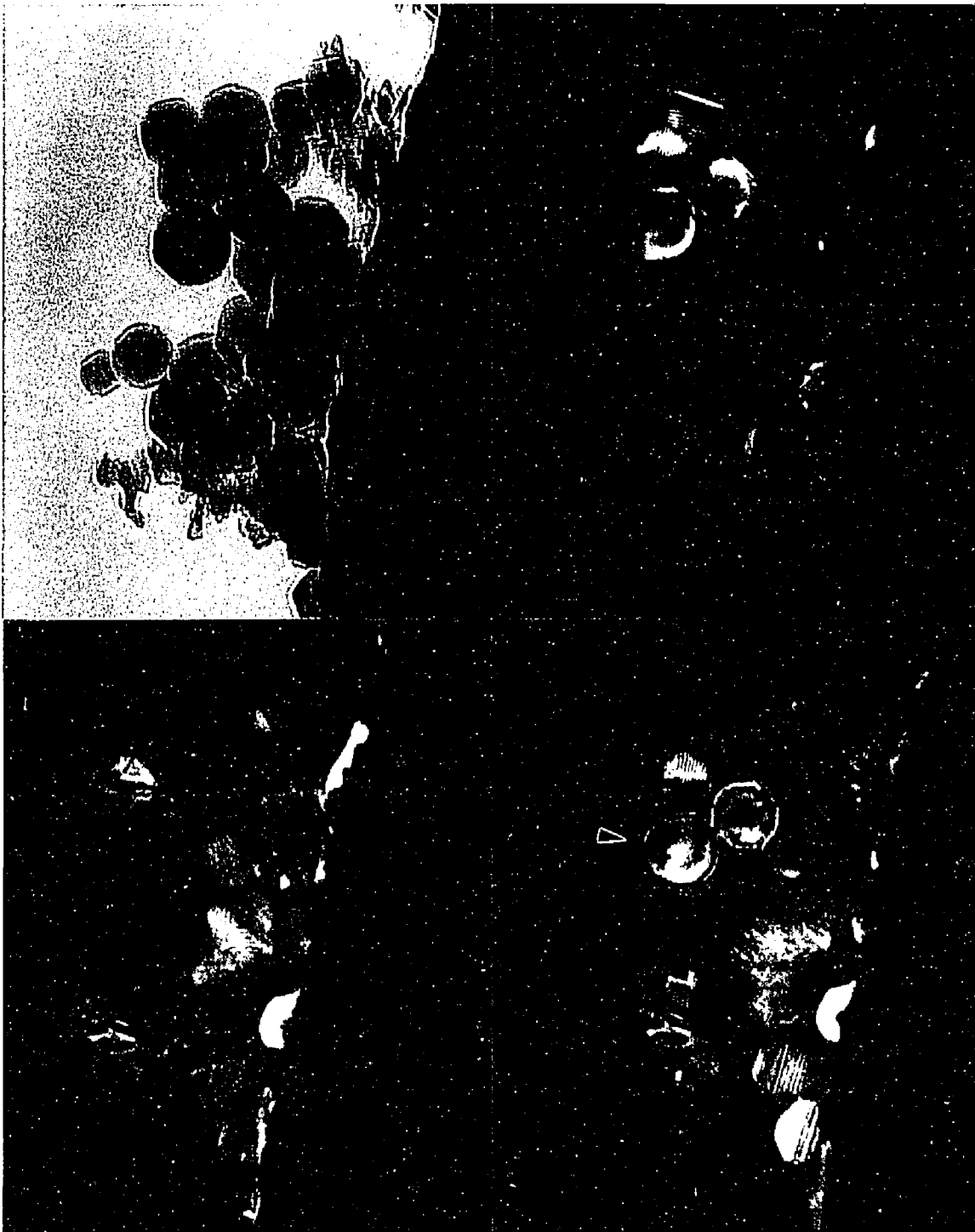


Figure 4.25. Bright field/dark field montage of sintered particles. Again the particles have internally faulted in response to the adhesion stress. Arrowed particles show indications inhomogeneous strains as a consequence of sintering together. Scale: 1.2 μm = 40 nm.

§4.2.2.4 Phase Transformations

The UFPs entering the furnace traverse a temperature profile which, in addition to promoting sintering and neck growth, can lead to phase transformations, e.g. γ to δ . Consider, for example, Figure 4.26 where a particle has sintered to a smaller particle. If one traces the general outline of each particle shape, then one would expect to find the grain boundary in between them. Instead, the 'interface' between the particles appears to be completely commensurate and the grain boundary has moved up into the smaller particle. An interpretation of this result is that the particles entered the furnace with the γ structure and have undergone a phase transformation to the δ -phase. Consequently, the grain boundary has migrated into the smaller particle in order to reduce overall interfacial energy. One might speculate that given sufficient time, the grain boundary would have completely migrated through the particle leaving a single grain in the shape of the original two particles.

Conversely, one might interpret figure 4.26 as being the result of only grain boundary migration without the need to invoke a phase transformation. Consider the case of two adhered δ -phase particles. If the smaller particle had such a high degree of structural misorientation relative to the larger particle that, as a result of the elevated sintering temperatures, the larger particles' grain boundary nucleated grain growth in the smaller particle so as to regrow it in an epitaxial fashion. This would then explain why one side of the small particle appears 'amorphous' in structure; it is simply so misoriented that no structural periodicities are imaged.

Figure 4.27 is an excellent example of grain boundary migration. Here, two particles underwent a phase transformation (or just GB migration) with the result that the final crystal is simply one grain in the shape of the original two particles. The interface appears to be commensurate with respect to the $\{400\}$ lattice planes in the structure. In

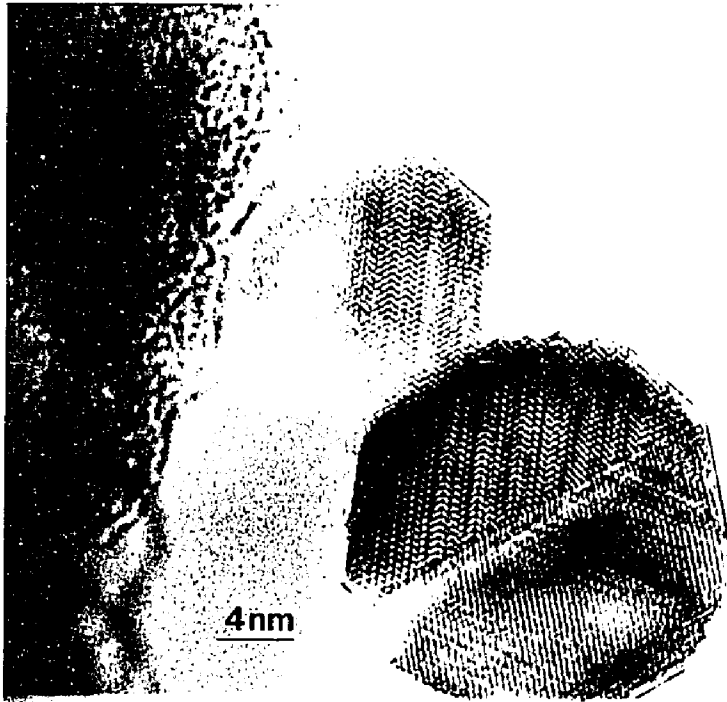


Figure 4.26. Two sintered particles that have undergone a transformation to the δ -phase. The smaller particle has grown epitaxially with the larger particle, oriented along $[102]_{\delta}$. The grain boundary is now inside the smaller particle.



Figure 4.27. Two particles which have no grain boundary between them, resulting in a single crystal in the shape of the original two. The particles are coherent along the $\{400\}_{\delta}$.

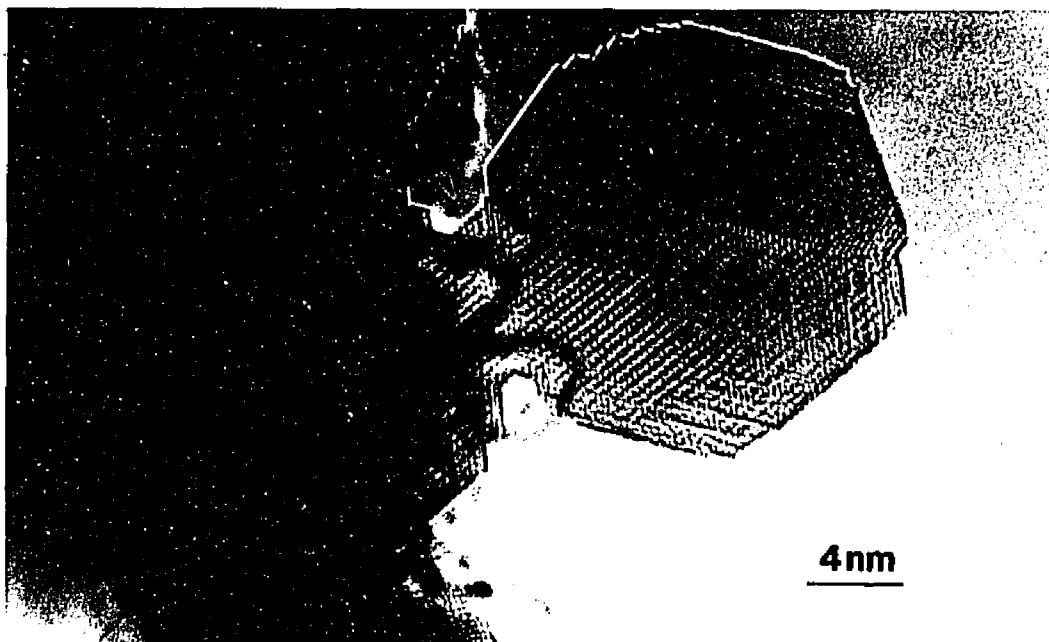


Figure 4.28. Two sintered particles of the γ -phase. The neck is sharply faceted and has a discrete contact angle. The particles seem to have phase transformed into one particle, however closer examination reveals that the $\{311\}$ planes in the right particle do not cross the grain boundary which also appears distinctly. Note the neck surface has reconstructed.

addition, the particles appear to have experienced considerable neck growth. This may be the result of either true neck growth or, more likely, the effects of surface energetics to 'straighten out' the cusped regions of the original neck shape, similar to sub-grain coalescence (Reed-Hill, 1973).

Figure 4.28 illustrates the existence of statistical anomalies in the sintering of UFPs. Here two twinned γ -alumina particles have sintered along their {111} facets and, in doing so, appear to have oriented themselves so as to achieve a high degree of coherency across the interface. Such a reorientation is not favored simply because surface diffusion should be sufficiently fast enough to 'lock-in' the initial adhesion orientation. The probability of two particles just adhering and sintering in this orientation is quite low. However, the two particles are clearly distinct (i.e. no grain growth) as indicated by the termination of the {311} lattice planes at the grain boundary. Furthermore the reconstructed neck region, arrowed, has a different thickness contrast from the 'bulk' suggesting that there exists a slight height difference between the sintered particles.

§4.2.3 Role of Faceting

Virtually every particle that forms from the arc discharge has a high degree of faceting due to the particle shape conforming to its Wulff construction. Consequently, one expects the presence of these facets to greatly control the sintering behavior of the UFPs, and this is indeed the case. The analysis of the faceting structure reveals that it is more probable for sintering to occur on those facets which represent the close-packed planes of the spinel phases. If we assume, for the sake of simplicity, that all particles analyzed have the spinel structure (neglect the θ -phase) and furthermore consider the δ -alumina Wulff construction to be isomorphic with that of γ -alumina, then we can classify all UFP facets entirely in terms of the γ -alumina Wulff polyhedra which is isomorphic with that expected from an fcc crystal. Thus the Wulff polyhedra will be comprised of eight {111}, six

{200} and twelve {220} facets. We also remember that the {220} are unstable and decompose into {111} microfacets, but again will be treated as locally flat. The analysis of the sintering with respect to the facets yields;

Table 4.4: Ultrafine particle sintering by facet structure.

<u>{111}/{111}</u>	<u>{111}/{200}</u>	<u>{111}/{220}</u>	<u>{200}/{200}</u>	<u>{200}/{220}</u>	<u>{220}/{220}</u>
18	5	5	9	-	-

where sintering purely on {111} facets has the highest probability, followed by that of a purely {200} facet structure. We also see that the probability of sintering with mixed facet structure is equally great with the caveat that the mixed facet sintering seems to prefer a {111} facet. No evidence was found to support the sintering of pure {220} facets, though this certainly does not preclude their existence, just their probability. Of course, there also exists evidence of sintering in UFPs where no facet structure can readily be applied, they have been neglected in this analysis.

§4.2.4 Electron Spectroscopies

While HREM is extremely useful to determine the atomic structure of the UFPs, their chemical structure must also be examined. The primary instrument used to investigate the chemical nature of the sintered specimens was a parallel electron energy loss spectroscopy (PEELS) situated on the UHV-HREM (see Figures 4.29 and 4.30). The results from the PEELS data indicate that there are no substantial metallic impurities contained within the particles. Such impurities could come a number of sources, most notably those in the aluminum electrode material. That no such impurities were detected demonstrates that the particle formation and particle sintering processes are largely contamination-free and that the behaviors observed are not artifactual. Furthermore, from the structure of the loss spectra it is clear that the oxygen bonding environment, as

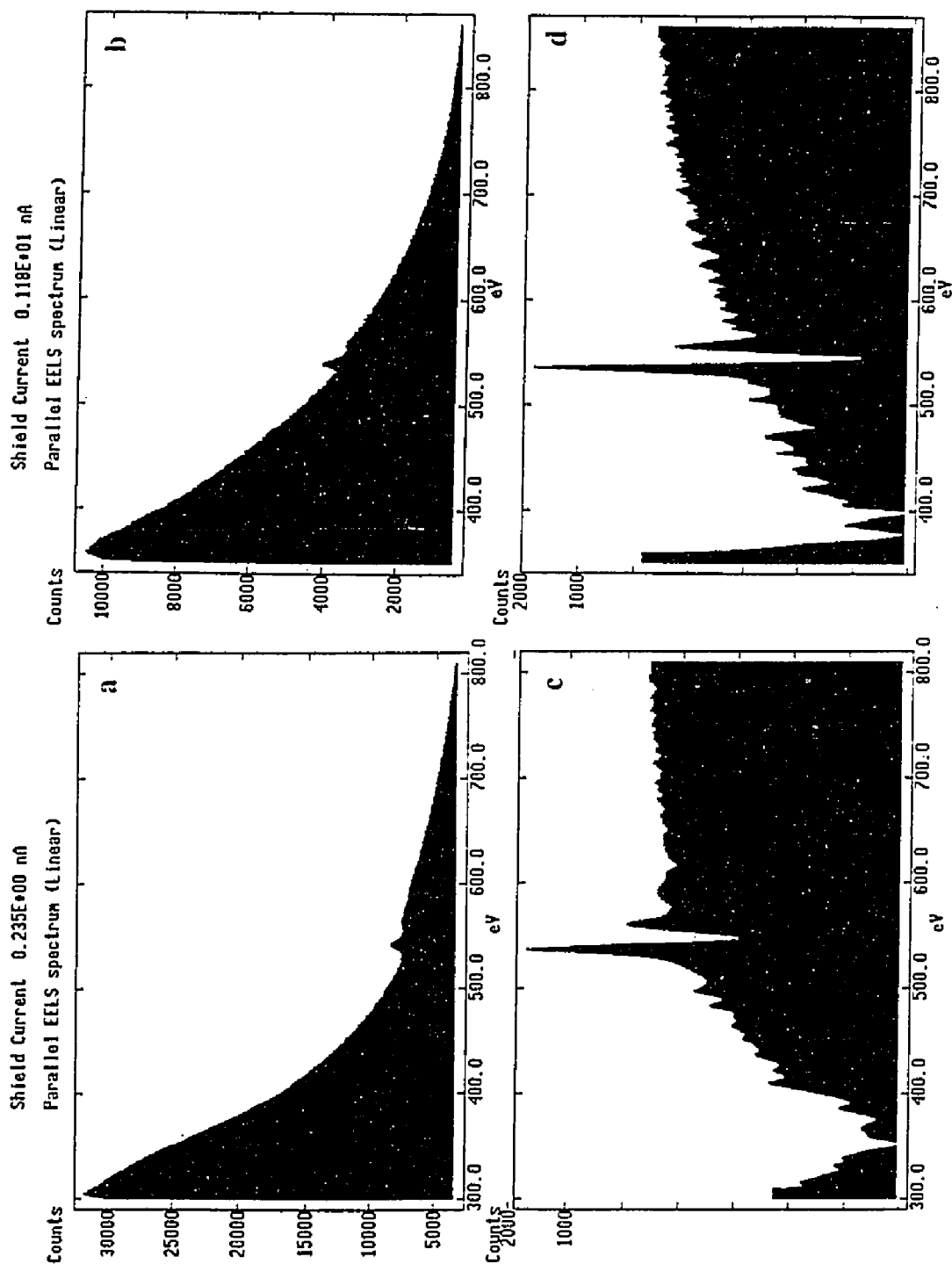


Figure 4.29. PEELS of alumina of the oxygen K-edge from the UHV (a) and HF2000 (b) microscopes. Their respective first derivative spectra are shown in (c) and (d).

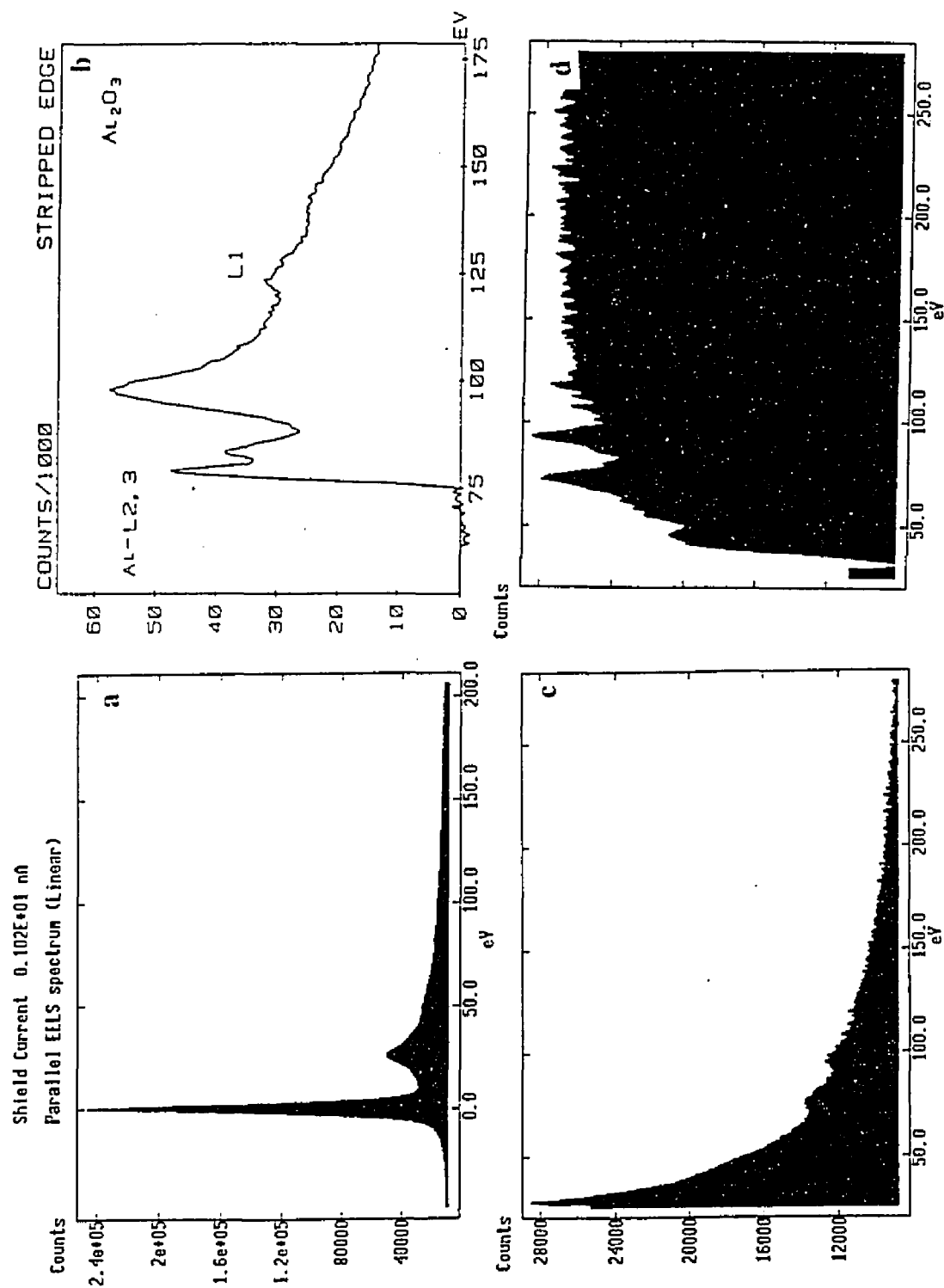


Figure 4.30. Alumina PEELS from the UHV microscope. The zero loss and plasmon peaks (a), the Al L_{2,3} stripped edge [from EELS Atlas 1983] (b), the Al L_{2,3} (c) and its first derivative in (d).

determined from its K-edge, is quite similar to that observed in α -alumina. Such a result is understandable in view of the fact that the transformation of γ to α -alumina can be viewed in terms of an ordering process of primarily the aluminum cations. The loss spectra due to aluminum (L2,3) also indicated that its chemical environment in the UFPs is highly similar to that in α -alumina. This result suggests that the chemical environment of the aluminum cations is either virtually identical to that of α -alumina, or that the sensitivity of the PEELS data is more greatly influenced by the aluminum in octahedral sites as opposed to the tetrahedral sites.

In order to obtain better signal-to-noise spectra, unsintered specimens were examined in the HF2000 with the result that both the oxygen K-edge and aluminum L2,3 spectra were similar to those obtained in the UHV-H9000. Under continued electron irradiation, there were indications of a metallic character to the aluminum loss spectra. For further information on this aspect, the reader is referred to Appendix One.

The sintering behavior of the UFPs is greatly controlled by their surfaces. And whereas PEELS provides information about the chemistry of the bulk, the technique is relatively insensitive to surfaces. That is, PEELS is unable to detect the presence of less than a few monolayers of contamination (e.g. carbon) from a surface. A suitable technique to examine the surface chemistry of UFPs is Auger electron spectroscopy (AES). While the initial proposal specified the use of AES to investigate the sintered specimens, the spectrometer has not been available to perform these experiments. The lack of an AES study is certainly a drawback, though not fatal, and future goals should make more effective use of the technique to examine such phenomena as segregation of dopant materials.

§4.3 Discussion of Results

In this study, the sintering of ultrafine particles has had dramatically different behavior than the micrometer-sized particles used in traditional sintering models (e.g. Johnson 1969). These traditional models require the assumptions of large 'spherical' particles with isotropic surface energy and a chemical potential driving force defined in terms of the neck / particle curvature difference; these models are expected to break down in the case of UFPs where surface properties predominate.

The UFPs have well-defined surface facets which determine the final sintering geometry, thus making surface *energy* considerations, which are necessarily anisotropic, preponderant. In addition, these surface facets result in neck formation which is, even on the atomic level, abrupt having no readily defined radius of curvature. Furthermore, it is likely that the mass transport mechanism which governs the sintering process is surface diffusion. In other words, one would expect surface diffusion to be the "short-circuit" diffusion path in UFP systems, allowing it to dominate over volume and grain boundary mechanisms. Furthermore, one would not expect significant contributions to mass transport from volume and grain boundary diffusion due to particle size and kinetic effects. Thus, while this study has no direct measurement of diffusion coefficients of any type, it is not unreasonable to conclude that surface diffusion is the predominant mechanism.

Given that the UFPs are out of the range of applicability of traditional sintering models, a different approach must be taken; one that treats the sintering process on the atomic scale. A treatment which seems plausible is to consider the sintering process as the following sequence of steps;

- The arc discharged particles form well-defined facets according to the Wulff construction.
- The particles randomly adhere together in the form of chains, these particles

then enter the furnace.

- The chain orientation is 'locked-in' by surface diffusion which is activated as the particles traverse the temperature ramp to the sintering temperature.
- The UFP chains enter the sintering temperature zone where surface diffusion is the predominant mass transport mechanism.
- The sintered UFPs exit the furnace where the room temperature specimen cartridge quenches the sintering process.

The third step is clearly most important for modeling the initial stages of the sintering process. The question then becomes how to model surface diffusion without having to invoke isotropic surface energy or diffusion coefficients (Nichols 1966). An appropriate treatment may be found by drawing an analogy to crystal growth from the melt by the mechanism of lateral growth on surfaces. Consider for example, three ways to achieve growth on surfaces; surface nucleation due to arriving atoms (i.e. evaporation-condensation), spiral growth due to interfacial steps (those supplied by screw dislocations), and growth from twin boundaries (Porter and Easterling 1981). We can neglect the contribution from surface nucleation because there already thermally activated atoms on the surface which are diffusing. Then we can confine our attention to the spiral and twin growth mechanisms which have similar behavior.

The gist of the model is that when surface diffusion is activated, atoms on the surface have a high degree of mobility and thus mass transport is rapid. Atoms move about on the facets of the UFPs which can be considered as atomically smooth terraces. These 'skating' atoms have, in a simplistic treatment, four dangling bonds which is energetically unfavorable. Those atoms which happen upon the interface between the UFPs will be energetically driven to the interface in order to reduce their dangling bonds, or, identically, increase their coordination number. Thus the fluxes of atoms about the

surfaces of the UFPs is determined by a coordination number gradient where those atoms in the neck region sit in a potential well; a higher binding energy. Also consider that facets such as the {220} represent ideal growth sites being comprised of {111} microfacets where kinks and jogs are easily found, see for example Figure 4.28.

Searcy (1985) treated the case of aggregates of particles with anisotropic surface energies. These particles were considered to be unstable to shape changes for which

$$\delta G = [\Sigma(\sigma_i A_i + \gamma_i h_i)] < 0 \quad (4.7)$$

where δG is the differential change in the Gibbs free energy, $\sigma_i A_i$ the free energy of the surface or interface i , and $\gamma_i h_i$ the free energy of edge, ledge, or other defect i . Searcy further stipulated that the free energies of the defects be ranked as edge \geq ledge \geq surface \geq grain boundary \geq dislocation. Searcy's approach predicts that during sintering, the difference in chemical potential between facet surfaces and the neck region is the driving force for the flux of atoms.

An additional example of this atom flux may be found in Figure 4.18 (a) where the particle in the middle appears to have 'lost' mass on its far side. This would be the result of diffusion away from the far side to the neck regions with the other two particles. Similar results were observed by Warble (1985) who interpreted the image contrast in the sintering / transformation of γ - to α -alumina as proceeding by "waves of material diffusing across the surface."

An alternative way to view the sintering of the UFPs is by means of the Wulff construction, see Figure 4.31. Earlier, it was noted that the Wulff construction for the case of multiply-twinned particles had the constraint that the facet surfaces on the twin boundary had to exactly match in order to perform the mathematical cut operation (Marks, 1985c). The grain boundary between two UFPs can also be considered as an internal

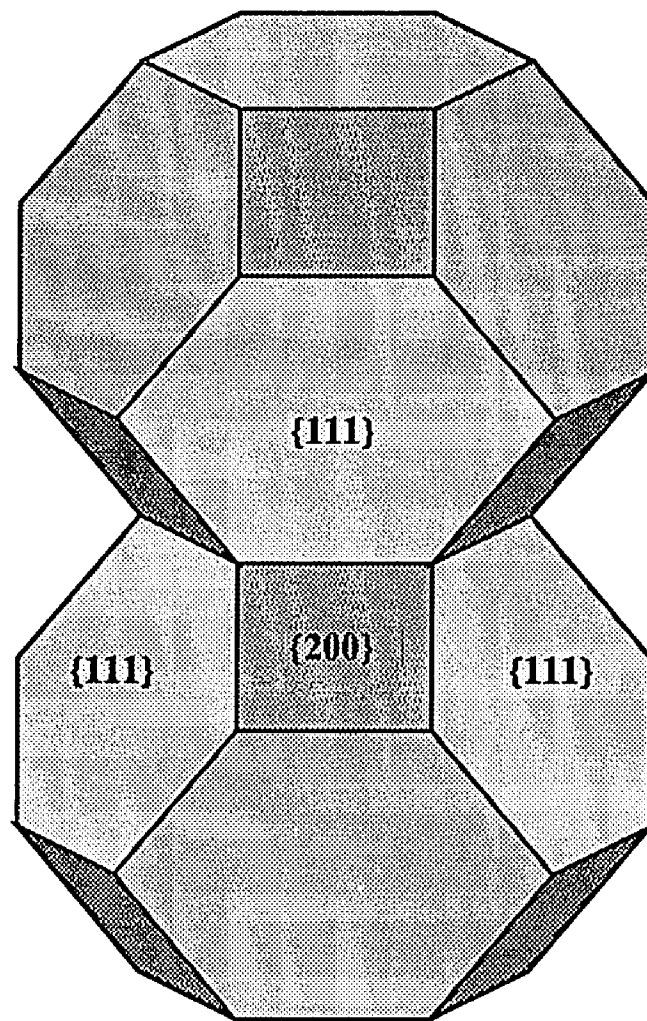


Figure 4.31. Two faceted ultrafine particles which have sintered on common $\{111\}$ facets but with mixed edge character. In this case densification, as defined by center-to-center approach, is constrained by the Wulff construction. In order for the Wulff centers of the particles to approach, the grain boundary must grow in area. That is, the $\{111\}$ facets must grow at the expense of the $\{200\}$ facets. However in this situation, a shrinking $\{200\}$ facet (labeled) will necessarily cause distortions in the adjacent $\{111\}$ facets. Distorting the Wulff construction is energetically unfavorable and thus no densification occurs. In the presence of an applied stress, or higher temperatures, the energetic barriers to densification may be overcome.

boundary of a single crystal, e.g. a disclination. We can then model the center-to-center approach of the two UFPs (densification) as the motion of a disclination through a single crystal. The calculations of Ajayan (1989, 45) indicate that there exist cusps, or local minima, in the energy of the particles as a function of the disclination position. These cusps are associated with activation barriers which correspond to the energy cost necessary to move the disclination. Extending this behavior to UFPs suggests that an energy barrier may exist to center-to-center approach, or densification. That is, the densification process would necessarily cause distortions in the Wulff polyhedra (in order for the facet boundaries to match) and that the driving force for densification is not sufficient to overcome the energy costs of these distortions. This would explain the apparent lack of densification in the sintering of the UFPs. Of course, an external force applied to the sintering particles, either temperature or pressure, could provide the necessary energy for the densification process to proceed.

Clearly, phase transformations in the UFPs are a concurrent process which have an effect of the sintering behavior. The effects of phase transformations with grain boundary motion have long been noted in the sintering literature. For the case of iron, Shingu (1967) sintered 12 μm spheres of $\alpha\text{-Fe}$ at 962°C for 1182 minutes with the result that the $\alpha\text{-}$ to $\gamma\text{-Fe}$ phase transformation occurred in the sintered compact. In sintering of $\alpha\text{-Fe}$, the GBs remained confined to the neck region between the two spheres. The driving force of the transformation to $\gamma\text{-Fe}$, however, caused the GBs to migrate freely through the compact so as to bear no relationship to the initial $\alpha\text{-Fe}$ boundaries. Since the presence of the GB between sintering spheres is required to achieve shrinkage, the results of GB motion are that no densification occurs in the compact.

GB motion has also been noted recently in the case of sintering of $\alpha\text{-alumina}$ (Komatsu and Fujita 1991). As their specimen was heated to 2300 K under stress,

particles in the size range of 10 nm acted as 'seed' crystals for the recrystallization of larger particles which then grew epitaxially. Though the results of Komatsu and Fujita are exactly opposite those indicated by Figure 4.26, it should be noted their specimens were powder compacts constrained by a heating/deformation holder. The present results represent the sintering of two 'free-body' particles where the smaller particle is clearly not a perfect 'seed' crystal.

It should be noted that in all of the sintering experiments, there was no evidence for the formation of the α -phase of alumina. That α -alumina was not observed may be the result of several factors. The temperature required for the equilibrium transformation of θ - to α -alumina is at least 1250°C. It may be that the dwell times used in these experiments were too short to allow the UFPs to complete the transformation, even though the temperature may have exceeded 1250°C. It may also be possible that under the 'vacuum' conditions (10 kPa) of the sintering experiments that the formation of α -alumina is not favorable regardless of the temperature, or is kinetically limited (Steiner et al. 1971). This explanation is supported by the results of Iijima (1985) who sintered UFPs of δ -alumina at 1350°C for 2 hours under vacuum conditions. There was no evidence of a transformation to α -alumina. Further buttressing this argument, Hirayama (1987) sintered Iijima's powders at 1260°C for 1 hour and noted the transformation to the α -phase, in addition to the presence of the transition phase aluminas. Furthermore, Warble (1985) sintered γ -alumina at 1150°C for 48 hours under atmospheric conditions and observed the transformation to α -alumina.

Chapter Five. Conclusions and Future Work

§5.1 Research Summary

The major accomplishments of this study can be summarized as follows;

An ultra-high vacuum (UHV) system has been constructed comprised of a UHV-HREM, a UHV furnace and a UHV specimen transfer manipulator. The UHV-HREM was extensively modified by the redesign of pumping systems, specimen holders and other equipment and achieves a base operating pressure at the specimen of 10^{-8} Pa. The UHV furnace chambers for the production and collection of the ultrafine particles (UFPs) were designed and constructed to achieve a base pressure of 4×10^{-7} Pa. The UHV specimen transfer system allows the sintered samples to be placed in the UHV-HREM under complete vacuum conditions.

The UFPs produced by the arc discharge have the spinel structure where the oxygen anions occupy a closed packed array with aluminum cations occupying the octahedral and tetrahedral sites in the lattice. A 'new' form of the orthorhombic δ -phase was observed to have lattice parameters of $a_{\delta}=1.58$ nm, $b_{\delta}=1.17$ nm, $c_{\delta}=0.79$ nm with a space group of $P2_12_12$ or $P2_12_12_1$. The monoclinic θ -phase was also possibly observed with the cell parameters of $a_{\theta}=1.09$ nm, $b_{\theta}=0.56$ nm, $c_{\theta}=0.27$ nm, $\beta=103.3^{\circ}$ with the space group of $B2/m$.

The sintering behavior of these UFPs demonstrates three major issues; the surface faceting due to the Wulff construction plays a major role in determining the final sintering geometry with sintering occurring predominantly on the closed-packed $\{111\}$ facets. Surface diffusion is the predominant mechanism for sintering, as evidenced by the fact that many sintered particles have their initial adhesion structure 'locked-in' during sintering with

no reorientation occurring. Furthermore, the necks formed during sintering have well-defined, atomically-sharp contact angles which suggests that the neck growth process is controlled by the faceted structures and may be modeled by a mechanism similar to crystal growth due to ledges, grain boundaries, and twins. The driving force for sintering can be considered as a chemical potential difference between facet surfaces and the neck region.

Phase transformations may occur during sintering with the consequence of grain boundary migration and epitaxial crystal growth. Transformations to the δ -phase were observed with both grain boundary migration and grain coalescence competing with the sintering process. No transformations to α -alumina were observed when sintering occurred under 'vacuum' conditions.

§5.2 Future Directions

There remain many questions to be answered in the study of the sintering behavior of ultrafine particles. For example, the effects of dopant materials on the sintering behavior needs further investigation. Dopants could be added to the UFPs by alloying the aluminum electrodes with the desired additive (e.g. add a few ppm of Mg to have MgO dopant). This would insure that the dopant was incorporated at the atomistic scale during initial particle formation. The addition of dopants would necessitate the use of both Auger and energy loss spectroscopy to determine whether there is any substantial segregation of the dopant to the particle surfaces where presumably it would have the greatest effect on the sintering properties. The use of magnesium as a dopant presents the possibility that the UFPs resulting from the arc discharge will have the MgAl_2O_4 spinel structure which may form in either the *normal* or *inverse -spinel* configuration. The formation of these spinels would require a completely homogeneous alloy of aluminum/magnesium electrodes.

This study was concerned with the behavior of alumina particles as α -alumina is a well-known ceramic material. However, the sintering behavior of other materials is of further interest. Replacing the aluminum electrode materials in the arcing apparatus with nickel would be a simple and convenient way of investigating ultrafine particles of nickel oxide. Nickel is a non-thermionic metal, as is aluminum, and so the arc discharge is the ideal method to produce NiO particles. In order to study materials which are not amenable to the arc discharge method, the electrodes may be replaced by a suitable sample holder (boat) and standard evaporation techniques employed.

It is further clear from this study that more control is needed over the flow characteristics of the furnace. That is, with current furnace and flow equipment there exists only a narrow range of operation which allows a suitable sample to be obtained. This can be alleviated by replacing the furnace tube a wider one. For instance, the current 5 mm ID and 11 mm OD tube could be replaced with one having dimensions of 10 mm ID and 15 mm OD without having to alter any of the UHV seals or the power and thermocouples connections. This new tube, with triple the volume, allows greater control over the dwell times in the furnace and also provides more structural integrity with respect mechanical and thermal stresses. An added benefit would be that a wider tube has a higher conductance for the vacuum system.

REFERENCES

- Ai, R. "Design of a TEM/STEM Auger detector." *Proceedings of the 47th Annual Meeting of the Electron Microscopy Society of America* G.W. Bailey. 98-99. San Francisco: San Francisco Press, 1989.
- Ajayan, P.M. "Phase instabilities in small particles." *Ph.D. Thesis*, Northwestern University (1989).
- Allpress, J.G. and J.V. Sanders. "The structure and orientation of crystals in deposits of metals on mica." *Surface Sci.* 7 (1967): 1-25.
- Anstis, G.R. and M.A. O'Keefe, unpublished (1977).
- Ashby, M.F. "A first report on sintering diagrams." *Acta Metall.* 22 (1974): 275-289.
- Avalos-Borja, M., F.A. Ponce, D. Su, H. Poppa and M. Boudart. "Applications of in-situ UHV and high resolution TEM to the study of small particles." *High Resolution Microscopy of Materials*, 139, 81-86. Pittsburgh, PA: Materials Research Society Symposium Proceedings, 1989.
- Balluffi, R.W. and R. Maurer. "On rotating sphere-on-a-plate experiments and the question of whether high angle grain boundaries melt below bulk melting temperatures." *Scripta Metal.* 22 (1988): 709-713.
- Berger, S. D., I. G. Salisbury, R. H. Milne, D. Imeson and C. J. Humphreys. "Electron energy-loss spectroscopy studies of nanometer-scale structures in alumina produced by intense electron-beam irradiation." *Phil. Mag. B* 55, 3 (1987): 341-358.
- Bleeker, A. and P. Kruit. "A condenser objective lens with asymmetric polepieces to facilitate the extraction of secondary and Auger electrons." *Rev. Sci. Instrum.* 61 (1990): 350-356.
- _____. "The magnetic parallelizer as an optical element for Auger electrons: further characterization." *Nucl. Instrum. Methods Phys. Res. A* 298 (1990b): 269-278.
- Bleeker, A.J., P. Kruit and T. van Spronsen. "A UHV scanning transmission electron microscope for Auger electron spectroscopy." *Ph.D. Thesis*, Delft TU (1991).
- Bonevich, J.E. "Surface faceting in small ceramic particles." *Proceedings of the 47th Annual Meeting of the Electron Microscopy Society of America* G.W. Bailey. 258-259. San Francisco: San Francisco Press, 1989.
- _____. "Correspondence to Dr. K. Ishizuka." (1990) unpublished.
- Bonevich, J. E. and L. D. Marks. "Contrast transfer theory for non-linear imaging." *Ultramicroscopy* 26 (1988): 313-319.
- _____. "The development of ultra-high vacuum high resolution electron microscopy." *Hitachi Instrument News* 17 (1989a): 4-17.

- ____. "Addendum: contrast transfer theory for non-linear imaging." *Ultramicroscopy* 32 (1990a): 297-298.
- ____. "Ultra-high vacuum electron microscopy of surfaces." *J. Electron Microsc. Tech.* (1990b): invited review, in press.
- ____. "Electron irradiation damage of α -alumina." *Ultramicroscopy* 35 (1991): 161-166.
- Buckett, M. I., J. W. Strane, D. E. Luzzi, B. W. Wessels and L. D. Marks. "Electron irradiation damage in oxides." *Ultramicroscopy* 29 (1989): 217-227.
- Bursill, L. A. and P. J. Lin. "Monolayer reconstruction on polar surfaces of ruby." *Phil. Mag. A* 60, 3 (1989): 307-320.
- Bursill, L. A., P. J. Lin and D. J. Smith. "Surface faceting and polarity of alumina." *Ultramicroscopy* 23 (1987): 223-228.
- Braski, D.N. "High-vacuum evaporation stage for an electron microscope." *J. Vac. Sci. Tech.* 7 (1970): 164-168.
- Cazaux, J., O. Jbara and K. H. Kim. "Radiation damage and charging effects of insulators in electron microscopy." *Proc. XIIIth Internat. Cong. Electron Microsc.*, 4, 796-797. San Francisco: San Francisco Press, 1990.
- Chokshi, A.H., A. Rosen, J. Karch and H. Gleiter. "On the validity of the Hall-Petch relationship in nanocrystalline materials." *Scripta Met.* 23 (1989): 1679-1684.
- Coble, R.L. "Initial sintering of alumina and hematite." *J. Am. Ceram. Soc.* 41 (1958): 55-62.
- ____. "Sintering crystalline solids. II. Experimental test of diffusion models in powder compacts." *J. Appl. Phys.* 32 (1961): 793-799.
- Coene, W., D. van Dyck and J. van Landuyt. "An extension of the standard theory of partial coherence for the effect of beam convergence in high resolution electron microscopy." *Optik* 73, 1 (1986): 13-18.
- Coulomb, P. "Experimental estimation of stacking fault and antiphase boundary energies." *J. Microsc. Spectrosc. Electron.* 3 (1978): 295-306.
- Dauger, A. and D. Fargeot. "TEM study of Al_2O_3 metastable phases." *Radiation Effects* 74 (1983): 279-289.
- Dieckmann, R. "Defects and cation diffusion in magnetite (IV): Nonstoichiometry and point defect structure of magnetite ($Fe_{3-\delta}O_4$)." *Ber. Bunsenges. Phys. Chem.* 86 (1982): 112-118.
- Dinghas, V.A. "Über einen geometrischen sat von Wulff für die gleichgewichtsform von fristallen." *Z. Kristall.* 105 (1943): 304-314.

- Egerton, R.F. *Electron energy-loss spectroscopy in electron microscopy*. New York: Plenum Press, 1986.
- Erb, U. and H. Gleiter. "The effect of temperature on the energy and structure of grain boundaries." *Scripta Metal.* 13 (1979): 61-64.
- Fadeeva, V. I., A. S. Kagan and L. S. Zevin. "Determination of stacking faults in the spinel-type lattice." *Acta Cryst. A* 33 (1977): 386-389.
- Fargeot, D., D. Mercurio and A. Dauger. "Structural characterization of alumina metastable phases in plasma sprayed deposits." *Mater. Chem. Phys.* 24 (1990): 299-314.
- Frank, J. "The envelope of electron microscopic transfer functions for partially coherent illumination." *Optik* 38 (1973): 519-536.
- Guile, A. E. "The electric arc." *The Physics of Welding* J.F. Lancaster. 120-145. Oxford: Pergamon, 1984.
- Hall, C.E. *Introduction to electron microscopy*, 2nd. Ed. New York: McGraw-Hill, 1966.
- Hall, E.O. "The deformation and aging of mild steel. III. Discussion of results." *Proc. Phys. Soc. London B* 64 (1951): 747-753.
- Hansson, I. and A. Tholen. "Adhesion between fine gold particles." *Phil. Mag. A* 37, 4 (1978): 535-559.
- Hatashi, T., T. Ohno, S. Yatsuya and R. Uyeda. "Formation of ultrafine metal particles by gas evaporation technique. IV. crystal habits of iron and fcc metals, Al, Co, Ni, Cu, Pd, Ag, In, Au and Pb." *Japan. J. Appl. Phys.* 16, 5 (1977): 705-717.
- Hausner, H.H. "Discussion on the definition of the term 'sintering'." *Sintering - New Developments* M.M. Ristic. 3-7. Amsterdam: Elsevier, 1979.
- Hawkes, P.W. *Electron optics and electron microscopy*, Taylor and Francis: London, 1972.
- _____. "Electron microscope transfer functions in closed form with tilted illumination." *Optik* 55, 2 (1980): 207-212.
- Hawkes, P.W. and E. Kasper. *Principles of electron optics*. London: Academic Press, 1989.
- Heinemann, K. and H. Poppa. "An UHV multipurpose specimen chamber with sample introduction system for in-situ transmission electron microscopy investigations." *J. Vac. Sci. Tech. A* 4 (1986): 127-136.
- Heinemann, K., M. J. Yacaman, C. Y. Yang and H. Poppa. "The structure of small, vapor-deposited particles. I. Experimental study of single crystals and particles with pentagonal profiles." *J. Cryst. Growth* 47 (1979): 177-186.

- Herring, C. "Effect of change of scale on sintering phenomena." *J. Appl. Phys.* 21 (1950): 301-303.
- _____. "Diffusional viscosity of a polycrystalline solid." *J. Appl. Phys.* 21 (1950): 437-445.
- _____. "Some theorems on the free energies of crystal surfaces." *Phys. Rev.* 82 (1951): 87-93.
- _____. "The use of classical macroscopic concepts in surface-energy problems." *Structure and Properties of Solid Surfaces* R. Gomer and C.S. Smith. 5-81. Chicago: Univ. of Chicago Press, 1953.
- Herrmann, G., H. Gleiter, and G. Baro. "Investigation of low energy grain boundaries in metals by a sintering technique." *Acta Metal.* 24 (1976): 353-359.
- Hersch, P., A. Howie, R.B. Nicholson, D.W. Pashley and M.J. Whelan. *Electron microscopy of thin crystals*. Kreiger: Malabar, FL, 1977.
- Hirayama, T. "High-temperature characteristics of transition Al_2O_3 powder with ultrafine spherical particles." *J. Am. Ceram. Soc.* 70 (1987): C122-C124.
- Hobbs, L.W. "Radiation effects in analysis of inorganic specimens by TEM." *Introduction to Analytical Electron Microscopy*, J.J. Hren, J.I. Goldstein and D.C. Joy. 437-480. Plenum: New York, 1979.
- Honjo, G., K. Takayanagi, K. Kobayashi and K. Yagi. "Ultra-high vacuum in-situ electron microscopy of growth processes of epitaxial thin films." *J. Cryst. Growth* 42 (1977): 98-109.
- Howie, A. and L.D. Marks. "Elastic strains and the energy balance for multiply twinned particles." *Phil. Mag. A* 49 (1984): 95-109.
- Howitt, D. G. and T. E. Mitchell. "Electron irradiation damage in $\alpha\text{-Al}_2\text{O}_3$." *Phil. Mag. A* 44, 1 (1981): 229-238.
- Iijima, S. "Ultra-fine spherical particles of γ -alumina: electron microscopy of crystal structure and surface morphology at atomic resolution." *Japan. J. Appl. Phys.* 23 (1984): L347-L350.
- _____. "Electron microscopy of small particles." *J. Electron Microsc.* 34 (1985): 249-265.
- Iijima, S. and T. Ichihashi. "Motion of surface atoms on small gold particles revealed by HREM with real-time VTR system." *Japan. J. Appl. Phys.* 24 (1985): L125-L128.
- _____. "Structural instability of ultrafine metal particles." *Phys. Rev. Lett.* 56 (1986): 616-619.
- _____. "Grain boundary migration in small gold particles." *Surface Sci.* 192 (1987): L872-L878.

- Ino, S. "Epitaxial growth of metals on rock salt faces cleaved in vacuum. II. Orientation and structure of Au particles formed in ultra-high vacuum." *J. Phys. Soc. Japan* 21 (1966): 346-362.
- _____. "Stability of multiply-twinned particles." *J. Phys. Soc. Japan* 27 (1969): 941-953.
- Ino, S. and T. Ogawa. "Multiply twinned particles at earlier stages of gold thin film formation on alkali halide crystals." *J. Phys. Soc. Japan*. 22 (1967): 1365-1374.
- Ishizuka, K. "Contrast transfer of crystal images in TEM." *Ultramicroscopy* 5 (1980): 55-65.
- Jayaram, V. and C.G. Levi. "The structure of δ -alumina evolved from the melt and the $\gamma \rightarrow \delta$ transformation." *Acta Metal.* 37 (1989): 569-578.
- Jenkins, W. K. and R. H. Wade. "Contrast transfer in the electron microscope for tilted and conical bright field illumination." *Developments in Electron Microscopy and Analysis*. 36. 115-118. London: Inst. Phys., 1977.
- Johnson, D.L. "New method of obtaining volume, grain-boundary, and surface diffusion coefficients from sintering data." *J. Appl. Phys.* 40 (1969): 192-200.
- Johnson, D.L. and I.B. Cutler. "Diffusion sintering: I. Initial stage sintering models and their application to shrinkage of powder compacts." *J. Am. Ceram. Soc.* (1963a): 541-545.
- _____. "Diffusion sintering: II. Initial sintering kinetics of alumina." *J. Am. Ceram. Soc.* (1963b): 545-550.
- Karch, J., R. Birringer and H. Gleiter. "Ceramics ductile at low temperature." *Nature* 330 (1987): 556-558.
- Kimoto, K., Y. Kamiya, M. Nonoyama and R. Uyeda. "An electron microscope study on fine metal particles prepared by evaporation in argon gas at low pressures." *Japan. J. Appl. Phys.* 2, 11 (1963): 702-713.
- Kingery, W.D. and M. Berg. "Study of the initial stages of sintering solids by viscous flow, evaporation-condensation, and self-diffusion." *J. Appl. Phys.* 26 (1955): 1205-1212.
- Kingery, W.D., H.K. Bowen and D.R. Uhlmann. *Introduction to Ceramics*. New York: Wiley-Interscience, 1976.
- Knotek, M. L. and P. J. Feibelman. "Ion desorption by core-hole Auger decay." *Phys. Rev. Lett.* 40, 14 (1978): 964-967.
- _____. "Stability of ionically bonded surfaces in ionizing environments." *Surface Sci.* 90 (1978): 78-90.

- Komatsu, M. and H. Fujita. "In situ experiments of sintering process in oxide ceramics by ultra-high voltage electron microscope." *Hitachi Instrum. News* 21 (1991): 18-23.
- Kondo, Y., K. Ohi, Y. Ishibashi, H. Hirano, H. Kobayashi, Y. Harada, K. Takayanagi, Y. Tanishiro, K. Kobayashi, N. Yamamoto and K. Yagi. "Development of ultra-high vacuum transmission electron microscope II. vacuum system." *J. Electron Microsc.* 36 (1987): 337-338.
- Kruit, P. "Magnetic through-the-lens detection in electron microscopy and spectroscopy. Part 1." *Adv. Opt. Electron Microsc.* 12 (1990): 93-137.
- Kuczynski, G.C. "Self-diffusion in sintering of metallic particles." *Met. Trans.* 185 (1949): 169-178.
- _____. "Study of the sintering of glass." *J. Appl. Phys.* 20 (1949): 1160-1163.
- Kuhn, H., G. Baero and H. Gleiter. "On the energy-misorientation relationship of grain boundaries." *Acta Metal.* 27 (1979): 959-963.
- Lange, F.F. "Sinterability of Agglomerated Powders." *J. Am. Ceram. Soc.* 67 (1984): 83-89.
- _____. "Influence of particle arrangement on sintering: a thermodynamic viewpoint." *J. de Physiq. Colloq.* C1 (1986): 205-217.
- Lee, W. E., K. P. D. Lagerlof, T. E. Mitchell and A. H. Heuer. "Radiation damage and non-equilibrium phases in Al_2O_3 ." *Phil. Mag. Lett. A* 51, 4 (1985): L23-L27.
- Linford, R.G. "Surface thermodynamics of solids." *Solid State Surface Science.* 2. M. Green. 1-152. New York: Marcel Dekker, 1973.
- Lis, J. and R. Pampuch. "The role of surface diffusion in the sintering of micropowders." *J. de Physiq. Colloq.* C1 (1986): 219-223.
- Marks, L.D. "Modified Wulff constructions for twinned particles." *J. Cryst. Growth* 61 (1983): 556-566.
- _____. "Surface structure and energetics of multiply twinned particles." *Phil. Mag. A* 49 (1984): 81-93.
- _____. "Direct atomic imaging of solid surfaces. I. Image simulation and interpretation." *Surface Sci.* 139 (1985a): 281-298.
- _____. "Inhomogeneous strains in small particles." *Surface Sci.* 150 (1985b): 302-318.
- _____. "Particle size effects on Wulff constructions." *Surface Sci.* 150 (1985c):358-366.
- _____. "Dynamical diffraction and high resolution electron microscopy: class notes." unpublished (1987).

- Marks, L.D. and D.J. Smith. "Direct surface imaging in small metal particles." *Nature* 303 (1983): 316-317.
- McDonald, M.L. and J.M. Gibson. "An UHV and ultra-high resolution transmission electron microscope." *Proceedings of the 42nd Annual Meeting of the Electron Microscopy Society of America*, G.W. Bailey. 436-437. San Francisco Press: San Francisco, 1984.
- Metois, J.J., S. Nitsche, and J.C. Heyraud. "An ultra-high-vacuum transmission and scanning electron microscope for crystal growth experiments." *Ultramicroscopy* 27 (1989): 347-358.
- Mitchell, T.E., B.J. Pletka, D.S. Phillips and A.H. Heuer. "Climb dissociation of dislocations in sapphire (α -Al₂O₃)." *Phil. Mag.* 34 (1976): 441-451.
- Mochel, M. E., C. J. Humphreys, J. A. Eades, J. M. Mochel and A. M. Petford. "Electron beam writing on a 20 Å scale in metal β -aluminas." *Appl. Phys. Lett.* 42, 4 (1983): 392-394.
- Moorhead, R.D. and H. Poppa. "An ultrahigh-vacuum specimen chamber for in-situ electron microscopy of vapor deposition processes." *Proceedings of the 27th Annual Meeting of the Electron Microscopy Society of America* G.W. Bailey. 116-117. Claitor: Baton Rouge, LA, 1969.
- Mykura, H. "Grain boundary energy and the rotation and translation of Cu spheres sintering onto a substrate." *Acta Metal.* 27 (1979): 243-249.
- Nichols, F.A. "Coalescence of two spheres by surface diffusion." *J. Appl. Phys.* 37 (1966): 2805-2808.
- Nieman, G.W., J.R. Weertman and R.W. Seigel. "Microhardness of nanocrystalline palladium and copper produced by inert-gas condensation." *Scripta Metal.* 23 (1989): 2013-2018.
- _____. "Tensile strength and creep properties of nanocrystalline palladium." *Scripta Metal.* 23 (1990): 145-150.
- O'Keefe, M. A. and W. O. Saxton. "The 'well-known' theory of electron image formation." *Proceedings of the 41st Annual Meeting of the Electron Microscopy Society of America* G.W. Bailey. 288-289. San Francisco: San Francisco Press, 1983.
- O'Keefe, M.A. "Resolution-damping functions in non-linear images." *37th Annual Proceedings of the Electron Microscopy Society of America* G.W. Bailey. 556-557. San Francisco: San Francisco Press, 1979.
- Ohi, K., Y. Kondo, Y. Ishibashi, H. Hirano, H. Kobayashi, Y. Harada, K. Takayanagi, Y. Tanishiro, K. Kobayashi, N. Yamamoto, and K. Yagi. "Development of ultra-high vacuum transmission electron microscope I. specimen system." *J. Electron Microsc.* 36 (1987): 337.

- Ohno, T., S. Yatsuya and R. Uyeda. "Formation of ultrafine metal particles by gas evaporation technique. III. Al in He, Ar and Xe, and Mg in mixtures of inactive gas and air." *Japan. J. Appl. Phys.* 15, 7 (1976): 1213-1217.
- Pells, G. P. and D. C. Phillips. "Radiation damage of α -Al₂O₃ in the HVEM. I. temperature dependence of the displacement threshold." *J. Nucl. Mater.* 80 (1979): 207-214.
- _____. "Radiation damage of α -Al₂O₃ in the HVEM. II. radiation damage at high temperature and high dose." *J. Nucl. Mater.* 80 (1979): 215-222.
- Pells, G. P. and A. Y. Stathopoulos. "Radiation damage in the cation sublattice of α -Al₂O₃." *Radiation Effects* 74 (1983): 181-191.
- Petch, N.J. "The cleavage strength of polycrystals." *J. Iron Steel Inst.* 174 (1953): 25-28.
- Poppa, H. and R.D. Moorhead. "The use of RF-plasma reactions for in-situ transmission electron microscopy studies." *Ultramicroscopy* 23 (1987): 271-274.
- Poppa, H. and R.D. Moorhead. "UHV in-situ microscopy of precipitation and gas reactions of very small Pt particles." *Surface Sci.* 106 (1981): 478-482.
- Poppa, H., K. Heinemann and A.G. Elliot. "Epitaxial orientation studies of gold on UHV-cleaved mica during early stages of nucleation and growth." *J. Vac. Sci. Tech.* 8 (1971): 471-480.
- Poppa, H., R.D. Moorhead and K. Heinemann. "Summary of in-situ epitaxial nucleation and growth measurements." *J. Vac. Sci. Tech. A* 11 (1974): 132-135.
- Porter, D.A. and K.E. Easterling. *Phase transformations in metals and alloys*, 199-201. New York: Van Nostrand, 1981.
- Pulvermacher, H. "Der transmissions-kreuz-koeffizient fur die elektronenmikroskopische abbildung bei partiell koharerer beleuchtung und elektrischer instabilitat." *Optik* 60 (1981): 45-60.
- Ramaker, D.E. "Mechanisms for Excited Neutral and Negative and Positive Ion Desorption from Surfaces," *Desorption Induced by Electronic Transitions: DIET II*, W. Brenig and D. Menzel. 10-23. Berlin: Springer, 1985.
- Raman, S.V., R.H. Doremus and R.M. German. "Mechanisms of initial sintering of a fine alumina powder." *J. Physiq. Colloq.* C1 (1986): 225-230.
- Reed-Hill, R.E. *Physical Metallurgy Principles* 2nd Ed. 293., New York: Van Nostrand, 1973.
- Reimer, L. *Transmission Electron Microscopy*, D.L. MacAdam. Berlin: Springer, 1984.
- Rooksby, J. *X-ray identification and crystal structures of clay minerals*. London: 1951.

- Saito, Y. "Crystal structure and habit of silicon and germanium particles grown in argon gas." *J. Cryst. Growth* 47 (1979): 61-72.
- Scott, W.D. "Twinning shear in alumina." *J. Am. Ceram. Soc.* Sept. (1983): C161-C162.
- Searcy, A.W. "Driving force for sintering of particles with anisotropic surface energies." *J. Am. Ceram. Soc.* 68 (1985): C267-C268.
- Shikama, T. and G. P. Pells. "Radiation damage in pure and helium-doped α -Al₂O₃ in the HVEM. Qualitative aspects of void and aluminum colloid formation." *Phil. Mag. A* 47, 3 (1983): 369-379.
- Shingu, P.H. "Effect of competitive mechanisms upon densification during the initial stage of sintering." *Ph.D. Thesis*, Northwestern University (1967): 64.
- Smith, D. J., L. A. Bursill and D. A. Jefferson. "Atomic imaging of oxide surfaces. I. general features and surface rearrangements." *Surface Sci.* 175 (1986): 673-683.
- Smith, D. J., J. Podbrdsky, P. R. Swann and J. S. Jones. "Initial experiences with a 300-kV HREM converted for UHV operation." 289-294. *High Resolution Microscopy of Materials*, 139. Pittsburgh, PA: Materials Research Society Symposium Proceedings, 1989.
- Smith, J.V. *Geometrical and structural crystallography*, New York: Wiley, 1982.
- Somorjai, G.A. "Principles of surface chemistry." *Fundamental Topics in Physical Chemistry*, 3, H.S. Johnston. Englewoods Cliffs, New Jersey: Prentice-Hall, 1972.
- Spence, J.C.H. *Experimental High Resolution Electron Microscopy*, Oxford: Clarendon, 1981.
- Stathopoulos, A. Y. and G. P. Pells. "Damage in the cation sublattice of α -Al₂O₃ irradiated in an HVEM." *Phil. Mag. A* 47, 3 (1983): 381-394.
- Steiner, C.J.-P., D.P.H. Hasselman and R.M. Spriggs. "Kinetics of the gamma-to-alpha alumina phase transformation." *J. Am. Ceram. Soc.* 54 (1971): 412-413.
- Taftø, J. and J. Zhu. "Electron energy-loss near edge structure (ELNES), a potential technique in the studies of local atomic arrangements." *Ultramicroscopy* 9 (1982): 349-354.
- Takayanagi, K., K. Yagi, K. Kobayashi, and G. Honjo. "Techniques for routine UHV in-situ electron microscopy of growth processes of epitaxial thin films." *J. Phys. E* 11 (1978): 441-448.
- Tasker, P. W. "Surfaces of magnesia and alumina." 176-189. *Advances in Ceramics*, 10. Columbus: Am. Ceram. Soc., 1984.
- Teng, M.-H. "Study of initial-stage sintering of ultrafine ceramic particles." *Ph.D. Thesis*, Northwestern University (1991): in preparation.

- Tholen, A. R. "On the formation and interaction of small metal particles." *Acta Metall.* 27 (1979): 1765-1778.
- _____. "Vibrations and martensitic transformation in small cobalt particles." *Surface Sci.* 106 (1981): 70-78.
- _____. "Character of adhesion strain fields at contacts between spheres of different materials." *Microscopic aspects of adhesion and lubrication*. J.M. Georges. 263-277. Amsterdam: Elsevier Scientific Publishing Company, 1982.
- Tomokiyo, Y., T. Kuroiwa and C. Kinoshita. "Defects occurring at or near surfaces of α - Al_2O_3 during electron irradiation." *Internatl. Symp. on New Directions and Future Aspects of HVEM*. 56-57. Osaka University, Nov, 1990.
- Tucker, D.S. "Gamma-to-alpha transformation in spherical aluminum oxide powders." *J. Am. Ceram. Soc.* 68 (1985): C163-C164.
- Uyeda, R. "Crystallography of ultrafine particles." 715-737. *Sintering Key Papers*. London: Elsevier Applied Science, 1990.
- Valentine, T. M. "On the use of critical energy techniques for the measurement of surface energies of ceramics. Part II. The temperature variant method." *Mater. Sci. & Engin.* 30, 3 (1977): 211-218.
- Vergnon, P.G., F.E. Juillet, M.P. Astier and S.J. Teichner. "Sintering of ultrafine particles of anatase and delta alumina." 47-62. *Science of Ceramics*, 5, C. Brosset and E. Knopp. Gothenburg: Swedish Institute for Silicate Research, 1970.
- Wade, R. H. and J. Frank. "Electron microscope transfer function for partially coherent axial illumination and chromatic defocus spread." *Optik* 49 (1977): 81-92.
- Wade, R. H. and W. K. Jenkins. "Tilted beam electron microscopy: the effective coherent aperture." *Optik* 50, 1 (1978): 1-17.
- Warble, C.E. "Surface structure of spherical gamma-alumina." *J. Mater. Sci.* 20 (1985): 2512-2516.
- Weertman, J. and J.R. Weertman. *Elementary Dislocation Theory*. London: MacMillan, 1969.
- Yacaman, M. J., K. Heinemann, C. Y. Yang and H. Poppa. "The structure of small, vapor-deposited particles. II. Experimental study of particles with hexagonal profile." *J. Cryst. Growth* 47 (1979): 187-195.
- Yatsuya, S., R. Uyeda and Y. Fukano. "Mean size and size distribution of metal fine particles produced by gas evaporation technique." *Japan. J. Appl. Phys.* 11 (1972): 408.
- Yatsuya, S., S. Kasukabe and R. Uyeda. "Formation of ultrafine metal particles by gas evaporation. I. aluminum in helium." *Japan. J. Appl. Phys.* 12, 11 (1973): 1675-1684.

Appendix One. Electron Beam - Solid Interactions

Since the electron microscope must be used to observe the structural characteristics of the alumina powders, it is very important to know how the particles behave during this period of observation. That is, it must be determined whether the alumina particle structures observed are instrument/specimen artefacts and if the particles interact with the electron beam in such a way as to change their structures during observation. This field of research is called radiation damage and the electron microscope serves a useful function to this end; the electron beam provides the ionizing radiation source as well as a means to observe the structural changes occurring at the atomic level during the radiation process. In the following section is a brief summary of the types of beam-specimen interactions produced in the electron microscope. Also presented are some experimental results conducted (by JEB) with various phase aluminas (both α - and the γ -, δ - UFPs).

Displacement or Knock-on Damage

In this case the electron radiation damage results in the physical displacement of an atom from its lattice position to an interstitial site forming a Frenkel pair (Hobbs 1979). The Frenkel pairs are created when the energy of the electron beam exceeds a certain threshold defined by;

$$E_{th} = m_0c^2 \left[\sqrt{\frac{ME_d}{2m_0^2c^2} + 1} - 1 \right], \quad (A1.1)$$

where m_0c^2 is the rest energy of the electron, M the mass of the displaced atom and E_d the displacement energy. In diatomic solids the value of E_d is a function of the electronic state (i.e. anion/cation). In addition, E_d is usually a function of orientation and temperature. As a result, the values of E_{th} for each species may be quite different leading to the preferential damage on a certain sublattice in the material. The cross-section for interaction of the

primary electrons with Z free electrons in the atomic nucleus is;

$$\sigma_e = Z \frac{8\pi a_0^2 U_R}{m_0 v^2} \frac{U_R}{T_{\min}} \quad (\text{A1.2})$$

where a_0 is the Bohr radius, U_R the Rydberg energy, and T_{\min} the minimum transferable energy, essentially lattice vibrations, $\approx .01$ eV. Equations A1.1 and A1.2 are the McKinley-Feshbach relations for knock-on damage. These relations hold only for electron-nuclear interactions (assumes electron beam heating to be a minimum) and also are not valid for those elements where $Z \geq 29$.

Radiolysis Damage

Radiolysis refers to the case whereby the electrons passing through the material interact with the atoms such that electronic state instabilities may occur resulting in a change in the chemical bonding of the atomic species (Hobbs 1979). This usually occurs with substantial momentum transfer to an atomic nucleus. Materials that do not localize electronic excitations are highly susceptible to radiolytic damage mechanisms (i.e. insulators damage, metals do not). The usual criterion for radiolysis is that the electronic excitations have energies at least as large as the energy stored in the resulting displacements, and an efficient mechanism for transferring this energy into momentum of displaced atom cores. That is;

$$U_{\text{eh}} = U_L + U_A - U_I \quad (\text{A1.3})$$

where U_{eh} is the energy of the electron-hole pair, U_L the lattice binding energy, U_A the electron affinity for the anion, and U_I the ionization potential for the cation. The necessary condition for radiolysis is that $U_{\text{eh}} > U_L$ or $U_A - U_I > 0$.

Radiation Damage in Alumina (Previous Results)

Alumina (α phase) is a Class 4 material (Buckett et al. 1989), that is a material that displays surface initiated beam damage. Alumina was originally not known to suffer radiolytic damage and instead thought to damage by ballistic knock-on mechanisms inducing aggregated defects. Pells and Phillips (1979a, 1979b) determined the temperature and dose dependence of E_{th} . They found that for temperatures below 570 K the threshold energy was constant at 390 ± 10 keV. For temperatures above 870 K the threshold fell to 200 keV. From these results they calculated widely different displacement energies, E_d , for aluminum (18 eV) and oxygen (≈ 75 eV). Howitt and Mitchell (1981) reanalyzed the data and determined that, using a model of thermally activated escape of close Frenkel pairs, the value for aluminum should be ≈ 45 eV whereas oxygen remained unchanged. In their study, dislocation loops formed on the (0001) basal and $\{10\bar{1}0\}$ prism planes. Stathopoulos and Pells (1983) damaged α - Al_2O_3 with 300 keV electrons at 1055 K, a situation where only aluminum atoms are displaced, and also observed the formation of basal and prismatic plane dislocation loops. However, in both cases, the method of specimen preparation (ion-thinned samples) directly affects the damage results, as recognized by Lee et al. (1985) where the amorphous Al_2O_3 (resulting from ion-beam thinning) recrystallized to γ - Al_2O_3 in a 125 keV microscope.

Smith et al. (1986) observed damage processes in ruby Al_2O_3 to result in a 'patchwork quilt' structure. The ruby samples damaged similarly at 100 keV and eventually suffered from hole-drilling in the crystal. Under an intense electron beam, Mochel et al. (1983) were able to drill holes in metal β -aluminas. Berger et al. (1987) also drilled holes in both β - and amorphous aluminas where metallic aluminum was detected by electron energy loss spectroscopy (EELS). They attributed the damage mechanism to a Knotek-Feibelman (1978a, 1978b) process whereby oxygen atoms are desorbed from the

surface by a core-level ionization process.

Recently, the formation of 'dark-line' faceting in α -alumina in a medium voltage EM was reported by Bursill et al. (1987). This faceting phenomenon was attributed by Bursill and Lin (1989) to be a 'monolayer' of a spinel phase, though detailed image simulation was absent from the report. This dark-line contrast was also observed by myself at the same time. After private correspondence with Dr. D.J. Smith (January 1988) a series of tilting experiments about the facets were conducted (by JEB) with the result that no structure could be resolved in the facets.

As part of a wider study of the behavior of materials in the space environment (in association with Northwestern's Center for Surface Radiation Damage Studies), α -alumina was damaged in the electron microscope under various conditions. Consistent with earlier results, facet formation was detected on the crystal surfaces. Facet formation occurred rapidly under electron irradiation and, in most cases, can be considered a feature of the initial surface. Whereas Bursill et al. (1987) reported facet formation on the $[11\bar{2}0]/(0006)$ habits of alumina, we have determined that the facet formation is not limited to this zone and occurred on almost all crystal orientations. In addition, the facet formation appears to be intimately linked with the ambient vacuum at the specimen. While I detected facets in the C-HREM, they did not form when alumina was irradiated under UHV conditions. Instead, small crystallites of aluminum formed on the surface of the irradiated alumina (Bonevich and Marks 1991).

Experimental Method

The α -alumina specimens were prepared by crushing Aesar corundum (99.99%) in a methanol slurry. The resulting solutions were dispersed on holey films; carbon for the C-HREM and SiO for the UHV-HREM. The Hitachi H9000 HREM used for the C-HREM work had a vacuum of 2×10^{-5} Pa at the specimen while the UHV-H9000

experiments were conducted at a working vacuum of 3×10^{-8} Pa at the specimen. The H9000 microscopes have an accelerating voltage variable from 100 to 300 keV. The flux conditions were measured by means of a Faraday cup in the H9000 and similar conditions were established for use in the UHV-H9000 for comparison.

The UFPs of γ - and δ -alumina were prepared in the UHV furnace system and collected onto SiO films. The specimens were damaged in both the UHV-H9000 and the HF2000 microscopes. The HF2000 is a field-emission type microscope operating at 200 keV. The high brightness field-emission source can be focused into a 1 nm probe to conduct nano-diffraction, nano-analysis and convergent-beam studies. The pressure at the specimen is $\approx 10^{-6}$ Pa and liquid nitrogen (LN2) cold traps and fingers must be extensively used to minimize contamination.

Radiation Damage in Alumina (Present Results)

Specimens of α -alumina were damaged in the C-HREM under low flux (10 A/cm^2) which is typical of the conditions used in HREM. From the onset of observation the faceting phenomenon was observed; that is, in the time necessary to orient a crystal along a specific zone axis (a few minutes) facets had already formed along the surface and thus, in most cases, can be considered a feature of the initial surface. Under prolonged electron irradiation the faceting became more extensive though the facets themselves remained confined to a specific habit plane. Figure A1.1 shows a time sequence under constant flux in non-UHV conditions at 300 keV; the faceting is clearly evident.

The time sequence also reveals evidence for a phase transformation occurring at the surface of the crystal. In fact, it may be speculated from Figure A1.1(c) that the orientation of the new phase at the surface very closely resembles the [112] zone of γ -alumina. This result would be consistent with the observation of Bursill and Lin (1989) that the dark-line facet is actually the {111} surface termination of the [112] orientation of

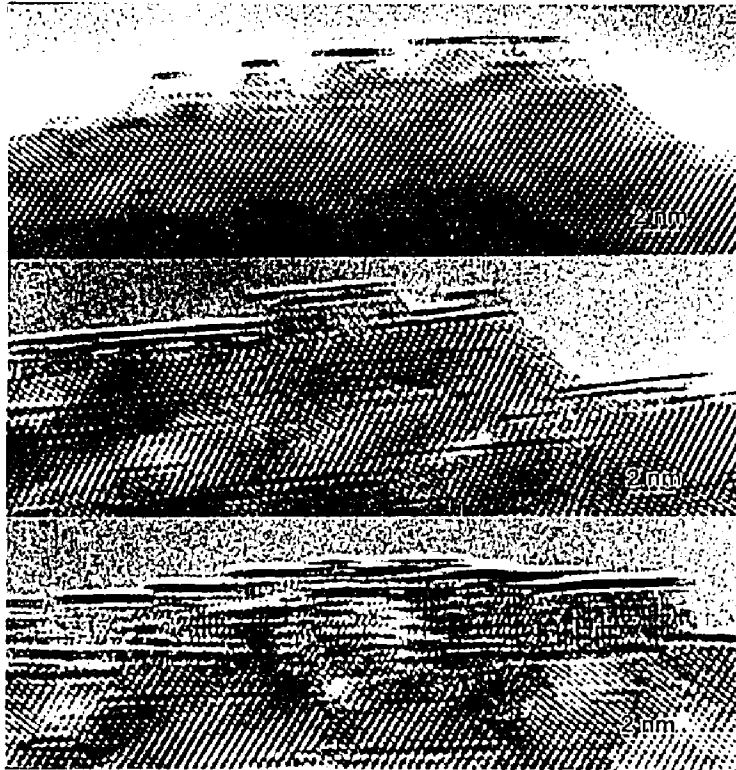


Figure A1.1. Time sequence of the damage process of α -alumina $[11\bar{2}0]$ zone. The initial surface in (a), after 30 minutes of low flux (10 A/cm^2) damage. After 2 hours of damage (c) the faceting has become more extensive and the surface phase resembles $[112]_{\gamma}$ zone.

γ -alumina. However, whereas their surface termination resulted in only a 'monolayer,' the evidence here suggests that a surface phase of many 'monolayers' is actually stable under electron irradiation.

Simultaneous with facet formation, α -alumina suffered from surface roughening, due to ionization damage, resulting in a 'quilt' pattern of contrast between thick and thin regions of the crystal. Facet formation was observed for a variety of different crystal orientations and always occurred on those surfaces where 'normal' atomic terminations result in planes of either oxygen or aluminum, see Figures A1.2 (crystal structure), and A1.3 and A1.4 (HREM images). The damage process also appeared uncorrelated with the crystal orientation. Under conditions of higher electron flux, and lower electron energy, both facet and 'quilt' formation accelerated.

We should note that while facet formation occurred along many orientations, the facet itself always appeared in profile, as a 'monolayer'. Consider, for example, facets along $[2\bar{2}01]$ which form upon $(0\bar{1}14)$ habits. This profile surface, when viewed in plan view, is representative of the $[11\bar{2}0]$ orientation, and assuming the spinel structure of the facets is correct, would give discernibly different HREM images for faceted and unfaceted surfaces. Such differences have not been detected in the images implying that the facets form parallel to the electron beam, i.e. top and bottom surfaces of the crystal are unfaceted.

The damage process in α -alumina was accelerated by irradiating with 100 keV electrons, see Figure A1.5. In the C-HREM the initial surfaces were smooth and very little faceting was present; however, after irradiation for 90 minutes ($\approx 20 \text{ A/cm}^2$) the crystal surfaces had extensive faceting and considerable surface roughening. In the 100 keV regime, ionization processes are favored relative to ballistic processes whereas the opposite is true at higher electron energies. That α -alumina damages, and at a rather fast rate, indicates that an ionization mechanism is responsible for facet formation either as a

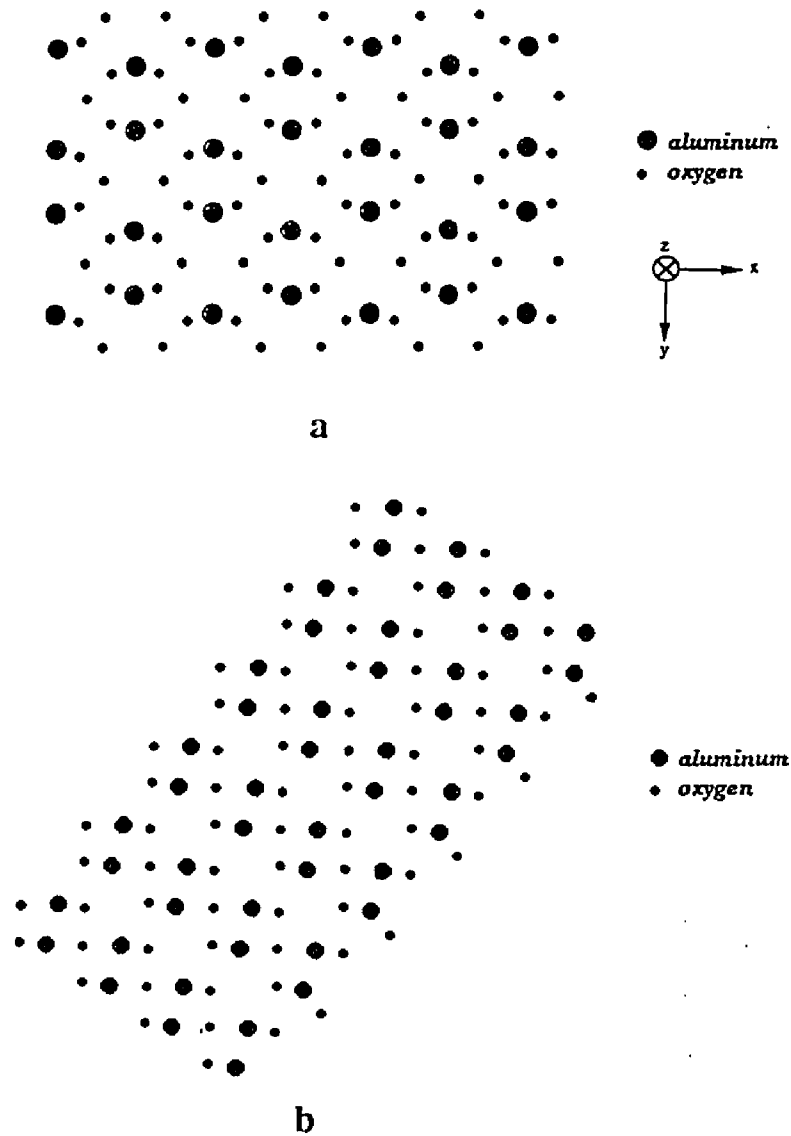


Figure A1.2. The unit cell crystal structure from a multislice calculation for the $[2\bar{2}01]$ zone of α -alumina (a). The dark-line facets occur along planes in the crystal which are either all aluminum or all oxygen (vertical). The horizontal planes have a mixed character and no faceting is observed there. In (b) the unit cell is viewed along the 'x-axis' and is, in fact, the $[11\bar{2}0]$ zone where faceting occurs along the (0006) planes which have been rotated to the vertical orientation.



Figure A1.3. The faceting occurs on almost all crystal orientations in α -alumina. Here the $[2\bar{2}01]$ zone also exhibits facets on planes which are layers of oxygen or aluminum.



Figure A1.4. The damage process accelerates at 100 keV in the CTEM. Here, the $[11\bar{2}0]$ zone damages after 90 minutes of medium flux (20 A/cm^2) irradiation.



Figure A1.5. The damage process under UHV conditions results in the formation of small crystallites of aluminum. Here, the initial surface of the $[2\bar{2}01]$ zone and after 1 hour of moderate flux (20 A/cm^2) irradiation.

contaminant catalyzed or intrinsic process. It should be noted that the presence of a carbon overlayer seems to locally quench the damage process as observed in many other materials (Buckett et al. 1989).

In contrast to the C-HREM results, crystals of α -alumina irradiated in the UHV-H9000 under similar flux conditions did not exhibit facet formation. Instead, under irradiation the formation of aluminum was detected. Figure A1.4 presents the results from the $[\bar{2}201]$ zone axis. (PEELS was performed on these specimens and indicated that the O K-edge intensity decreased during the irradiation process, though the structure of the Al L_{2,3}-edge could not be well resolved.) These results indicate that facet formation is controlled by the ambient vacuum environment of the the microscope. In addition, the crystallites that form on the surface do not wet the surface. These results are consistent with the observations of Valentine (1977) of molten metals on α -alumina substrates. Whereas the C-HREM can be expected to have a relatively 'dirty' vacuum of 10^{-5} Pa with molecular oxygen and residual hydrocarbons from pumps present, the UHV-H9000 represents a clean, dry environment of 10^{-8} Pa where the probability of surface reactions is strongly reduced. In addition, the alumina specimens were baked at 200°C in the specimen transfer chamber before insertion in the UHV microscope. This procedure, not typical of C-HREM experiments, also minimizes any surface contaminants.

Results on Ultrafine Particles

The ultrafine alumina particles were observed to damage in the electron microscope under both UHV and HF2000 environments. In the UHV, under low flux (imaging) conditions of $<10 \text{ A/cm}^2$, the surfaces of the UFPs became roughened after about 20 minutes, similar to Figure 4.7. The morphological changes are also quite similar to those observed with α -alumina under prolonged irradiation. Given that the damage process in α -alumina proceeds by an ionization mechanism, it is probable that the γ - and δ -phases are

also susceptible to radiolytic damage. Moreover, the UFP sizes of about 20-40 nm mean that the behavior is surface-controlled as opposed to properties dominated by the bulk.

Another interesting feature in the UHV environment is the formation of a dark-line contrast on several facets on the UFPs, e.g. Figure 4.13. These results are strikingly similar to the facets formed on α -alumina in the CTEM environment. If one assumes that the image simulation analysis of Bursill and Lin (1990) is correct, then the facet is comprised of a spinel phase in closed-packed relation to the bulk. The UFPs of γ - and δ -alumina are structural variants of the spinel phase, and therefore already have 'normal' surface terminations that would result in dark-line facet formation.

The damage process is accelerated when the UFPs are observed in the HF2000 environment. Here, at higher fluxes of 20 A/cm^2 , the surfaces begin to roughen almost immediately when the beam is placed upon the particles. Typically after 5 minutes of irradiation the particle surface is completely disordered. On larger particles the electron probe could be focused well enough that a small hole could be 'drilled' through the particle, leaving the surrounding crystal undisturbed.

The HF2000 is equipped with a PEEL spectrometer to conduct nano-analysis, ideal for investigating UFPs. PEELS was conducted on sintered particles in an effort to elucidate their chemical environment. Because the nano-probe is also highly intense, the particles suffer from damage during the analysis period. Given that both the α -phase and the UFPs suffer from radiolysis, one would expect acquired spectra that reveal the damage process occurring as a function of time (electron dose). Both the oxygen K-edge and the aluminum L_{2,3}-edges were analyzed during the irradiation process. The spectra from the UFPs show that the aluminum L_{2,3}-edge resembles that of oxidized aluminum as opposed to aluminum metal, see Figure A1.6. It is important to note that since the UFPs do not present a large sampling volume for EELS long acquisition times (e.g. 50 seconds) were

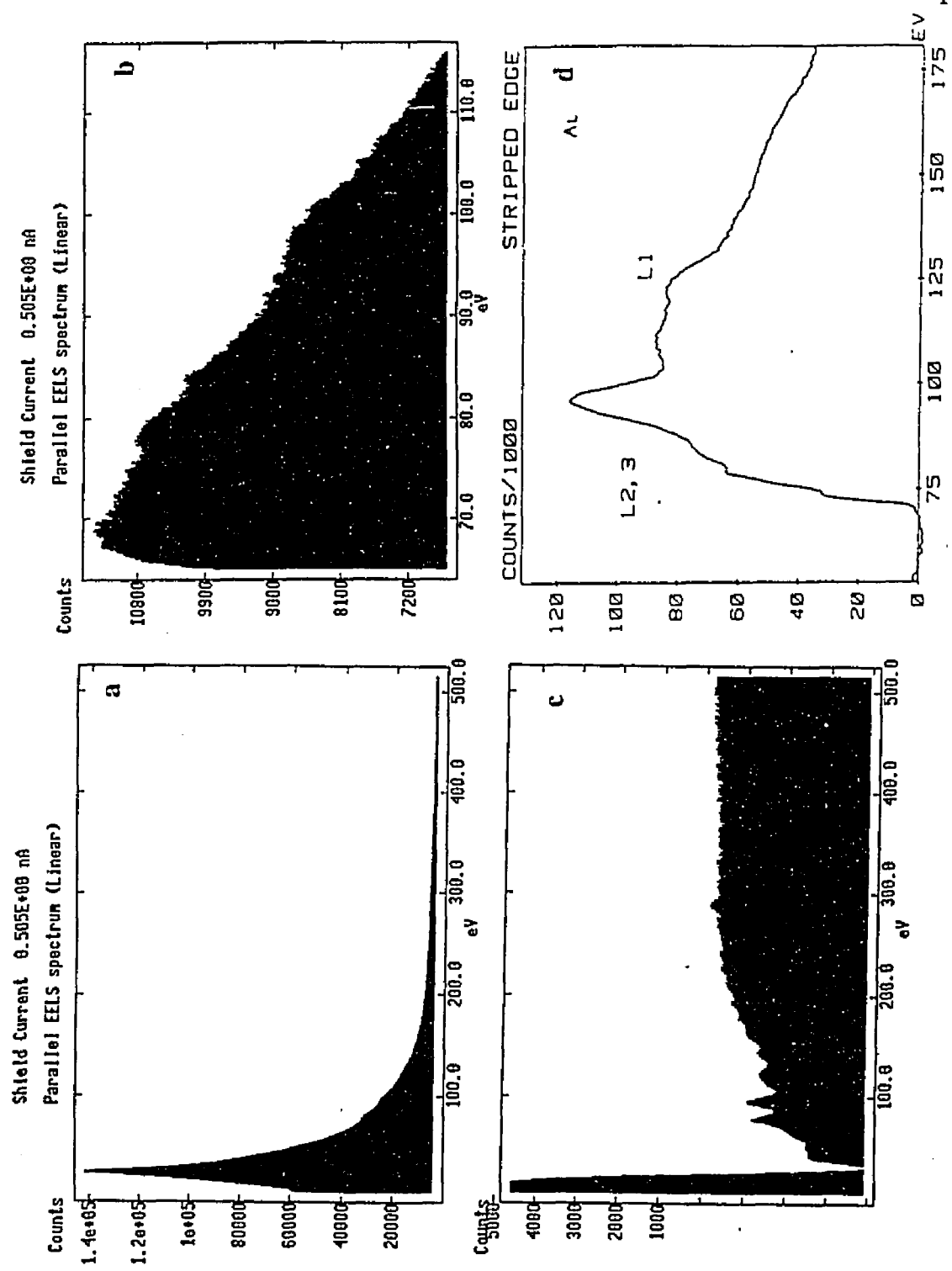


Figure A1.6. PEEL spectra of the UFPs in the HF2000. In (a) the spectra of Al L2,3. The near-edge structure of the L2,3 in (b) and the first derivative of (a) in (c). The stripped edge of aluminum metal (d) from the EELS Atlas (1983).

necessary to obtain good signal-to-noise ratios. Thus, we would have expected the UFPs to have damaged and reduced to aluminum metal during the acquisition time, though this was not observed in the few spectra that were obtained. The oxygen K-edge was also detected in these UFPs indicating that reduction of the oxide is not occurring during the spectra acquisition. This result can be explained by the fact that carbon contamination (which is substantial even with the extensive use of LN2 traps and cold fingers) quenches the damage process leaving the aluminum in an oxidized state.

Conclusions

As mentioned previously, the damage process in alumina in the case of hole drilling has been attributed to the Knotek-Feibelman (KF) oxygen ion desorption mechanism (1978a, 1978b). Although the KF mechanism is an attractive candidate for the damage process, this and earlier electron microscope studies cannot determine unambiguously whether KF or another ionization process, e.g. Ramaker (1985), is responsible. From the results it is clear that the surface faceting phenomenon in the case of α -alumina is a representative artefact of a 'dirty' microscope vacuum that typifies most C-HREMs. That is, during irradiation α -alumina preferentially ejects oxygen from the surface and the 'dirty' vacuum reoxidizes the aluminum that would otherwise be left on the surface. In more recent results, Tomokiyo et al. (1990) irradiated single crystal α -alumina and observed both facets and hole drilling in specimens prepared by Ar^+ ion milling and hot phosphorus etching, indicating that the ambient vacuum at the specimen plays a greater role in the damage process. In the clean environment of the UHV-HREM reoxidation of the facets is quenched allowing the reactive aluminum to remain in its metallic form and grow into stable crystallites. These results suggest that the facet formation in C-HREM is a dynamic balance between the desorption process and the high reactivity of metallic aluminum; one might envision a flux threshold above which the formation of aluminum might be stabilized

in even an oxidizing environment.

In the case of the UFPs of γ - and δ -phase spinels, the results also support an ionization damage mechanism. However, the question remains why the alumina particles do not reduce in the UHV environment to crystals of aluminum, as in the α -phase. One possible explanation is that there are several competing mechanisms for the damage process. Consider, for example, the classical case for collisional mechanics. The maximum energy transferred to an atom for displacement by an incident electron is;

$$E_{\max} = 2147.7 E \left[\frac{E + 1.022}{A} \right] \quad (\text{eV}) \quad (\text{A 1.4})$$

where E is the incident electron energy (in MeV) and A the mass (in amu) of the atomic species. For the case of 300 keV electrons, a substantial amount of energy, 32 eV, can be transmitted ballistically to the aluminum sublattice in addition to the electronic excitations suffered by the oxygen sublattice. Thus it is conceivable that the damage rates for both aluminum and oxygen are the same order of magnitude. Where in the case of α -alumina, the loss of aluminum from the surface could be replenished from the bulk, the UFP could not sustain this process resulting in the erosion of the entire particle.

Appendix Two. Fiddly Bits (Work on the UHV-HREM)

In order to make the sintering of the ultrafine ceramic particles a success, many design details had to be worked out to ensure the systems functioned as a whole. The UHV-HREM, being a prototype, needed extensive modifications to make it perform as intended. Listed below are most of the modifications and engineering work done by myself:

- Designed a titanium sublimation pump and placed it on the microscope to improve the pumping systems, complete with cooling lines.
- Modified the ion pump on the STC to include a TSP for the same reason. Its cooling lines are configured with double shut-off valves for STC mobility.
- Designed the specimen manipulation system to allow for UHV transfer of specimens into the STC from remote UHV chambers or atmosphere.
- The transfer system includes:
 - * Custom-designed 'grabber' mechanism for specimen manipulation. (Also useful for tilting pin re-alignment.)
 - * Magnetically-coupled manipulator with battery-powered ion pump.
 - * Reconfigured turbo pumping system to be able to evacuate transfer system to ultimate pressure of 1×10^{-6} Pa.
 - * The success of this UHV transfer system prompted Hitachi to include the design concept in their commercially available product.
- Redesigned the specimen holder to allow for 3 mm specimens. This enabled users other than myself to ion mill, anneal, perform LEED/Auger, ... with their specimens which was exceedingly difficult with Hitachi's original 2.3 mm holder.

- Lead the design concept for an ion milling holder without a spring clip that enabled a 5 mm specimen to be used if desired.
- Redesigned the tilting spring in the specimen cartridge to improve the tilting freedom.
- Designed the multiport flange on the STC to give a variety of instruments 'line-of-sight' at the specimen.
- Reconfigured the HREM turbo bellows anti-vibration collar to simultaneously minimize vibration and maintain proper alignment.
- Modified the HREM desiccator door panel to allow for film exchange while keeping the STC attached to the HREM (essential for true surface science).
- Reconfigured the heating flange circuits on the STC to allow for a more controlled bakeout of the system...this minimizes Hitachi's extreme thermal gradients and also allows some areas of the STC, such as the LEED, to be baked hotter than other regions (ion gun).
- Modified the lead shielding on Gatan's Model 666 parallel EELS to accommodate their Model 676 PEELS-compatible CCD-TV.

These are just some of the modifications and redesigns made to the UHV-HREM over the course of three years. As the instrument evolves there undoubtedly will be many more changes incorporated into the system.

Appendix Three. What Not To Do (Murphy Was Right)

During the construction process many different configurations were tested in order to determine proper procedures with respect to the operation and ease of use of the UHV furnace system. Concurrent with this process were several configurations which did not perform as expected, i.e. some event occurred that caused substantial operational impediments. As a direct result of these events, there was much consternation and more than a few grey hairs and sleepless nights. In keeping with the basic tenant of Murphy's Law; 'if something can go wrong, it will' this appendix has been compiled. All subsequent users of the UHV furnace should read this appendix first, discarding the rest. All the while the reader should keep in mind that the following events have already been done; i.e. no copycatting, if you want a PhD you'll just have to be original on your own!!

- 1• The UHV furnace is a *vacuum* chamber and, as such, you can not pressurize it without causing big leaks.
- 2• If you have the furnace at temperatures above 1000°C when doing rule #1, you'll cause a big fire and your lab will smell bad.
- 3• However, if you want to study big crystals of MoO₃, then you're in luck.
- 4• When installing a fragile furnace tube, do not put it in upside down (unless you want to work for NASA).
- 5• Moly induction coils are not very flexible, ceramic tubes break before they do. This is the corollary for rule #4.
- 6• Copper tubing isn't very flexible either.

- 7• If your turbo pump sounds like a marble is rolling around in it, send the pump back to France where they're experts at losing marbles.
- 8• When the turbo makes a little noise, maybe it's time to grease it before those damn marbles come back.
- 9• When degassing an ionization gauge, do not turn up the wattage control up real fast unless you want to evaporate thoriated iridium.
- 10• An aluminum wire electrode which is arcing with the stainless steel chamber walls probably will not form aluminum oxide. However, iron oxide (rust) is very interesting and you can work for the auto companies.
- 11• An efficient method of cleaning the inside of a vacuum chamber is to turn on the ion pump when the pressure is about 10 millitorr. The resulting plasma will do a good job unless the ion pump melts first.

The above listed items are only a small portion in the realm of possibilities with this complicated and sophisticated UHV furnace. Many other avenues exist, for example try to install a microwave or plasma furnace in the chamber. It is suggested that sunscreen #10 be applied in liberal amounts to all exposed areas.

Appendix Four. Contrast Transfer Program

This appendix includes the source code used to calculate the contrast transfer function as elaborated in Chapter Two. The code is by no means optimized, in fact far from it. It does however give the method for calculating the transmission cross-coefficient for conventional non-linear theory, the JEB/LDM improved TCC and its numerical solution, the TCC with the $\Delta\alpha$ cross-terms, and finally the solution to the matrix formulation.

```
PROGRAM EVERYONE
C
C THIS PROGRAM WILL CALCULATE
C THE SECOND ORDER EFFECTS IN NON-LINEAR IMAGING
C THEORY. IT GETS QUITE COMPLICATED
C
CHARACTER*10 P,W,X,Y,Z
CHARACTER*1 ANSWER
REAL U,V,Q,A,B,C,ALPHA,BETA,PI,SPHAB,LAM,DEF,RMSB,RMSA,
# DF_SPHAB,DF_DEF,DF_RMSB,DF_VOLT
COMPLEX F1,F2,F3,F4,F5
C
P = 'newone.dat'
W = 'cross.dat '
X = 'conven.dat'
Y = 'consec.dat'
Z = 'ishi.dat '
C
OPEN (UNIT=7,FILE=X,STATUS='UNKNOWN')
OPEN (UNIT=8,FILE=Y,STATUS='UNKNOWN')
OPEN (UNIT=9,FILE=Z,STATUS='UNKNOWN')
OPEN (UNIT=10,FILE=W,STATUS='UNKNOWN')
OPEN (UNIT=11,FILE=P,STATUS='UNKNOWN')
C
C CHI IS THE CONTRAST TRANSFER FUNCTION
C GRADCHI IS THE GRADIENT OF THE CTF
C SPHAB IS THE SPHERICAL ABERATION
C U, V AND Q ARE SPATIAL FREQUENCIES TO BE EVALUATED
C A,B,AND C ARE THE ANGLES BETWEEN U,Q,AND V
C ALPHA IS THE CONVERGENCE
C BETA IS THE FOCAL SPREAD
C LAM IS THE INCIDENT ELECTRON WAVELENGTH
C DEF IS THE DEFOCUS WE ARE CONSIDERING
```

```

C
C TERMS WILL BE CALCULATED ALONG THE WAY
C
  WRITE(6,99)
99  FORMAT(/, ' CONTRAST TRANSFER FUNCTION ROUTINE' /, /)
C
  PI = ACOS(-1.)
  DF_U = 0.0001
  DF_VOLT = 300.
  DF_SPHAB = .9
  DF_DEF = -500.
  DF_RMSB = 70.
  DF_RMSA = 1.
  DF_A = 90.
  DF_QMIN = 0.
  DF_QMAX = .95
  DF_DQ = .01
  DF_VIEW = 1.
C
C
97  CALL VCALL('the first spatial frequency ', DF_U, U)
  WRITE(6,102)
102 FORMAT(' Input the bounds of the second spatial frequency ')
  CALL VCALL('the lower spatial frequency ', DF_QMIN, QMIN)
  CALL VCALL('the upper spatial frequency ', DF_QMAX, QMAX)
  CALL VCALL('the frequency sampling step ', DF_DQ, DQ)
  CALL VCALL('angle subtended in degrees ', DF_A, A)
  A = A*PI/180.
  CALL VCALL('accelerating voltage in kV ', DF_VOLT, VOLT)
  LAM = 12.26/(SQRT(VOLT*1E3)*SQRT(1+.9788E-3*VOLT))
  CALL VCALL('spherical aberration in mm ', DF_SPHAB, SPHAB)
  SPHAB = SPHAB*1E7
  CALL VCALL('lense defocus in angstroms ', DF_DEF, DEF)
  CALL VCALL('focal spread in angstroms ', DF_RMSB, RMSB)
  CALL VCALL('beam convergence in mRad ', DF_RMSA, RMSA)
C
  WRITE(6,995)
995 FORMAT(' The output can be supplied in terms of /,
# ' amplitude contrast (input as -1)' /,
# ' phase contrast (input as 0)' /,
# ' envelope term only (input as 1)' /,
# ' the default case is phase contrast')
C
  CALL VCALL('your choice of output -1,0,1 ', DF_VIEW, VIEW)
C
  BETA = (1./RMSB)**2
  ALPHA = (LAM/(RMSA*1E-3))**2
  Q = QMIN
C
C ONCE U AND A HAVE BEEN GIVEN
C THE OTHER SPATIAL PARAMETERS CAN BE CALCULATED
C
11  E = Q/U - COS(A)
  IF (E .NE. 0.) GOTO 12

```

```

      C = ATAN(SIN(A)/1E-6)
      GOTO 13
12    C = ATAN(SIN(A)/ABS(E))
13    B = PI - A - C
      V = SIN(A)*U/SIN(C)
C
      CALL CONVEN(U,Q,V,A,B,C,ALPHA,BETA,DEF,LAM,SPHAB,PI,F1)
C
      WRITE(7,997) Q,CONJG(F1)
997   FORMAT(4(F10.6,X))
C
      CALL SECOND(U,V,Q,A,B,C,RMSA,ALPHA,BETA,DEF,LAM,SPHAB,PI,F2)
C
      WRITE(8,997) Q,CONJG(F2)
C
      CALL FULL(U,V,Q,A,B,C,RMSA,ALPHA,BETA,DEF,LAM,SPHAB,PI,F3)
C
      WRITE(9,997) Q,CONJG(F3)
C
      CALL MIKE(U,V,Q,A,B,C,RMSA,ALPHA,BETA,DEF,LAM,SPHAB,PI,F4)
C
      WRITE(10,997) Q,CONJG(F4)
C
      CALL ISHI(U,V,Q,A,B,C,RMSA,ALPHA,BETA,DEF,LAM,SPHAB,PI,F5)
C
      WRITE(9,997) Q,CONJG(F5)
C
      CALL CROSS(U,V,Q,A,B,C,RMSA,ALPHA,BETA,DEF,LAM,SPHAB,PI,F2)
C
      WRITE(10,997) Q,CONJG(F2)
C
      CALL NEW(U,V,Q,A,B,C,ALPHA,BETA,DEF,LAM,SPHAB,PI,F3)
C
      WRITE(11,997) Q,CONJG(F3)
C
      Q = Q + DQ
      IF (Q .LE. QMAX) GOTO 11
C
C   CONTINUING THE PROGRAM
C
      DF_U = U
      DF_VOLT = VOLT
      DF_SPHAB = SPHAB/1E7
      DF_DEF = DEF
      DF_RMSB = RMSB
      DF_RMSA = RMSA
      DF_A = A*180./PI
      DF_QMIN = QMIN
      DF_QMAX = QMAX
      DF_DQ = DQ
C   DF_VIEW = VIEW

```

```

C
  WRITE(6,998)
998  FORMAT(' DO YOU WANT TO REPEAT (Y OR N) ? '$)
  READ(5,999) ANSWER
999  FORMAT(A1)
  IF(ANSWER .EQ. 'Y' .OR. ANSWER .EQ. 'y') GOTO 97
C
C  WRITING TO THE FILE IS DONE
C
  STOP
  END
C
  subroutine vcall(string,default,value)
  character*29 string
  temp=0
  value=default
  WRITE(6,100)string,default
100  FORMAT(' Input 'a29,' (Default=',f10.4,' )_ '$)
  read(5,200,err=300)temp
200  format(f10.0)
300  IF(TEMP.ne.0.)value=TEMP
  return
  end
C
C
C
C
  SUBROUTINE CONVEN(U,Q,V,A,B,C,ALPHA,BETA,DEF,LAM,SPHAB,PI,F1)
  REAL U,Q,V,A,B,C,ALPHA,BETA,DEF,LAM,SPHAB,PI,T1,T2,T3,T4,T5,T6,T7
  COMPLEX F1
C
  T1 = PI*LAM*U*U*(DEF + .5*SPHAB*(LAM*U)**2)
  T2 = PI*LAM*Q*Q*(DEF + .5*SPHAB*(LAM*Q)**2)
  T3 = 2*LAM*PI*U*(DEF + SPHAB*(LAM*U)**2)
  T4 = 2*LAM*PI*Q*(DEF + SPHAB*(LAM*Q)**2)
  T5 = (T3*COS(B) + T4*COS(C))**2
  T6 = ((PI*LAM)**2 * (Q**4 - 2.*(U*Q)**2 + U**4))/(-4.*BETA)
  T7 = (T3*SIN(B) - T4*SIN(C))**2
  F1 = EXP(T6)*EXP(-.25*(T5+T7)/ALPHA)*CMPLX(COS(T2-T1),SIN(T2-T1))
C
  RETURN
  END
C
C
  SUBROUTINE
  SECOND(U,V,Q,A,B,C,RMSA,ALPHA,BETA,DEF,LAM,SPHAB,PI,F2)
  REAL
  LAM,DEF,SPHAB,PI,RMSA,ALPHA,BETA,W2,DW,A,B,C,U,V,Q,GRADCHI(2)
  COMPLEX Y3,X1,X2,X3,X4,X5,X6,F2
C
C  NOW COMPUTING THE VALUE OF THE FUNCTION

```

```

C
Y1 = PI*LAM*U*U * (DEF + 0.5*SPHAB*((LAM*U)**2))
Y2 = PI*LAM*Q*Q * (DEF + 0.5*SPHAB*((LAM*Q)**2))
GRADCHI(1) = PI*2.*LAM*U * (DEF + SPHAB*((LAM*U)**2))
GRADCHI(2) = PI*2.*LAM*Q * (DEF + SPHAB*((LAM*Q)**2))
C
T1 = ((PI*LAM)**2) * (Q**4 - 2.*((U*Q)**2) + U**4)/(-4.*BETA)
Y3 = EXP(T1) * CMPLX(COS(Y2-Y1),SIN(Y2-Y1))
C
C   FOR W PERPENDICULAR TO U-Q (ANALYTICALLY)
C
T2 = (GRADCHI(1)*SIN(B) - GRADCHI(2)*SIN(C))**2
T3 = PI*SPHAB*LAM**3*(U*U*(1. + 2.*((SIN(B))**2))
#      - Q*Q*(1. + 2.*((SIN(C))**2)))
X1 = T2
X2 = CMPLX(ALPHA,T3)
X3 = 1. / CSQRT(X2)
C
C   FOR W PARALLEL (ANALYTICALLY) TO U-Q
C
T4 = (GRADCHI(1)*COS(B) + GRADCHI(2)*COS(C))**2
T5 = (PI*SPHAB*LAM**3)*(U*U*(1. + 2.*((COS(B))**2))
#      - Q*Q*(1. + 2.*((COS(C))**2)))
X4 = T4
X5 = CMPLX(ALPHA,T5)
X6 = 1. / CSQRT(X5)
C
F2 = Y3*ALPHA*CEXP(-.25*X1/X2)*CEXP(-.25*X4/X5)*X3*X6
C
C   F2 IS THE TERM WE HAVE BEEN LOOKING FOR ALL ALONG
C
RETURN
END
C
C
SUBROUTINE
FULL(U,V,Q,A,B,C,RMSA,ALPHA,BETA,DEF,LAM,SPHAB,PI,FUNC)
REAL
LAM,DEF,SPHAB,PI,RMSA,ALPHA,BETA,W2,DW,A,B,C,U,V,Q,GRADCHI(2)
COMPLEX Y3,X1,X2,X3,X4,X5,x6,FUNC
C
C   NOW COMPUTING THE VALUE OF THE FUNCTION
C
Y1 = PI*LAM*U*U * (DEF + 0.5*SPHAB*(LAM*U)**2)
Y2 = PI*LAM*Q*Q * (DEF + 0.5*SPHAB*(LAM*Q)**2)
GRADCHI(1) = PI*2*LAM*U * (DEF + SPHAB*(LAM*U)**2)
GRADCHI(2) = PI*2*LAM*Q * (DEF + SPHAB*(LAM*Q)**2)
C
T1 = (PI*LAM)**2 * (Q**4 - 2.*(U*Q)**2 + U**4)/(-4.*BETA)
Y3 = EXP(T1) * CMPLX(COS(Y2-Y1),SIN(Y2-Y1))
C

```

```

C   FOR W PERPENDICULAR TO U-Q (ANALYTICALLY)
C
  T2 = (GRADCHI(1)*SIN(B) - GRADCHI(2)*SIN(C))**2
  T3 = PI*SPHAB*LAM**3*(U*U*(1. + 2.*(SIN(B))**2)
#     - Q*Q*(1. + 2.*(SIN(C))**2))
  X1 = T2
  X2 = CMPLX(ALPHA,T3)
  X3 = 1. / CSQRT(X2)
C
C   FOR W(W2) PARALLEL TO U-Q (NUMERICALLY BY TRAPAZOIDAL RULE)
C
  W2 = -6.*RMSA/LAM
  DW = .05*RMSA/LAM
  X4 = CMPLX(0.,0.)
  T5 = GRADCHI(1)*COS(B) + GRADCHI(2)*COS(C)
  DO 40 N = 1,240
    T4 = PI*SPHAB*LAM**3*(U*U*(1. + 2.*COS(B)*COS(B))
#     - Q*Q*(1. + 2.*COS(C)*COS(C)) - 2.*W2*V)
C
C   this is the cross-term between the focal spread and convergence
C   that mike o'keefe said was important
C
  T6 = PI*PI*LAM*LAM*W2*V*(U*U-Q*Q-W2*V)/BETA
C
  X5 = CEXP(CMPLX((T6-W2*W2*ALPHA),(W2*T5 - W2*W2*T4)))
  X4 = X4 + X5*DW
  W2 = W2 + DW
40 CONTINUE
C
  FUNC = Y3*X3*CEXP(-0.25*X1/X2)*X4*ALPHA/SQRT(PI)
C
C   FUNC IS THE TERM WE HAVE BEEN LOOKING FOR ALL ALONG
C
  RETURN
  END

  SUBROUTINE MIKE(U,V,Q,A,B,C,RMSA,ALPHA,BETA,
#DEF,LAM,SPHAB,PI,FUNC2)
  REAL
LAM,DEF,SPHAB,PI,RMSA,ALPHA,BETA,W2,DW,A,B,C,U,V,Q,GRADCHI(2)
  COMPLEX Y3,X1,X2,X3,X4,X5,x6,FUNC2
C
C   NOW COMPUTING THE VALUE OF THE FUNCTION
C
  Y1 = PI*LAM*U*U * (DEF + 0.5*SPHAB*(LAM*U)**2)
  Y2 = PI*LAM*Q*Q * (DEF + 0.5*SPHAB*(LAM*Q)**2)
  GRADCHI(1) = PI*2*LAM*U * (DEF + SPHAB*(LAM*U)**2)
  GRADCHI(2) = PI*2*LAM*Q * (DEF + SPHAB*(LAM*Q)**2)
C
  T1 = (PI*LAM)**2 * (Q**4 - 2.*(U*Q)**2 + U**4)/(-4.*BETA)
  Y3 = EXP(T1) * CMPLX(COS(Y2-Y1),SIN(Y2-Y1))

```

```

C
C FOR W PERPENDICULAR TO U-Q (ANALYTICALLY)
C
T2 = (GRADCHI(1)*SIN(B) - GRADCHI(2)*SIN(C))**2
T3 = PI*SPHAB*LAM**3*(U*U*(1. + 2.*(SIN(B))**2)
#      - Q*Q*(1. + 2.*(SIN(C))**2))
X1 = T2
X2 = CMPLX(ALPHA,T3)
X3 = 1. / CSQRT(X2)
C
C FOR W(W2) PARALLEL TO U-Q (NUMERICALLY BY TRAPAZOIDAL RULE)
C including the cross-terms between spatial and temporal coherence
C
W2 = -6.*RMSA/LAM
DW = .05*RMSA/LAM
X4 = CMPLX(0.,0.)
T5 = GRADCHI(1)*COS(B) + GRADCHI(2)*COS(C)
DO 40 N = 1,240
T4 = PI*SPHAB*LAM**3*(U*U*(1. + 2.*(COS(B))**2)
#      - Q*Q*(1. + 2.*(COS(C))**2))
C
C this is the cross-term between the focal spread and convergence
C that mike o'keefe said was important
C
T6 = PI*PI*LAM*LAM*W2*V*(U*U-Q*Q-W2*V)/BETA
C
X5 = CEXP(CMPLX((T6-W2*W2*ALPHA),(W2*T5 - W2*W2*T4)))
X4 = X4 + X5*DW
W2 = W2 + DW
40 CONTINUE
C
FUNC2 = Y3*X3*CEXP(-0.25*X1/X2)*X4*ALPHA/SQRT(PI)
C
C FUNC2 IS THE TERM WE HAVE BEEN LOOKING FOR ALL ALONG
C
RETURN
END
C
SUBROUTINE
ISHI(U,V,Q,A,B,C,RMSA,ALPHA,BETA,DEF,LAM,SPHAB,PI,FUNC)
REAL
LAM,DEF,SPHAB,PI,RMSA,ALPHA,BETA,W2,DW,A,B,C,U,V,Q,GRADCHI(2)
REAL AA,BB,CC,Y1,Y2,T1,T2,T3,T4,T5,TEST
COMPLEX Y3,X1,X2,X3,X4,X5,X6,X7,X8,X9,X10,X11,X12,FUNC
C
C NOW COMPUTING THE VALUE OF THE FUNCTION
C
Y1 = PI*LAM*U*U * (DEF + 0.5*SPHAB*((LAM*U)**2))
Y2 = PI*LAM*Q*Q * (DEF + 0.5*SPHAB*((LAM*Q)**2))
GRADCHI(1) = PI*2.*LAM*U * (DEF + SPHAB*((LAM*U)**2))
GRADCHI(2) = PI*2.*LAM*Q * (DEF + SPHAB*((LAM*Q)**2))

```

```

C
T1 = ((PI*LAM)**2) * (Q**4 - 2.*((U*Q)**2) + U**4)/(-4.*BETA)
Y3 = EXP(T1) * CMPLX(COS(Y2-Y1),SIN(Y2-Y1))
C
C   FOR W PERPENDICULAR TO U-Q (ANALYTICALLY)
C
T2 = GRADCHI(1)*SIN(B) - GRADCHI(2)*SIN(C)
T3 = PI*SPHAB*LAM**3*(U*U*(1. + 2.*SIN(B)*SIN(B))
#      - Q*Q*(1. + 2.*SIN(C)*SIN(C)))
X1 = T2*T2
X2 = CMPLX(ALPHA,T3)
X3 = 1. / CSQRT(X2)
C
C   FOR W PARALLEL (ANALYTICALLY) TO U-Q
C
T4 = GRADCHI(1)*COS(B) + GRADCHI(2)*COS(C)
T5 = PI*SPHAB*LAM**3*(U*U*(1. + 2.*COS(B)*COS(B))
#      - Q*Q*(1. + 2.*COS(C)*COS(C)))
X4 = T4*T4
X5 = CMPLX(ALPHA,T5)
X6 = 1. / CSQRT(X5)
C
C   THIS PART NOW HAS THE CROSS-TERMS THAT ISHIZUKA
C   TOLD US OF... WE SHALL SEE IF THEY ARE SIGNIFICANT
C
TEST = U*U*COS(B)*SIN(B) + Q*Q*COS(C)*SIN(C)
CC = -4.*PI*SPHAB*LAM*LAM*LAM*TEST
C   X7 = CMPLX(CC,2.*ALPHA)
C
X8 = 4.*X2*X5 + CC*CC
X9 = CSQRT(X8)
X10 = (X4*X5 + X1*X2)/X8
X11 = CMPLX(0,1.)*CC*T2*T4
X12 = CEXP(X11/X8)
C
C   WRITE(6,101) X8-4.*X2*X5
101 FORMAT(' THE DIFFERENCE IS ',F10.3,2x,F10.3)
C
FUNC = Y3*(2.*ALPHA/X9)*CEXP(-X10)*X12
C
C   F2 = Y3*ALPHA*CEXP(-.25*X1/X2)*CEXP(-.25*X4/X5)*X3*X6
C
C   F2 IS THE TERM WE HAVE BEEN LOOKING FOR ALL ALONG
C
RETURN
END
C
SUBROUTINE
CROSS(U,V,Q,A,B,C,RMSA,ALPHA,BETA,DEF,LAM,SPHAB,PI,F2)
REAL
LAM,DEF,SPHAB,PI,RMSA,ALPHA,BETA,W2,DW,A,B,C,U,V,Q,GRADCHI(2)

```

```

REAL AA,BB,CC,Y1,Y2,T1,T2,T3,T4,T5,TEST,AAA,BBB,CCC,DDD
COMPLEX Y3,X1,X2,X3,X4,X5,X6,X7,X8,X9,X10,X11,X12,F2
C
C NOW COMPUTING THE VALUE OF THE FUNCTION
C
Y1 = PI*LAM*U*U * (DEF + 0.5*SPHAB*((LAM*U)**2))
Y2 = PI*LAM*Q*Q * (DEF + 0.5*SPHAB*((LAM*Q)**2))
GRADCHI(1) = PI*2.*LAM*U * (DEF + SPHAB*((LAM*U)**2))
GRADCHI(2) = PI*2.*LAM*Q * (DEF + SPHAB*((LAM*Q)**2))
C
T1 = ((PI*LAM)**2) * (Q**4 - 2.*((U*Q)**2) + U**4)/(-4.*BETA)
Y3 = EXP(T1) * CMPLX(COS(Y2-Y1),SIN(Y2-Y1))
C
AAA= U*COS(B) + Q*COS(C)
BBB= U*SIN(B) - Q*SIN(C)
CCC= (U*U - Q*Q)*AAA
DDD= (U*U - Q*Q)*BBB
C
C FOR W PERPENDICULAR TO U-Q (ANALYTICALLY)
C
T2 = GRADCHI(1)*SIN(B) - GRADCHI(2)*SIN(C)
T3 = PI*SPHAB*LAM**3*(U*U*(1. + 2.*SIN(B)*SIN(B))
#      - Q*Q*(1. + 2.*SIN(C)*SIN(C)))
C   X1 = T2*T2
X1 = CMPLX(T2,-PI*PI*LAM*LAM*DDD/BETA)
X2 = CMPLX(ALPHA - PI*PI*LAM*LAM*AAA*AAA/BETA,T3)
X3 = 1. / CSQRT(X2)
C
C FOR W PARALLEL (ANALYTICALLY) TO U-Q
C
T4 = GRADCHI(1)*COS(B) + GRADCHI(2)*COS(C)
T5 = PI*SPHAB*LAM**3*(U*U*(1. + 2.*COS(B)*COS(B))
#      - Q*Q*(1. + 2.*COS(C)*COS(C)))
C   X4 = T4*T4
X4 = CMPLX(T4,-PI*PI*LAM*LAM*CCC/BETA)
X5 = CMPLX(ALPHA - PI*PI*LAM*LAM*BBB/BETA,T5)
X6 = 1. / CSQRT(X5)
C
C THIS PART NOW HAS THE CROSS-TERMS THAT ISHIZUKA
C TOLD US OF... WE SHALL SEE IF THEY ARE SIGNIFICANT
C
TEST = U*U*COS(B)*SIN(B) + Q*Q*COS(C)*SIN(C)
CC = -4.*PI*SPHAB*LAM*LAM*LAM*TEST
X7 = CMPLX(CC,-2.*AAA*BBB)
C
X8 = 4.*X2*X5 + X7*X7
X9 = CSQRT(X8)
X10= (X4*X4*X5 + X1*X1*X2)/X8
X11= CMPLX(0,1.)*X7*X1*X4
X12= CEXP(X11/X8)
C

```

```

FUNC = Y3*(2.*ALPHA/X9)*CEXP(-X10)*X12
C
C F2 IS THE TERM WE HAVE BEEN LOOKING FOR ALL ALONG
C
RETURN
END
C
SUBROUTINE NEW(U,V,Q,A,B,C,ALPHA,BETA,DEF,LAM,SPHAB,PI,F2)
REAL LAM,DEF,SPHAB,PI,ALPHA,BETA,W2,DW,A,B,C,U,V,Q,GRADCHI(2)
REAL Y1,Y2,T1,T2,T3,T4,AAA,BBB
REAL AA,BB,CC,DD,EE,GG,JJ
COMPLEX Y3,I,HH,II,DETW,X1,X2,F2
C
C THIS SUBROUTINE WILL SOLVE THE CTF BY MONICA'S METHOD
C IT DOES NOT CONSIDER THE CUBIC TERM OF W
C
C NOW COMPUTING THE VALUE OF THE FUNCTION
C
Y1 = PI*LAM*U*U * (DEF + 0.5*SPHAB*((LAM*U)**2))
Y2 = PI*LAM*Q*Q * (DEF + 0.5*SPHAB*((LAM*Q)**2))
GRADCHI(1) = PI*2.*LAM*U * (DEF + SPHAB*((LAM*U)**2))
GRADCHI(2) = PI*2.*LAM*Q * (DEF + SPHAB*((LAM*Q)**2))
C
Y3 = (ALPHA*SQRT(8.*BETA)) * CMPLX(COS(Y2-Y1),SIN(Y2-Y1))
C
T1 = GRADCHI(1)*COS(B) + GRADCHI(2)*COS(C)
T2 = GRADCHI(1)*SIN(B) - GRADCHI(2)*SIN(C)
T3 = PI*SPHAB*LAM**3*(U*U*(1. + 2.*COS(B)*COS(B))
# - Q*Q*(1. + 2.*COS(C)*COS(C)))
T4 = PI*SPHAB*LAM**3*(U*U*(1. + 2.*SIN(B)*SIN(B))
# - Q*Q*(1. + 2.*SIN(C)*SIN(C)))
C
AAA= U*COS(B) + Q*COS(C)
BBB= U*SIN(B) - Q*SIN(C)
C
AA = -T1
BB = -T2
CC = PI*LAM*(U*U - Q*Q)
DD = 2.*PI*SPHAB*LAM*LAM*LAM*
# (U*U*COS(B)*SIN(B) - Q*Q*COS(C)*SIN(C))
EE = -2.*PI*LAM*AAA
GG = -2.*PI*LAM*BBB
HH = CMPLX(ALPHA,T3)
II = CMPLX(ALPHA,T4)
JJ = BETA
C
I = CMPLX(0,1.)
C
DETW = 2.*(EE*EE*II + GG*GG*HH + DD*DD*JJ)
# + 8.*HH*II*JJ - 2.*I*DD*EE*GG
C

```

```
      X1 = AA*AA*(GG*GG + 4.*I*JJ) + BB*BB*(EE*EE + 4.*HH*JJ)
#     + CC*CC*(DD*DD + 4.*HH*II)
C
      X2 = AA*BB*(EE*GG + 2.*I*DD*JJ) + AA*CC*(DD*GG + 2.*I*EE*II)
#     + BB*CC*(DD*EE + 2.*I*HH*GG)
C
      X3 = 1./CSQRT(DETW)
C
      F2 = Y3*X3*CEXP((-0.5*X1 + X2)/DETW)
C
      F2 IS THE TERM WE HAVE BEEN LOOKING FOR ALL ALONG
C
      RETURN
      END
```

Appendix Five. UHV Microscope and Furnace Designs

The following drawings were used to design and build the UHV microscope and furnace systems. Each drawing is in its own scale and was drawn according in the design scheme requested from the Materials Science Machine Shop.

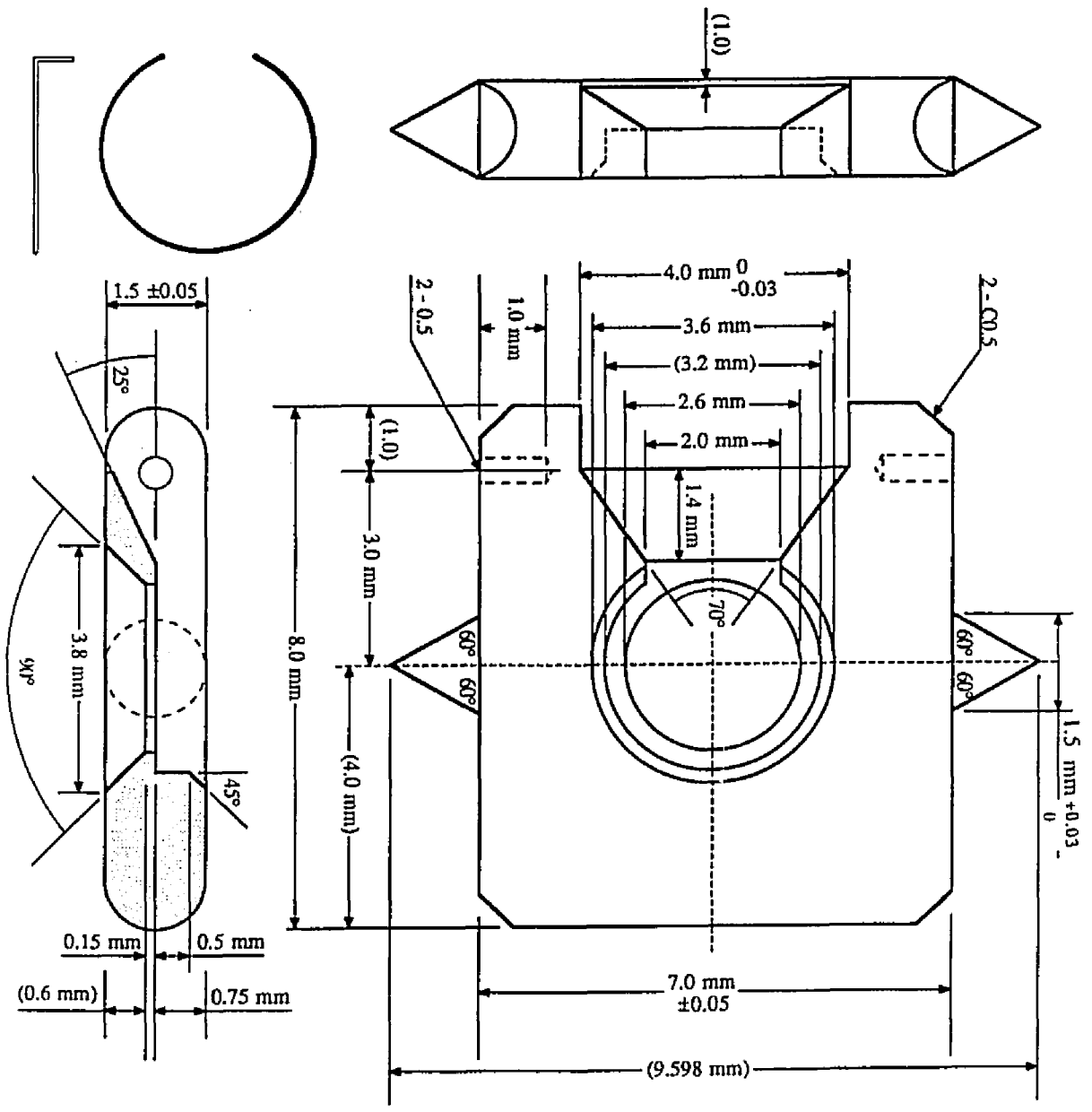
The 3 mm cartridge design is shown on page 165. This design was used instead of Hitachi's 2.3 mm holder which had only a 1 mm cross-section available for specimen collection.

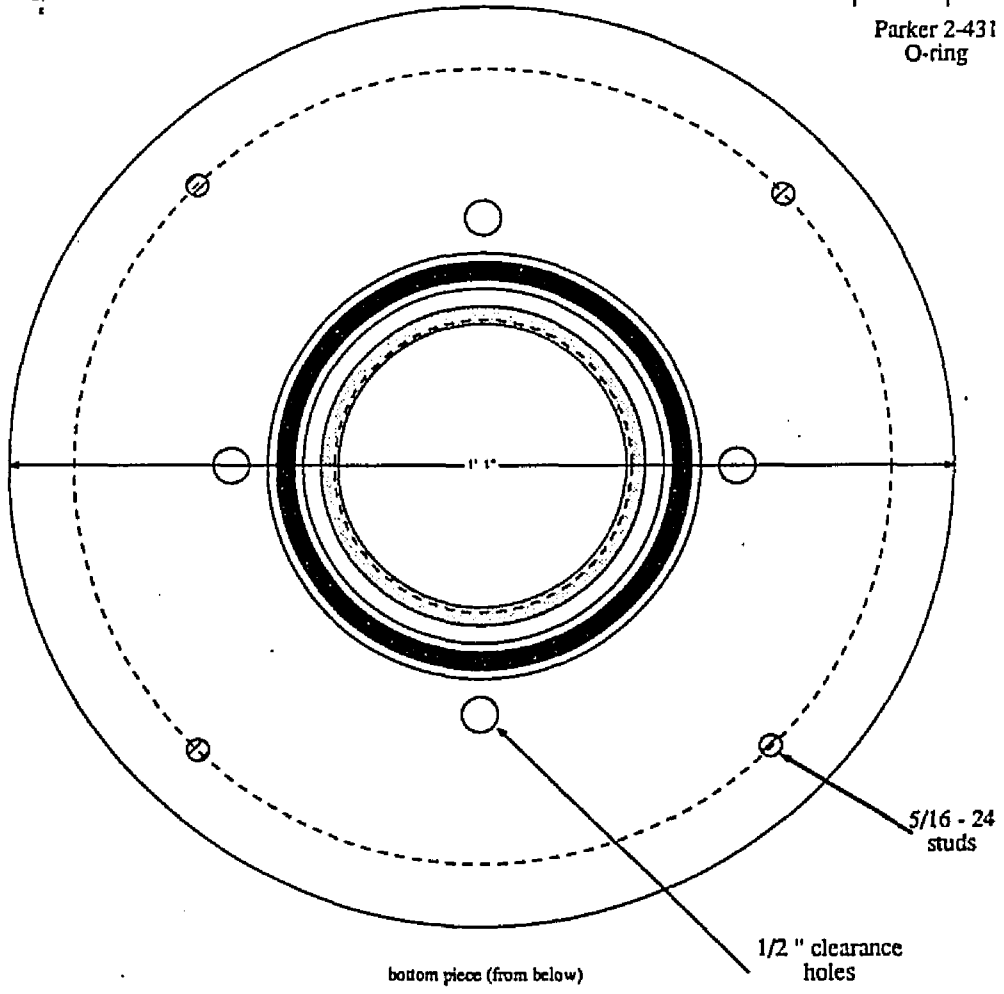
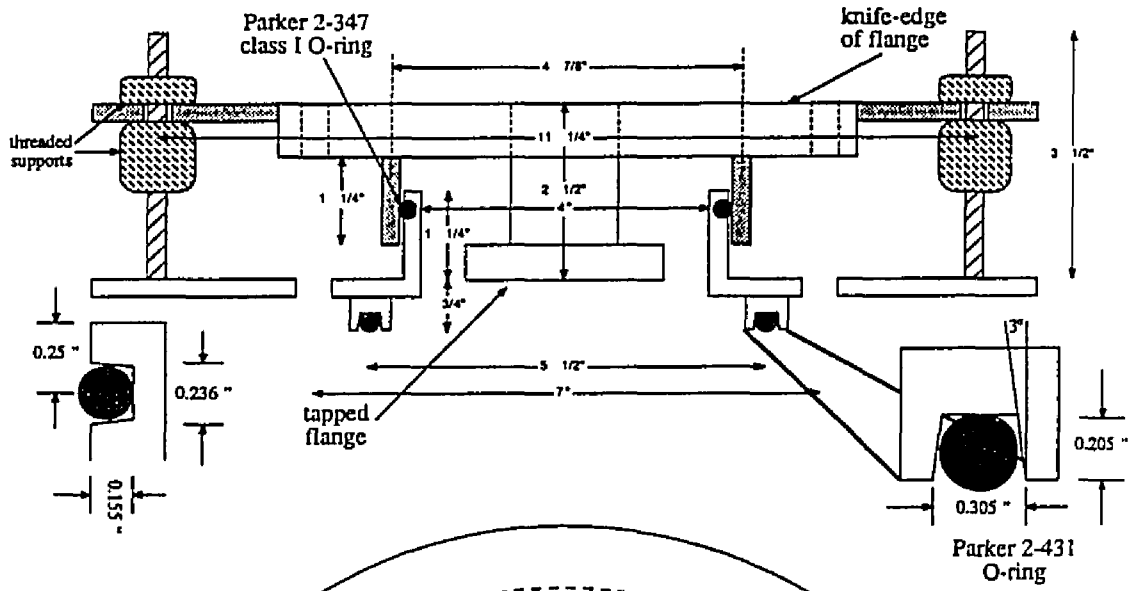
Pages 166 and 167 are the sliding O-ring seal design for the collection chamber. This fitting was designed to link the UHV collection chamber with the O-ring sealed furnace vacuum chamber. The sliding seal has three degrees of freedom; vertical adjustments are provided by the threaded posts and the xy planar adjustments by the large O-ring.

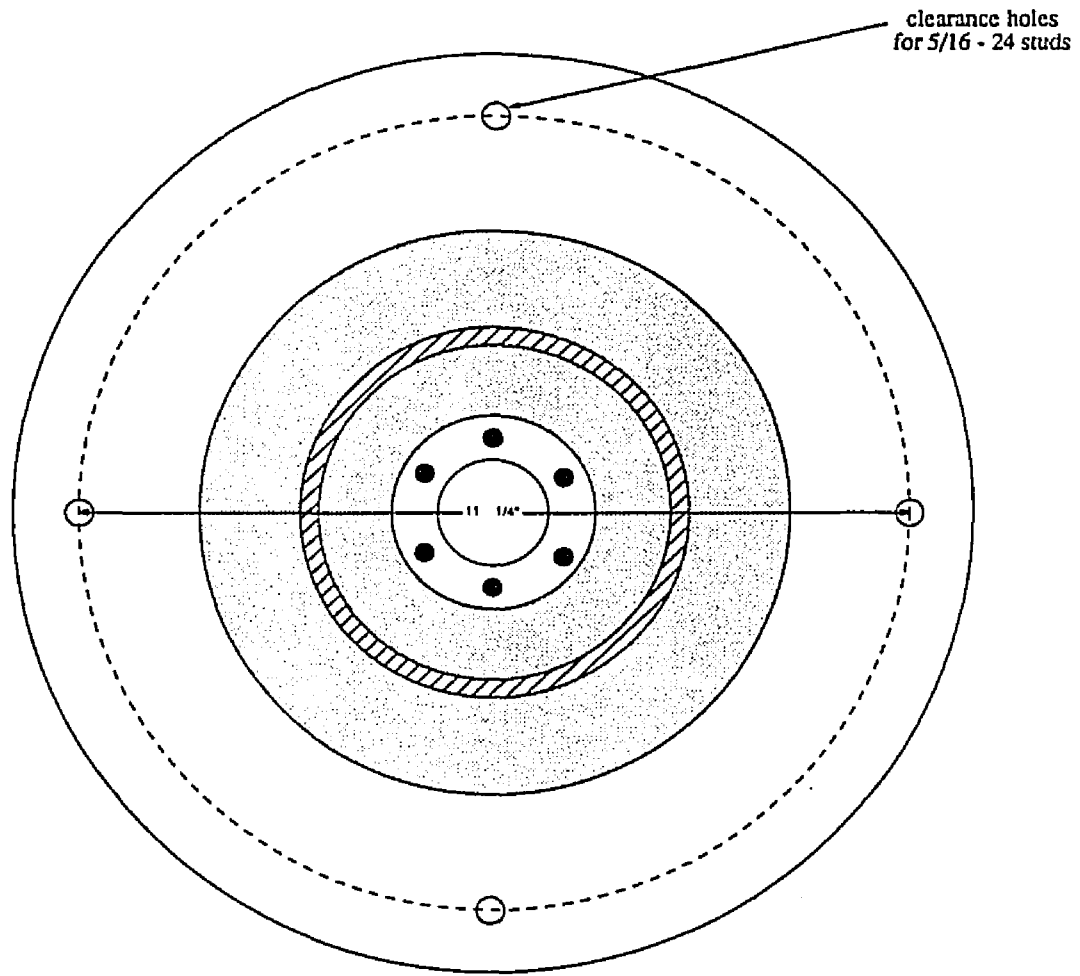
Page 168 is the specimen collection chamber which has many ports for the attachment of vacuum gauges, transfer system, etc.

Page 169 is the design for the electrode chamber which must also connect the furnace tube to a UHV seal while the chamber itself has an O-ring seal for connection to the large furnace vacuum chamber. The chamber has a large viewport flange, eight inch electrode flange connection and a flange for the Ar/O₂ leak valve.

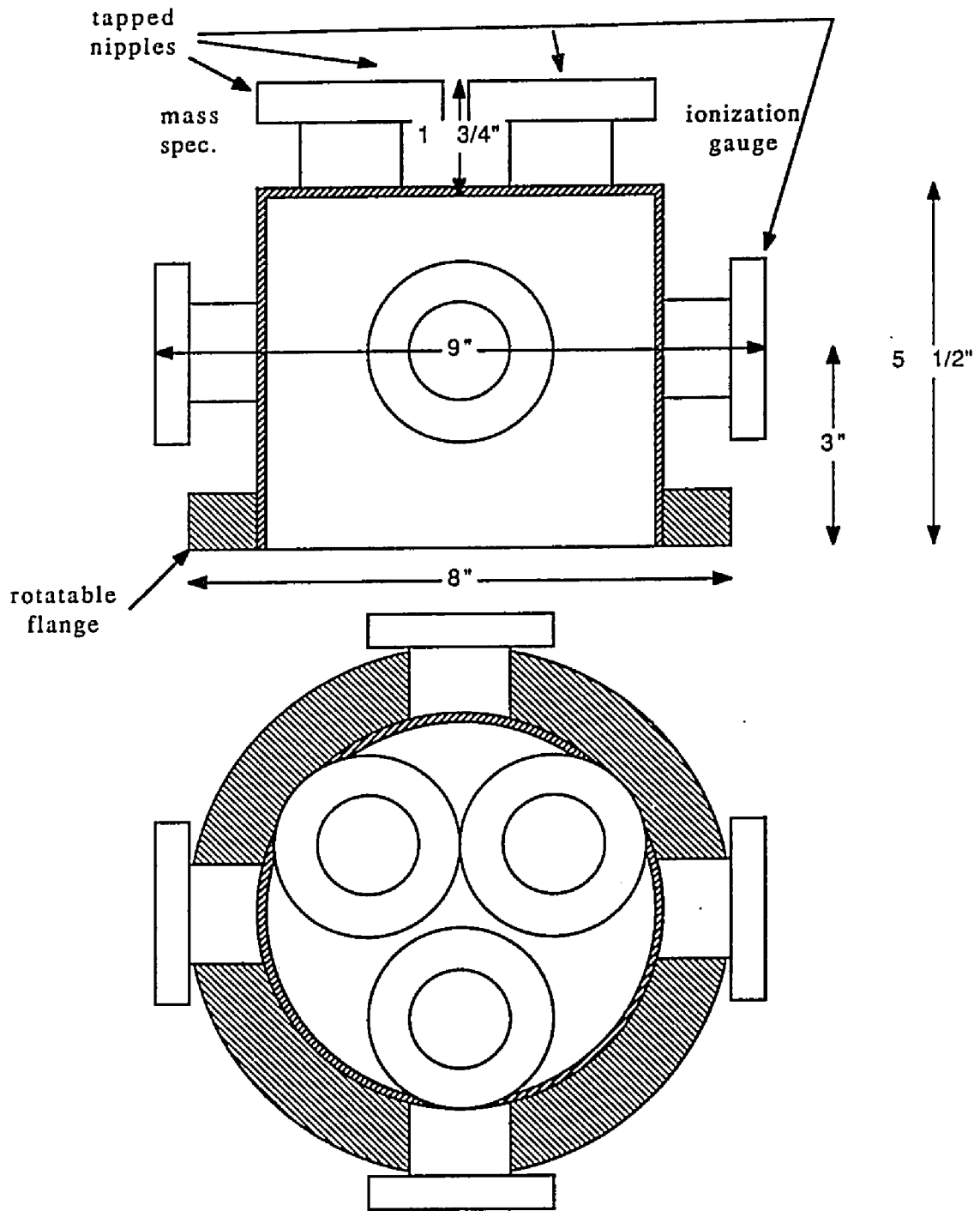
Pages 170 and 171 are the designs of the specimen cartridge 'grabber' jaws. These jaws are designed to fit around the cartridge, thereby aligning the tilting pins and holding them still. The grabber scheme was used for the primary reason that the STC is not of sufficient size to allow for a single piece.

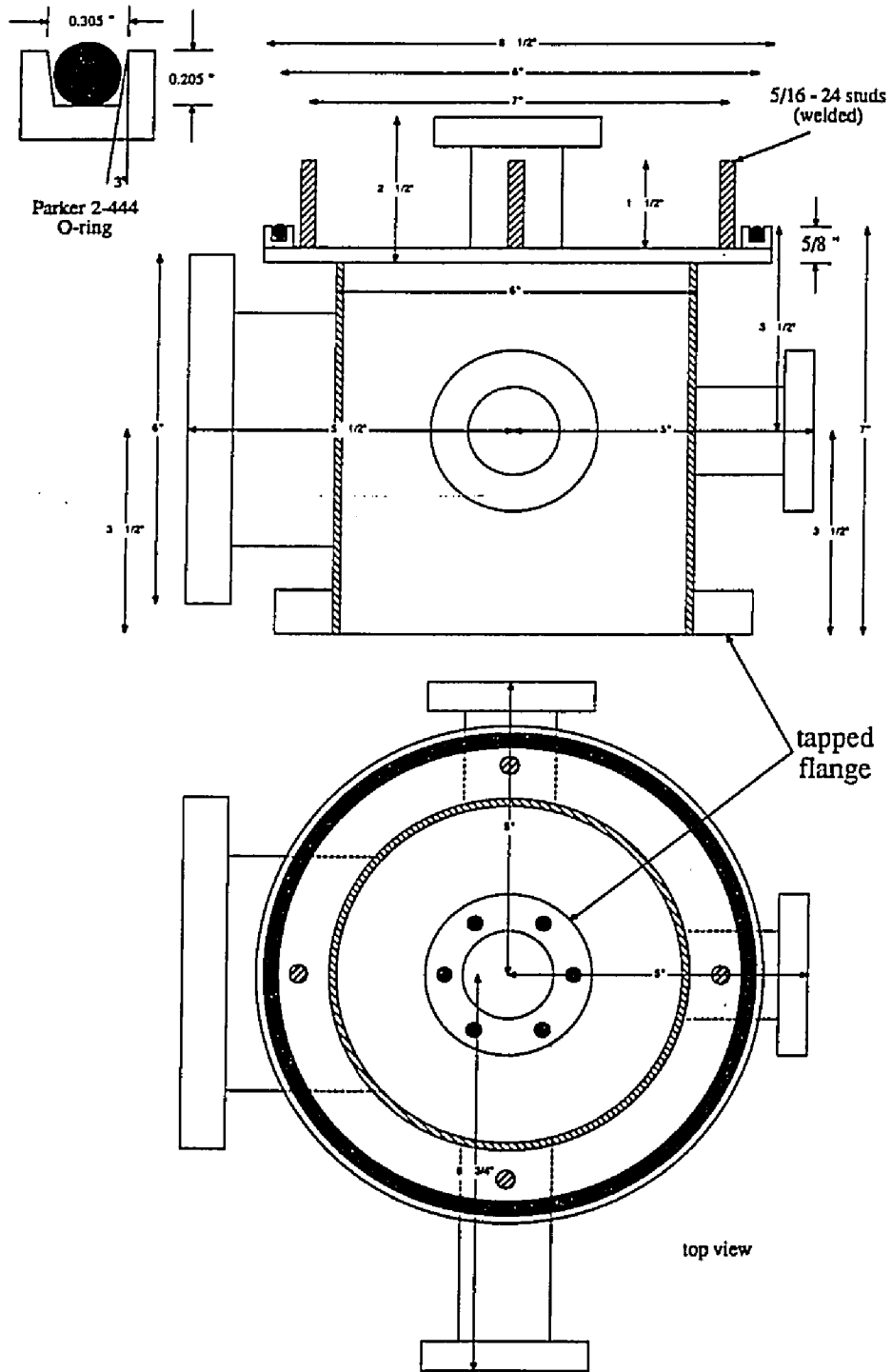


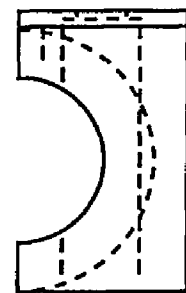
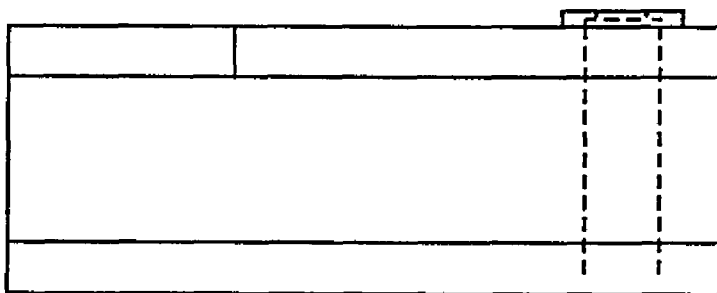
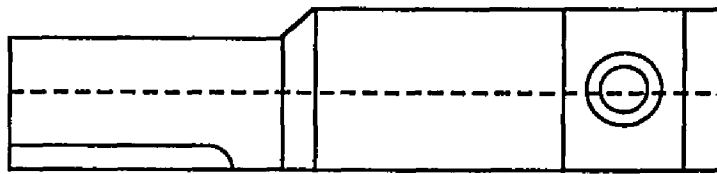
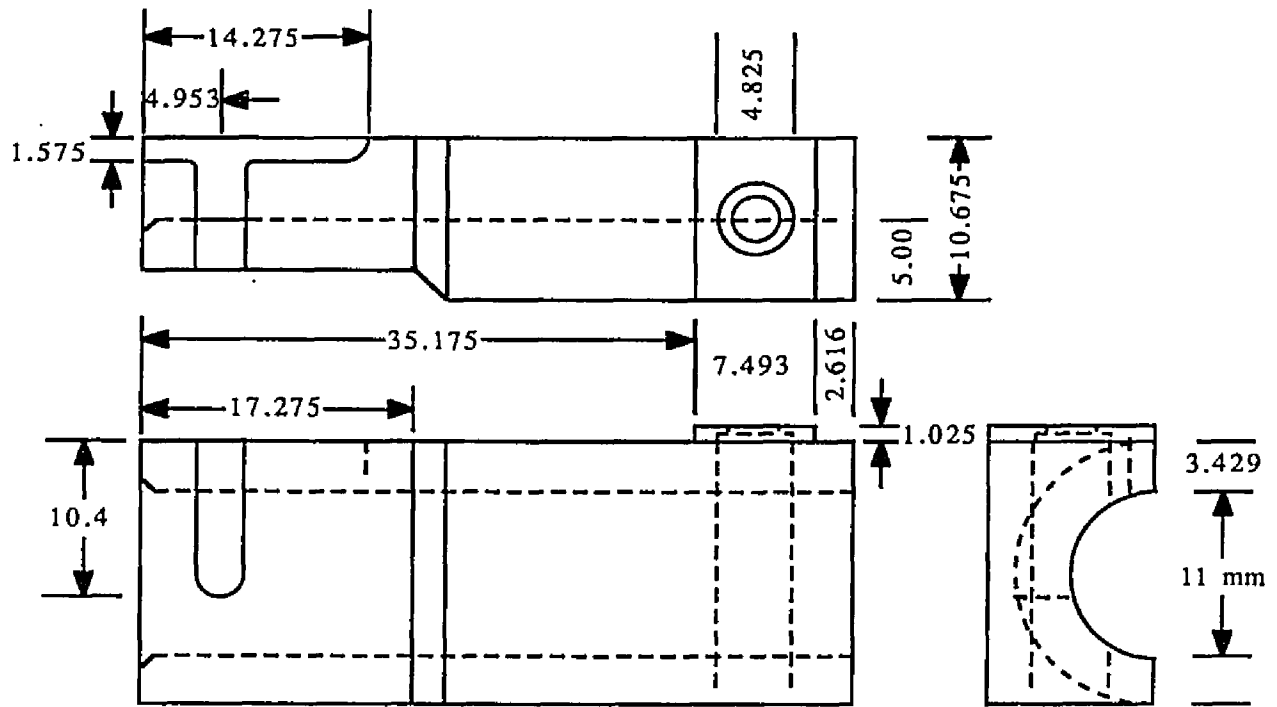


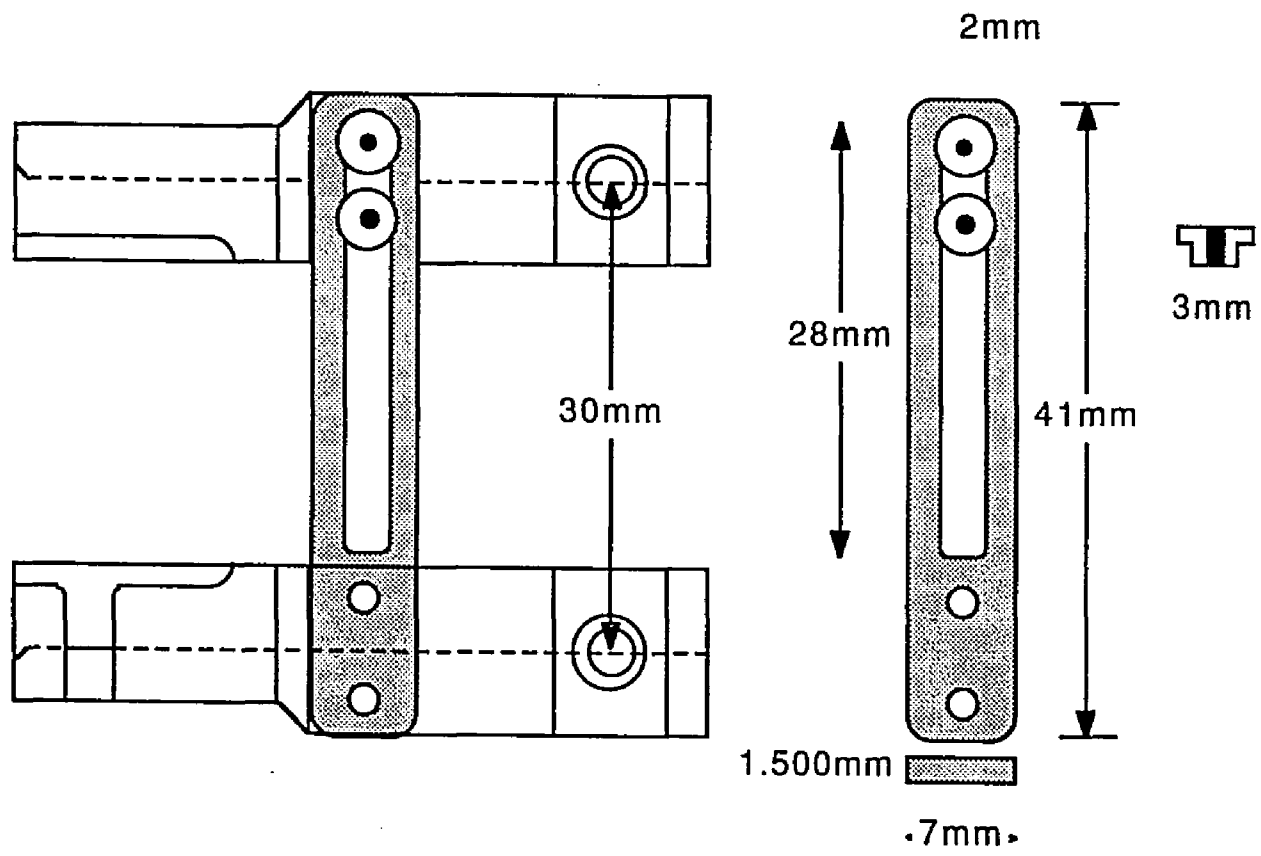


top piece (from below)









Appendix Six. UHV Design Philosophy

The preceding appendix has shown the UHV designs which were used to modify the UHV microscope and the designs used to build the UHV furnace. In addition to the design scheme, i.e. the main idea which is the essence of a successful piece of equipment, there are some general rules governing the making of any UHV component. This appendix outlines the considerations that went into all designs and is intended as a first-principles approach to UHV design.

To design successfully for the UHV environment one must;

- First read and understand O'Hanlon's Users Guide to Vacuum Technology (Wiley 1989). This book describes many useful vacuum concepts (such as conductances) and pumping systems (ion, turbo, sublimation, diffusion, etc.).
- Then enroll in a surface science course (C80 at present). This will help familiarize oneself with surface science concepts (that is, what can and cannot be done in surface science) and experimental design and instrumentation.

Designing for UHV

Now one is ready to begin the UHV design process. The first thing to remember is that if one is working on the UHV-HREM, then several, and sometimes conflicting, concepts must be considered.

- Surface scientists like to work with large samples ($\approx 1 \text{ cm}^2$ of surface area) whereas microscopy requires very small samples which are also necessarily thin ($< 50 \text{ nm}$). These two requirements must always be balanced.
- Any component for the UHV must be made of materials which are compatible with both surface science and microscopy. That means;
→ Low outgassing materials such as stainless steel or aluminum, and not brass, are

good for chamber walls. However, stainless steels have residual magnetism which makes them unacceptable for use in the microscope specimen region...use copper-beryllium alloys instead. Use aluminum for low-weight applications.

- Since the microscope is involved, one must ensure that inherent vibrations are quite small as this conflicts with the needs of high resolution microscopy. Vibrations result from components which have a lot of 'slop' in the design causing them to fit together loosely or from components that degrade during use in the microscope (i.e. springs which stress relax over time at elevated temperatures).
- The component must be able to withstand a high temperature bakeout (e.g. 200°C) without failure. This precludes the use of some materials in load-bearing applications where they may begin to creep under stress. In addition, one must consider that under the conditions of vacuum and high temperature that materials can vacuum-weld together. This is important for sliding components, etc. where the use of a molybdenum coating (low coefficient of friction) on the component can alleviate this problem.
- Any design must avoid the presence of virtual leaks and also provide for adequate pumping conductance. Bolts or screws should have center holes or flats on the threads and designs with open spaces for pumping are desired.

UHV Component Cleaning

Once a UHV component has been designed, refined, and finally built one will receive from the machine shop a piece of equipment which is completely greasy, filthy, and otherwise totally UHV incompatible!! The part must be cleaned thoroughly for UHV:

- First remove all the grime from the component by washing it in a mixture of distilled water and Alconox (glassware cleanser). Careful not to drop the part as this solution is quite slippery. Also, the UHV knife-edges are especially good

- traps of crud, one can use the edge of a thumbnail to clean them.
- Thoroughly dry the component with a lint-free towel (Kim-wipes). Don't let it 'drip-dry' as this will leave residues.
 - Reclean the component with acetone and a lint-free towel to remove any residual oils. Remember to wear gloves (NO talcum powder).
 - To get rid of any residues from the acetone (e.g. benzene), clean with research grade methanol (anhydrous). Gloves here are an absolute must!
 - Now, heat the component in air to remove any water vapor and crack any residual hydrocarbons on the surfaces. The baking time will vary with the heat capacity/conductivity of the component. For an eight-inch flange 10 minutes with the heat gun on high is usually sufficient. Careful not to handle the part with gloves (they will melt) and ensure that others in the laboratory behave likewise.

Some components come from the machine shop with burrs, etc. These must be removed by a file or sanding with emory paper. The amount of burring depends on the types of materials used, for instance aluminum spalls more than steel.

Also remember to protect the knife-edge seals at all costs!! Never use hardened steels near a knife-edge as they can fatally scratch it. The cardinal rule is: only God is allowed to use metal near a knife-edge and then only under advisement.

VITA

Name: John Edward Bonevich
Place of Birth: Kalamazoo, Michigan, USA
Date of Birth: July 20, 1964

Education: Northwestern University, Evanston, Illinois, USA
Ph.D. Materials Science and Engineering (June 1991)
University of Michigan, Ann Arbor, Michigan, USA
B.S.E. Materials and Metallurgical Engin. (May 1986)

Publications:

- J.E. Bonevich and L.D. Marks, *Ultramicroscopy* 26 (1988) 313.
- J.E. Bonevich and L.D. Marks, *Hitachi Instrument News*, 17th Edition (1989), p. 4.
- J.E. Bonevich, *Proc. 47th Ann. Meet. Electron Microsc. Soc. Amer.* (1989), p. 258.
- J.E. Bonevich, J.P. Zhang, M. Jacoby, R. Ai, D.N. Dunn, P.C. Stair and L.D. Marks, *Proc. 47th Ann. Meet. Electron Microsc. Soc. Amer.* (1989), p. 550.
- J.E. Bonevich, R. Ai, M. Jacoby, P.C. Stair and L.D. Marks, *Surface Reactions in the Space Environment, AFOSR Conference Proceedings* (1989).
- J.E. Bonevich and L.D. Marks, *Ultramicroscopy* 32 (1990) 297.
- J.E. Bonevich and L.D. Marks, *J. Electron Microscopy Technique* (invited review, 1990), in press.
- Y. Ma, J.E. Bonevich and L.D. Marks, *Proc. XIIth Internat. Cong. Electron Microsc. Vol. 2* (1990), p. 390.
- J.E. Bonevich and L.D. Marks, *Surface Reactions in the Space Environment, AFOSR Conf. Proc.* (1990).
- J.E. Bonevich and L.D. Marks, *Ultramicroscopy* 35 (1991) 161.
- J.E. Bonevich, Y. Ma and L.D. Marks, *Acta Cryst.* (1991), submitted.
- L.D. Marks, R. Ai, J.E. Bonevich, M.I. Buckett, D.N. Dunn and J.P. Zhang, *Proc. 3rd Conf. Frontiers of Electron Microscopy, Ultramicroscopy* (1991), in press.
- J.E. Bonevich, *Proc. 49th Ann. Meet. Electron Microsc. Soc. Amer.* (1991), in press.

